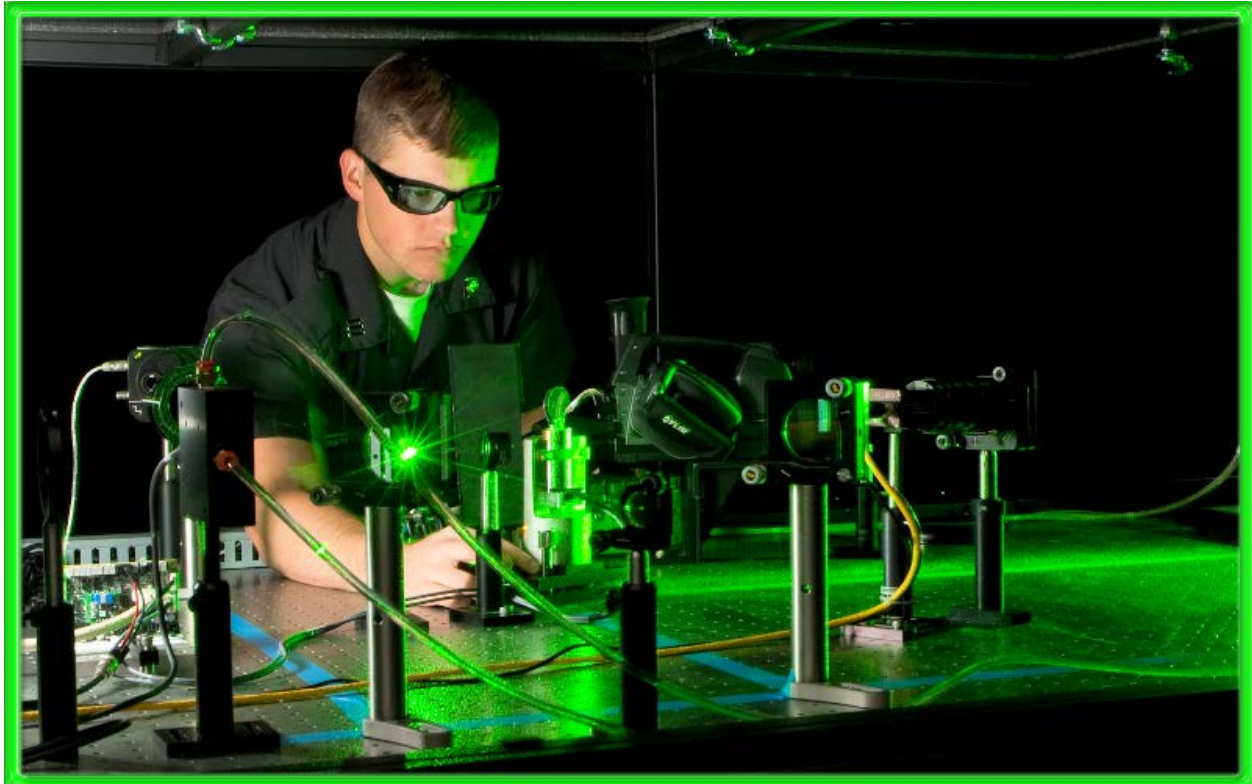# UNITED STATES MILITARY ACADEMY

25 Years of Enlightening Research

2012 Program Review

Photonics Research Center
United States Military Academy
West Point, NY 10996

Report Documentation Page

1. REPORT DATE **2012**	2. REPORT TYPE	3. DATES COVERED **00-00-2012 to 00-00-2012**

4. TITLE AND SUBTITLE **United States Military Academy: 25 Years of Enlightening Research**	5a. CONTRACT NUMBER
	5b. GRANT NUMBER
	5c. PROGRAM ELEMENT NUMBER
6. AUTHOR(S)	5d. PROJECT NUMBER
	5e. TASK NUMBER
	5f. WORK UNIT NUMBER

7. PERFORMING ORGANIZATION NAME(S) AND ADDRESS(ES) **Photonics Research Center,United States Military Academy,West Point,NY,10996**	8. PERFORMING ORGANIZATION REPORT NUMBER

9. SPONSORING/MONITORING AGENCY NAME(S) AND ADDRESS(ES)	10. SPONSOR/MONITOR'S ACRONYM(S)
	11. SPONSOR/MONITOR'S REPORT NUMBER(S)

12. DISTRIBUTION/AVAILABILITY STATEMENT
Approved for public release; distribution unlimited

13. SUPPLEMENTARY NOTES

14. ABSTRACT

15. SUBJECT TERMS

16. SECURITY CLASSIFICATION OF:			17. LIMITATION OF ABSTRACT	18. NUMBER OF PAGES	19a. NAME OF RESPONSIBLE PERSON
a. REPORT **unclassified**	b. ABSTRACT **unclassified**	c. THIS PAGE **unclassified**	**Same as Report (SAR)**	**116**	

THE PHOTONICS RESEARCH CENTER
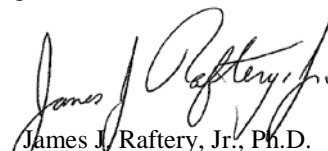*Biennial Program Review*
2009 – 2012

Director's Message

In May 2012, the Photonics Research Center (PRC) reached its 25th anniversary of providing service to the United States Army, doing so from newly renovated office and laboratory spaces in the Military Academy's Science Center, which were occupied in January 2012. Established in 1987 by a memorandum of understanding between the Superintendent of the Military Academy and the Vice Chief of Staff of the Army, the PRC has three mission essential tasks: educate future Army leaders, conduct basic and applied research, and support the Army and the Department of Defense in the areas of laser and photonics technologies. This report summarizes the research and education efforts of the PRC nominally from the last report in November 2009 to October 2012, though academic years 2011 and 2012 are its focus. This report is produced in partial fulfillment of a biennial program review conducted by the Army Research Office, the Center's principal funding agency.

The personnel situation within the PRC, like that within the Army at large, has been affected by our nation's overseas operations in Afghanistan and Iraq. Several of our research faculty, both those assigned within the PRC and those assigned within Departments, have served combat deployments. West Point's first and only Professor of Photonics, LTC John Hartke, is currently serving as the senior military advisor and team chief at the National Military Academy of Afghanistan. LTC Kraig Sheetz also deployed and served in this role while assigned within the PRC as the Academy Professor from the Department of Physics and Nuclear Engineering. While serving as Academy Professor from the Department of Chemistry and Life Science and as the PRC director, LTC Bill Pearman deployed to Afghanistan to support an RDECOM mission as a Science and Technology Assistance Team leader. This summer, while serving as the Academy Professor from the Department of Electrical Engineering and Computer Science and as the PRC director, I deployed to Baghdad, Iraq in support of the U.S. Embassy's security cooperation mission. During this time of persistent conflict, the Departments have maintained their steadfast commitment to each resource the PRC with a senior Ph.D. holding faculty member (nominally an Academy Professor), as well as a rotating faculty member. In recent years the PRC has perhaps enjoyed some of the widest participation of faculty members not assigned within the Center. A significant change to the staffing of the PRC was the 2011 reduction of the support staff from two positions to one by the loss of an authorization for the Department of Army Civilian Administrative Support Assistant.

Our researchers continued to engage cadets in our mission essential task of educating future Army officers in the area of photonics. Each year since the last review, the PRC has received annual funding from the High Energy Laser Joint Technology Office in support of the laser education mission. The number of cadets performing research in the PRC has grown each of the last past two years. A cadet capstone project team placed third in the Soldier Design Competition held at the Massachusetts Institute of Technology in 2010, and had their project picked up for prototyping by the Army's Asymmetric Warfare Group. The interdisciplinary nature of the PRC research program was demonstrated by a Chemical Engineering cadet, CDT Matt Letarte, being advised by an Electrical Engineering faculty member, CPT John Zehnpfennig, and presenting their work at the 2012 Conference on Lasers and Electro-Optics (CLEO), as well as the ongoing successes of the High Energy Laser project. The researchers in the PRC continue to provide support and expertise in laser and photonics technologies across the Army, the Department of Defense, and other government agencies.

The research accomplishments highlighted in this report represent the products of a healthy, mature research organization focused on educating our future Army leaders and closing technology gaps in the area of photonics. They are the result of hard work and are a tribute to the extremely talented researchers, cadets, and staff that are associated with the Center. They are our Light Fighters!

James J. Raftery, Jr., Ph.D.
Colonel, Academy Professor
Director

THE PHOTONICS RESEARCH CENTER

Center Overview

The Photonics Research Center has achieved its 25th year of service at the United States Military Academy. It was established at West Point in May of 1987 through a Memorandum of Understanding between the Superintendent of the United States Military Academy and the Vice Chief of Staff of the Army. An excerpt from this memorandum provides some insight into the charter of the Center:

> *"As the Army modernizes in an increasingly complex technological environment, it is essential that Army officers understand the advanced technologies which form critical elements of our evolving weapons systems. One technology field which is already exerting a major influence on force planning, and whose impact is certain to grow over the next two decades, is the physics and engineering of lasers, and the technologies associated with their development and applications. The Army needs a strong base of research and development in laser-related fields. It also needs an officer corps generally familiar with laser technologies and a subset of that officer corps whose members are experts in developing and applying those technologies."*

The PRC is formally staffed by faculty from the Departments of Chemistry & Life Science, Electrical Engineering & Computer Science, and Physics & Nuclear Engineering. Additionally, other faculty from both inside and outside these three departments participate in the PRC conducting research in laser and photonics technology areas. The PRC's three mission essential tasks are to *educate* both cadets and officers, conduct basic and applied *research*, and provide *support* to the Army in the area of laser and photonics technologies. Sustaining funding support for the PRC is provided through the Physics Division of the Army Research Office.

Each year, educational programs associated with the PRC introduce over 1000 cadets to photonics technologies, provide select cadets with an in-depth understanding of laser and photonics technologies, and return officers to the Army who are now considered experts in these technologies. In addition to sponsoring cadet projects and faculty research opportunities, the PRC maintains six to eight active research experiments producing both faculty and cadet conference presentations and technical journal articles. Specific research areas include spectroscopy, micro-cavity lasers and resonators, high energy continuous wave lasers, high power ultrashort pulsed lasers, optical information and signal processing, and hyperspectral imaging.

Additionally, the PRC has provided technical support to the Army, the Department of Defense, and other U.S. government agencies. Examples of the supported organizations are the Army's Program Executive Office Soldier (PEO Soldier), the Army's Space and Missile Defense Command (SMDC), the Joint Improvised Explosive Device Defeat organization (JIEDDO), the Office of the Secretary of Defense High Energy Laser Joint Technology Office (HEL-JTO), and the Department of Justice. PRC research faculty have deployed to combat locations in Afghanistan and Iraq. Finally, we have maintained a strong connection to the Army science and technology, as indicated by an internal PRC research position currently being filled by a visiting scientist from the Army Research Laboratory's Sensors and Electron Devices Directorate.

Photonics Research Center Assigned Staff and Faculty
2010 – 2012

Board of Directors

COL Edward P. Naessens, Jr., Ph.D. in Nuclear Engineering, Rensselaer Polytechnic Institute, 1999, Professor and Head, Department of Physics.

COL Eugene K. Ressler, Ph.D. in Computer Science, Cornell University, 1993, Professor and Head, Department of Electrical Engineering and Computer Science.

COL Leon L. Robert, Ph.D. in Entomology, Texas A&M University, 1987, Professor and Head, Department of Chemistry and Life Science.

Academy Professors

COL James J. Raftery, Jr., Ph.D. in Electrical Engineering, University of Illinois at Urbana-Champaign, 2005, Associate Professor, Department of Electrical Engineering and Computer Science.

LTC William F. Pearman, Ph.D. in Analytical Chemistry, University of South Carolina, 2007, Assistant Professor, Department of Chemistry and Life Science.

LTC Kraig Sheetz, Ph.D. in Applied Physics, Colorado School of Mines, 2009, Assistant Professor, Department of Physics and Nuclear Engineering.

Visiting Scientist

Nicholas F. Fell, Jr., Ph.D. in Analytical Chemistry, University of Illinois at Urbana-Champaign, 1993, Assistant Professor, Department of Chemistry and Life Science.

Title X Civilians

Caitlin N. Rinke-Kneapler, Ph.D. in Chemistry, University of Central Florida, 2012, Assistant Professor, Department of Chemistry and Life Science.

Thomas M. Spudich, Ph.D. in Analytical Chemistry, Northern Illinois University, 1999, Assistant Professor, Department of Chemistry and Life Science.

Cynthia M. Woodbridge, Ph.D. in Physical Chemistry, University of Nebraska, 2002, Assistant Professor, Department of Chemistry and Life Science.

Rotating Military Faculty

LTC Walter P. Cole, Ph.D. in Optical Sciences, Air Force Institute of Technology, 2008, Assistant Professor, Department of Physics and Nuclear Engineering.

LTC Gregory R. Kilby, Ph.D. in Electrical Engineering, Georgia Institute of Technology, 2005, Assistant Professor, Department of Electrical Engineering and Computer Science.

MAJ John D. Delong, M.S. in Optics, University of Rochester, 2007, Assistant Professor, Department of Physics and Nuclear Engineering.

MAJ Robert P. Grimming, M.S. on Optics, University of Central Florida, 2009, Assistant Professor, Department of Physics and Nuclear Engineering.

MAJ Karl H. Ludeman, M.S. in Physics, University of Minnesota, 2011, Instructor, Department of Physics and Nuclear Engineering.

MAJ Walter D. Zacherl, M.S. in Applied Physics, Stanford, 2007, Assistant Professor, Department of Physics and Nuclear Engineering.

CPT John D. Zehnpfennig II, M.S. in Electrical Engineering, University of Michigan, 2011, Instructor, Department of Electrical Engineering and Computer Science.

Administration

Director	COL James. J. Raftery, Jr.	(845) 938- 5565 or DSN 688-5565
Laboratory Facilities Manager	Ms. Andrea E. Sanborn	(845) 938- 8705 or DSN 688-8705
Facsimile		(845) 938- 3062 or DSN 688-3062

Photonics Research Center
Bartlett Hall, Bldg 753, Room 411
ATTN: MADN-PRC
West Point, New York 10996

Table of Contents

Department of Chemistry & Life Science

Verification of Silver Colloidal Properties for Surface Enhanced Raman Spectroscopic Analysis of Saxitoxins

William F. Pearman*, Christopher Jones*, Kyle Johnson* and Sherwood Hall**

*Photonics Research Center
Department of Chemistry and Life Science
United States Military Academy, West Point, NY 10996

**Food and Drug Administration
HFS-716, CHCB DBC ORS CFSAN
College Park, Maryland 20740

Abstract. Saxitoxins are a family of toxins produced by cyanobacteria and dinoflagellates that are found in both harmful algal blooms (HAB) in the world's oceans and in freshwater lakes. Previous published work established the feasibility of Surface Enhanced Raman Spectroscopy as a viable method for the detection and quantification of the parent toxin, Saxitoxin. Current studies are focused on three saxitoxin derivatives (two 11-hydroxysulfate (GTX2, GTX3) and one N-1- hydroxyl (NEO)). These studies include both the spectral identification of the individual derivatives using SERS and the possible classification of each derivative using multivariate statistical techniques.

Background

Saxitoxins are a family of toxins produced by cyanobacteria and dinoflagellates[1] that are found in both harmful algal blooms (HAB) in the world's oceans[2] and in freshwater lakes[1,3] of which Saxitoxin is the nominal parent. Saxitoxins are naturally produced algal toxins (marine or fresh water) that are often associated with shellfish bed closings and surface water contamination during harmful algal blooms.[1,2,4] Human exposure to this deadly toxin, mostly through the consumption of contaminated shellfish[5], can lead to paralysis, respiratory failure, and/or death. Aside from the obvious health related concerns generated by this toxin, there are also environmental (fish kills, shellfish contamination) and economic (commercial fisheries, recreation and tourism) impacts to consider.[6]

To date several analytical techniques have been utilized to detect saxitoxin. These techniques can be separated into two broad, if not overlapping categories; bioassay and spectroscopic techniques. The current standard for the detection and quantification of aqueous saxitoxin is the mouse injection assay[7] which, though accurate, it is impractical for on site applications and hampered by the need for a large number of live animals.

Raman spectroscopy, specifically Surface Enhanced Raman Spectroscopy (SERS), is an effective technique for the non-invasive analysis of biologically relevant molecules.[8] The normal Raman effect is very weak where only one in $\sim 10^9$ photons will be inelastically or Raman scattered. However, SERS significantly enhances the detectable Raman signal by several orders of magnitude through both electromagnetic and chemical enhancement factors. It is also a rapid technique requiring little sample preparation. Thus, a major benefit of SERS is the ability to qualify and quantify molecules at biologically relevant

concentrations in near real time.[8] Previous work demonstrated the feasibility of using SERS for the detection and quantification of saxitoxin.[9] The current work focuses on studies of three saxitoxin derivatives (two 11-hydroxysulfate (GTX2, GTX3) and one N-1- hydroxyl (NEO)) for SERS analysis. The structures for GTX2, GTX3, and NEO are shown in Figure 1 below.
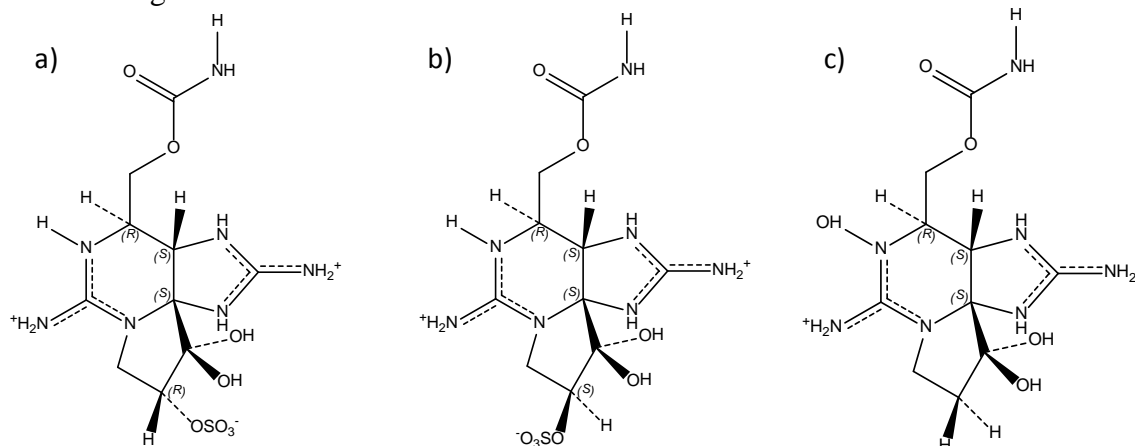

Figure 1. Structures of GTX2 (a), GTX3 (b), and NEO (c)

Experimental

Materials
Stock saxitoxin solutions were made by dissolving solid saxitoxins in 3 mM HCl. All saxitoxin samples were provided by the United States Food and Drug Administration (USFDA). $NaBH_4$, 30 % H_2O_2 and $AgNO_3$ were purchased from Sigma and H_2SO_4 purchased from Fisher Scientific. All reagents were used without further purification or modification. All samples and dilutions were prepared in pure water. Various commercially available silver nano-particles with various capping agents were purchased from nanoComposix.

Instrumentation
An Argon Ion Laser operating at 514 nm was used as the excitation source for this study. The laser energy was delivered to the sample vials via a fiber optically coupled, focused Raman probe (InPhotonics Raman Probe). The collection fiber from the Raman Probe was coupled to a 0.5m spectrometer. Raman spectra were recorded using a 16-bit, TE cooled, CCD. Daily calibrations of the system were performed using cyclohexane. Colloidal particle sizing was performed via dynamic light scattering (Brookhaven Instruments Corp., ZetaPlus Particle Sizing). Finally, UV/VIS spectra of the Ag colloid were obtained using a Jasco V-670 UV/Vis Spectrometer.

Borohydride Stabilized Ag Colloidal Synthesis
All glassware was cleaned using a 4:1 H_2SO_4:30 % H_2O_2 solution prior to colloid synthesis. Borohydride stabilized particles were prepared using a slightly modified procedure originally described by Cermakova et al.[10] Briefly, 150 mL of 1.2 mM $NaBH_4$(aq) was placed in a 250 mL round bottom flask submerged in an ice bath. 20 mL of 2.2 mM $AgNO_3$(aq) was prepared in a separate flask and also chilled in an ice bath. After approximately one half hour, a stir bar was added and the $NaBH_4$ solution was vigorously stirred. The $AgNO_3$ was then added drop wise with the use of a disposable

pipette to the NaBH₄. The balance of the AgNO₃ solution remained in the flask in the ice bath until use. Once added, the drops would turn dark gray, disperse in the NaBH₄, ultimately turning the bulk of the solution a pale yellow. Once all of the AgNO₃ was added, the colloidal solution was removed from the ice bath and stirring was continued for an additional 45 minutes.

Sample preparation
Aqueous dilutions of the stock saxitoxin solutions were performed prior to addition to the Ag colloidal hydrosol. Standard half dram sample vials (Fisher Scientific) were used for both the preparation and the collection of SERS spectra. The SERS samples were all prepared with 800 µL of borohydride reduced silver nanoparticles (AgNPs) that had aged for several weeks. To the AgNP, a 20 µL aliquot of a stock toxin solution was added and vortex mixed for 2 seconds. The final toxin concentrations were on the order of 40 µM.

Results and Discussion
Stabilizing or Capping Agents
This research pursued citrate, PVP, tannic acid, and sodium borohydride capping agents over silver nanoparticles. The following figures show the structure of the various capping agents.
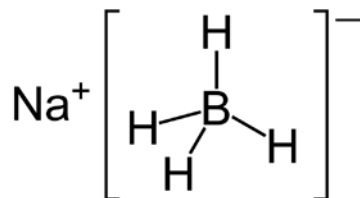

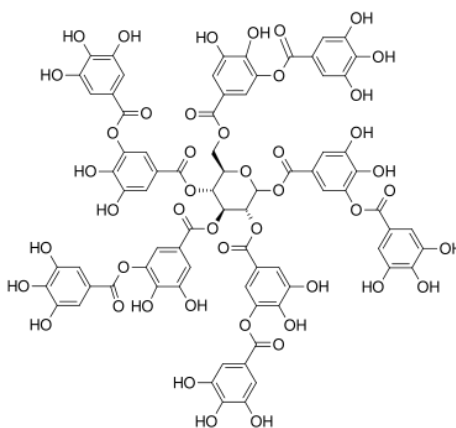**Figure 2**. Sodium Borohydride Nanoparticle Structure

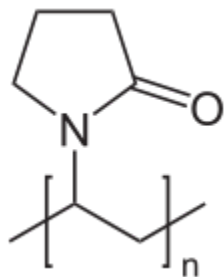**Figure 3.** Tannic Acid Nanoparticle Structure

8

Figure 4. PVP Nanoparticle Structure
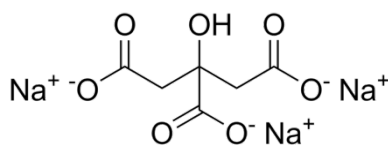
Figure 5. Citrate Nanoparticle Structure

The particle sizes were 30 nm and 60 nm in diameter, except the borohydride stabilized nanoparticle was 60 nm in diameter. After the toxins are introduced to the nanoparticles, the chemical and physical responses between the two particles cause the toxins to form a monolayer around the nanoparticle. Once the monolayer forms, SERS can be used to collect and record representative spectra from the analytes of interest .

Colloidal Parameters
The possible test for saxitoxins involves combining the toxin with a silver nanoparticle and monitoring their chemical and physical interactions. When the toxin is introduced to the nanoparticles, the negative charge of the nanoparticle interacts with the positively charged toxin molecules. Each nanoparticle tested had a zeta potential of 35 mV to 50 mV. The particle sizes were 30 nm to 60 nm. This range of colloidal parameters was determined from previous research.

The following figures are the processed data for GTX with the citrate capping agents with 30 nm and 60 nm silver nanoparticles.

The data in Figure 6 and Figure 7 show that the citrate capping agent on both 30 nm and 60 nm silver nanoparticles do not produce a consistent SERS response. The 30 nm citrate stabilized particles do provide a weak SERS response while the 60 nm citrate stabilized particles do not produce a detectable SERS response. Additionally, the SERS response as shown in Figure 6 is different than those previously collected. It is well know that GTX2 and GTX3 will epimerize and due to the length of time these samples have been in solution, it is little surprise to collect what is actually an equilibrium concentration of both GTX2 and GTX3.
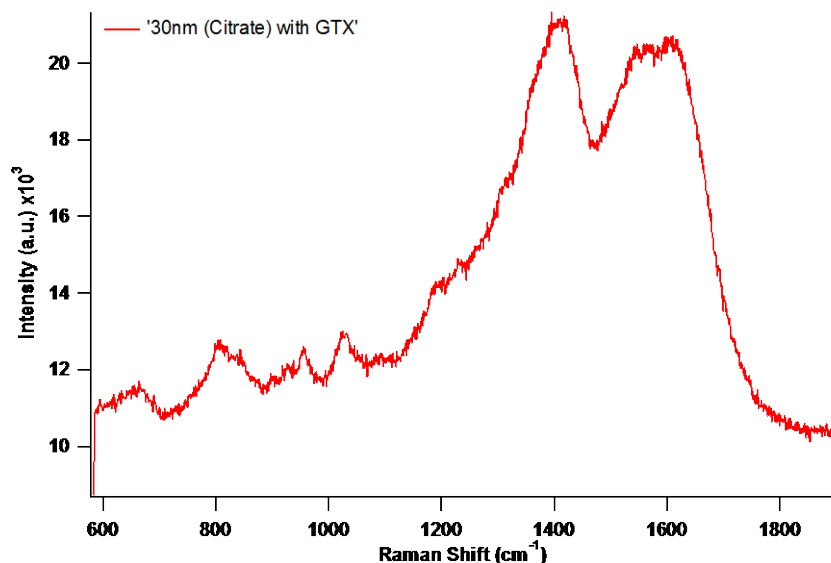
Figure 6. SERS response for 30 nm silver nanoparticle with citrate capping agent and GTX 2/3 analyte
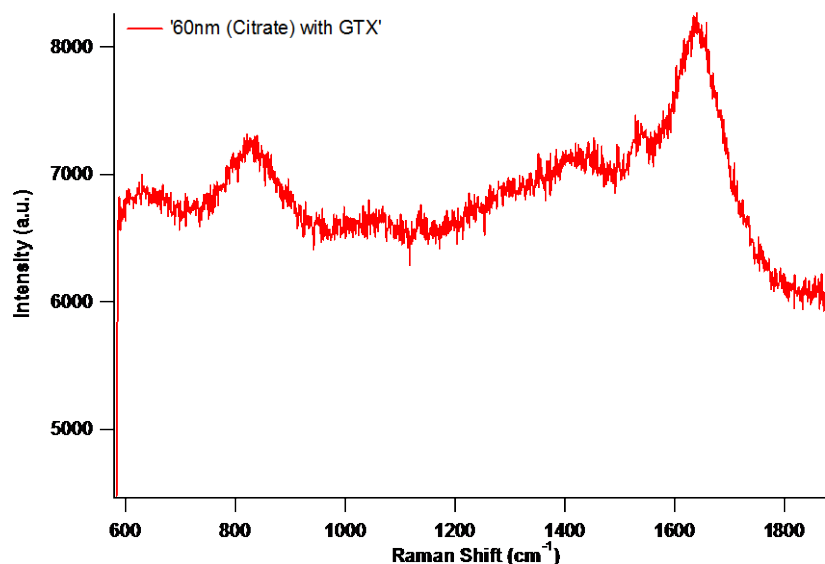
Figure 7. SERS response for 60 nm silver nanoparticle with citrate capping agent and GTX 2/3 analyte.

The same citrate stabilized nanoparticles were also tested in the collection of SERS spectra for NEO. Historically, NEO has demonstrated a propensity to bind to nearly every silver nanoparticle tested regardless of the capping agent of the particles. Figures 8 and 9 below also show that characteristic from this particular study. The SERS response for the 60 nm particle is less intense when compared to the 30 nm spectrum. Furthermore, the SERS response shown in Figures 8 and 9 are identical to those previously recorded in our laboratory.
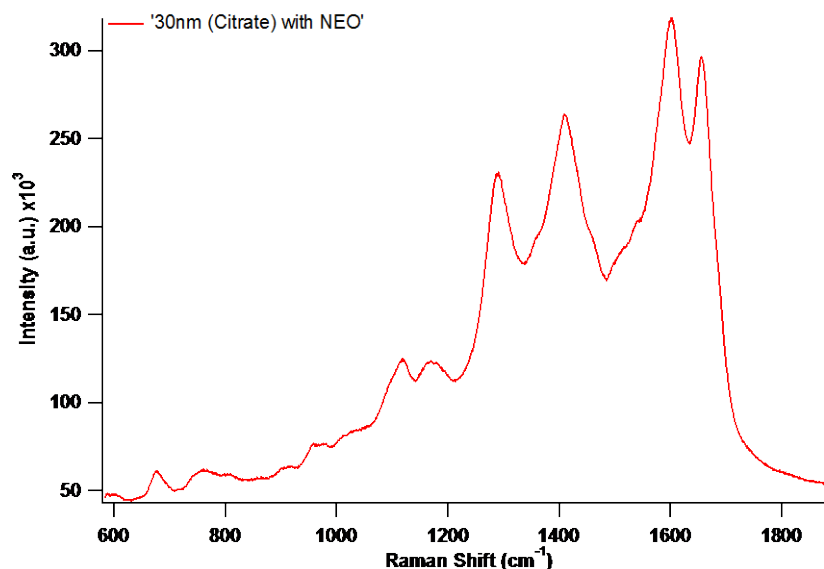
Figure 8. SERS response for 30nm silver colloid with citrate capping agent and NEO.
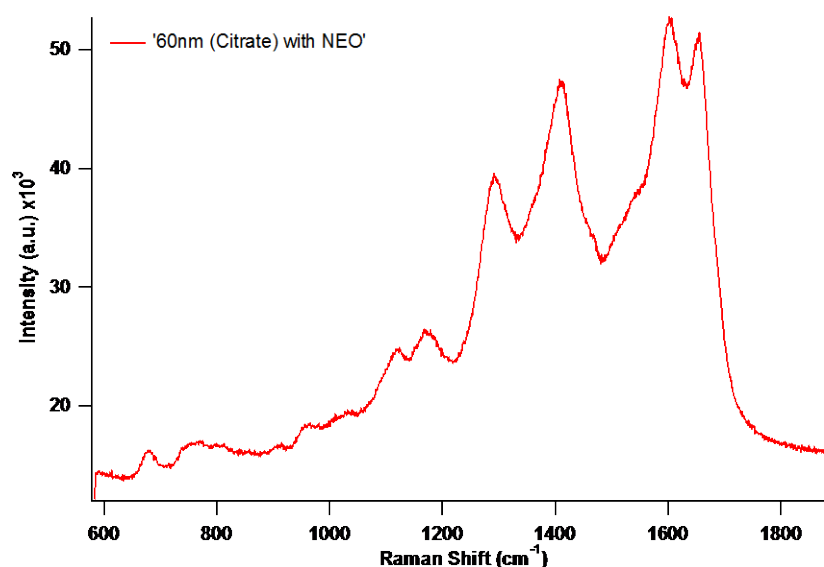
Figure 9. SERS response for 60nm silver colloid with citrate capping agent and NEO.

There are several possible explanations for this change in response, however, effectively doubling the surface area of the silver substrate without a requisite doubling of concentration or varying the preparation to collection timing. To illustrate this concept, the 60 nm citrate/silver nanoparticle underwent a time study where three consecutive spectra each with a total of 1 min integration time were collected from the same NEO sample. Figure 10 shows the SERS response for the three consecutive samples. It is suggested that an understanding of the rate of adsorption of NEO to the particle surface would quantitatively allow for the observed difference in SERS intensity.

11
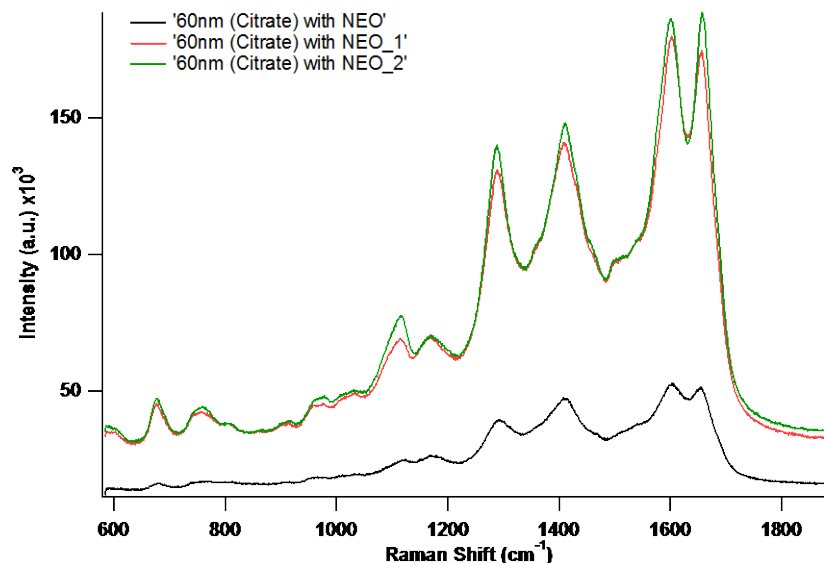
Figure 10. Time Study for 60nm Silver Nanoparticle with Citrate Capping Agent.

In addition to the citrate capping agent, the borohydride stabilized particles were also tested with both NEO and GTX 2/3. The borohydride stabilized particles were synthesized in the laboratory using the borohydride reduction of $AgNO_3$. A 4:1 molar ration of borohydride to $AgNO_3$ has the effect of forced maturation and allows the synthesized nanoparticles to be more selective and responsive to all of the analytes of interest. The borohydride measured 60 nm from DLS data. Figures 11 and 12 show the SERS response between the silver nanoparticle with the borohydride capping agent.
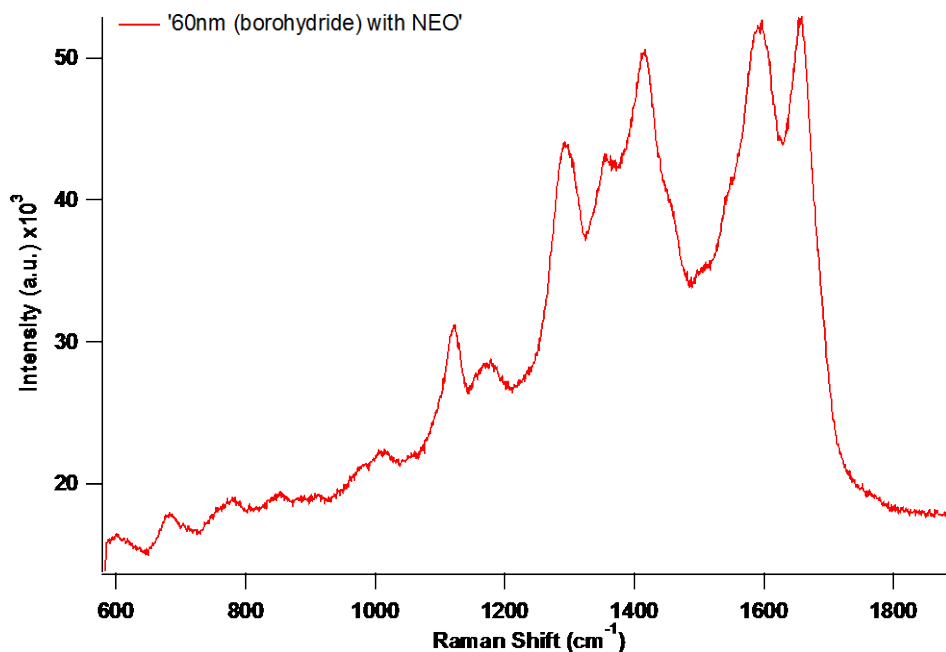
Figure 11. 60nm silver nanoparticle with borohydride capping agent with NEO.

12
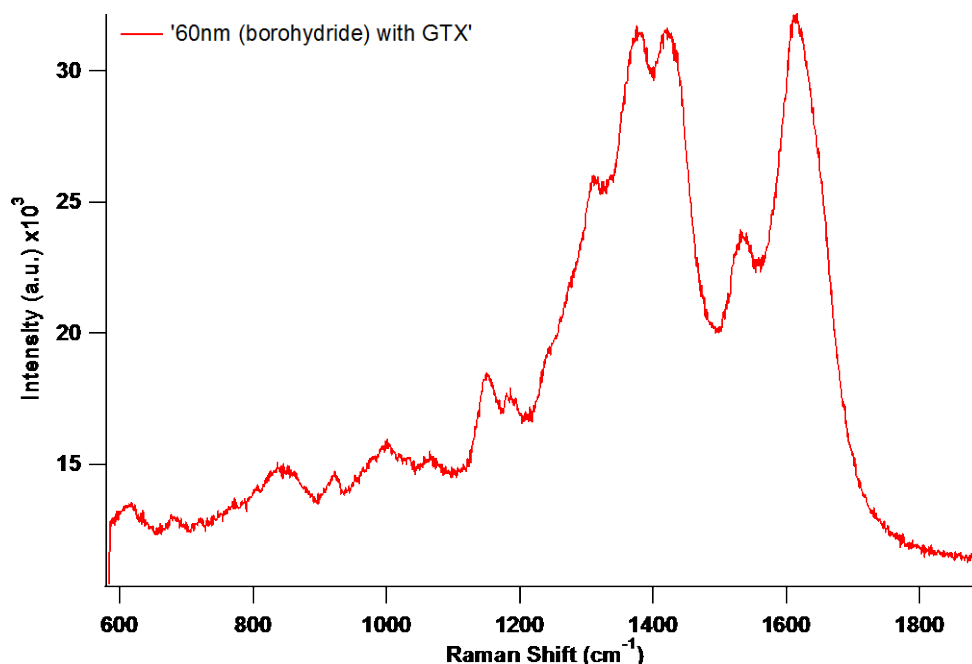
Figure 12. 60 nm silver nanoparticle with borohydride capping agent with GTX.

Once all of the spectra were collected, the colloids were able to be evaluated for their effectiveness with the toxins. The citrate only successfully interacted with NEO. The lack of structure and intensity of the response for GTX and the citrate/silver nanoparticle suggest that the particles interacted, but failed to yield the desired spectra. The spectra resulting from the citrate/silver nanoparticle produced the desired spectra, thus was found to be a successful nanoparticle to be used in a detection test. Both the 30 nm and 60 nm particles were able to produce the desired spectra. At initial mixing, the 30 nm citrate/silver particle produced the most intense signal. The time study was conducted to test if the 60 nm particle would gain in intensity and allow for the monolayer of toxin to form around the particle. Each consecutive sample produced stronger signal intensity. Thus, the size was determined not to be a significant factor in the interaction between the toxin and nanoparticles.

The borohydride/silver nanoparticle was found to be the most successful nanoparticle in interacting with both GTX and NEO. This nanoparticle produced the best responses from both GTX and NEO by producing the desired responses from both toxins. The borohydride/silver colloid response was not as intense as the citrate/silver nanoparticle, but the responses were still resolved and intense enough to distinguish the toxins presence in the nanoparticle solution. While the borohydride failed to yield the best results, it was the most versatile nanoparticle, which made it the most possible nanoparticle for a test.

The other capping agents of tannic acid and PVP failed to yield any usable results. The spectra are not significant enough to provide. Both capping agents are quite large, in comparison to borohydride and citrate. The failure of these nanoparticles add evidence to demonstrate that the size of the nanoparticle was not a significant factor, but the capping

agent proved to be a more substantial factor. The capping agents of tannic acid and PVP were 30 nm in diameter, which is the same size as the successful citrate and borohydride nanoparticles.

Conclusion
The evidence collected from the research suggest that the size of the nanoparticle was not important to the response. Specifically, the time study suggested that the size was not a significant factor. The size of the particle only affected the time necessary for the same intensity to be achieved. This evidence could be due to the larger surface area that is associated with a larger particle. The monolayer around the nanoparticle took longer to form, but given enough time, the proper response was able to be collected.

The results of the testing suggest the capping agent was the most significant factor in successful SERS response from the colloid and toxin solutions. The citrate and borohydride were the two successful capping agents. The tannic acid and PVP capping agents on the same sized nanoparticles failed to yield any successful results. Thus, the capping agent is the most important factor of a nanoparticle interacting with the toxins. The reason for the capping agents failing is not yet known. It is possible that some chemical interaction prevents the saxitoxins from reaching the silver particle and interacting. Also, the size of the capping agent could be an issue. The two failed capping agents were much larger on a molecular level than the successful capping agents. This possible explanation has no definitive evidence collected through research, and is grounds for continued research.

The results from this study suggest 60 nm silver nanoparticles with borohydride capping agents are the most successful nanoparticles to use to detect the presence of saxitoxins in a solution. This data can be used to design a test to detect the presence of saxitoxins in solutions. With more research, the nanoparticle can lead to a standardized method of detecting the saxitoxins present in samples. This could allow for governments to finally be able to detect the dangerous toxin being released from algal blooms. The evidence collected in this study is not conclusive but contributes to the development of such a test.

Cadet/Faculty Involvement
Cadets: Christopher Jones, Kyle Johnson
Faculty Advisor: LTC William Pearman

References
1. Newcombe, G.; Nicholson, B., Treatment options for the saxitoxin class of cyanotoxins. *Water Science & Technology: Water Supply* **2002,** *2* (5-6), 271-275.
2. K. G. Sellner, G. J. D., and G. J. Kirkpatrick, *J. Ind. Microbiol. Biotechnol.* **2003,** *30*, 383.
3. Kaas, H.; Henriksen, P., Saxtioxins (PSP Toxins) in Danish Lakes. *Water Research* **2000,** *34* (7), 2089-2097.

4. M. C. Louzao, M. R. V., J. M. V. Baptista de Sousa, F. Leira, and L. M. Botana, *Anal. Biochem.* **2001,** *289*, 246.

5. M. A. Quillian and J. L. C. Wright, *Anal. Chem.* **1989,** *61* (18), 1053A.

6. P. Hoagland, D. M. A., Y. Karoru, and A. W. White, *Estuaries* **2002,** *25* (4b), 819.

7. AOAC Official Method 959.08, P. S. P.

8. Pearman, W. F.; Lawrence-Snyder, M.; Angel, S. M.; Decho, A. W., Surface-Enhanced Raman Spectroscopy for in Situ Measurements of Signaling Molecules (Autoinducers) Relevant to Bacteria Quorum Sensing. *Applied Spectroscopy* **2007,** *61*, 1295-1300.

9. Pearman, W. F.; Angel, S. M.; Ferry, J. L.; Hall, S., Characterization of the Ag Mediated Surface-Enhanced Raman Spectroscopy of Saxitoxin. *Applied Spectroscopy* **2008,** *62*, 727-732.

10. Cermakova, K.; Sestak, O.; Matejka, P.; Baumruk, V.; Vlckova, B., Surface-Enhanced Raman-Scattering (Sers) Spectroscopy with Borohydride-Reduced Silver Colloids - Controlling Adsorption of the Scattering Species by Surface-Potential of Silver Colloid. *Collection of Czechoslovak Chemical Communications* **1993,** *58* (11), 2682-2694.

Hyperspectral Imaging to Develop Adaptable Near Infrared Camouflage

LTC William F. Pearman and Cadet Michael Vaughn

Photonics Research Center
Department of Chemistry and Life Science
United States Military Academy, West Point, NY 10996

Abstract. The availability of commercial and surplus military night vision optics utilizing generation I and II (GEN I & II) light intensifying technologies has caused an increase in concern of the spectral qualities of camouflage, specifically the near infrared. A field expedient appliqué which allows individuals to match the background spectral response in the NIR can significantly reduce the possibility of detection. Previous studies focused on various commercially available products, paints, and nano materials (gold nanorods) COTS products applied to different patterns and clothing materials. Those results indicated that it was possible to use a NIR absorber to alter the NIR reflectance of the materials, thus decreasing the overall probability of detection. Current research is directed towards the actual application of NIR dyes in a more realistic environment. The dyes were applied on various candidate camouflage patterns and the performance of the dyes were evaluated in the near infrared. The use of such appliqués would allow individuals, with specific mission sets, to apply and assess the effectiveness of these appliqués in the operational area.

Background

Hyper-spectral imaging (HSI) is a powerful sensing technology. Its strength lies in the camera's ability to collect banded spectrum data over a defined area rapidly. HSI output data contains complete banded spectra for each pixel (Figure 1). These individual spectra can be manipulated using any number of algorithms designed for imaging the specific target. HSI output data can be viewed as a two dimensional array like a regular digital photo.

HSI has several advantages over point spectrometer or color pictures. The captured HSI scene contains all the information for calibrating and comparing unknown materials and the background reflectance. There are no errors in color matching because all the information is collected simultaneously. One 30 second scan can provide all the information needed to match test materials against the background under those lighting conditions.

Current hyper-spectral imaging has several limitations. The major drawback is that the HSI image must be collected on site with natural lighting and background. Simulated or modeled background would more than likely miss many subtleties of an actual outdoor scene. The individual spectra are banded resulting in relatively low resolution of individual spectral features. In this application, however, only broad peak identification is needed for imaging purposes. Another weakness to hyper-spectral imaging is that the complete data package is very large. One 640x640 pixel hyper-spectral image is almost 100MB. For our post picture analysis, this is a small limiting factor.
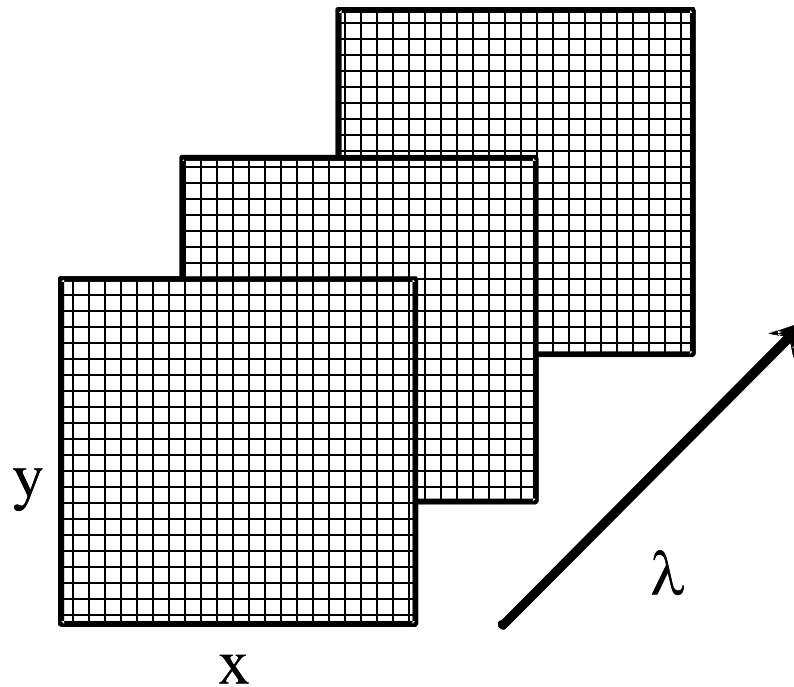
Figure 1: Hyperspectral Data Cube

HSI is a rapidly expanding technology. HSI sensors are being used in many high altitude applications from measuring water content in soil to assessing different tree species in Finland to identifying mineral concentrations in the Californian deserts. Most space exploratory vehicles have an integrated HSI or multispectral sensing system. Hyper-spectral imaging is being used in agriculture to quickly assess produce for disease and ripeness. The technology has been incorporated into microscopes to conduct micro analysis on chemical composition of pharmaceuticals. HSI systems are sold commercially with coverage in increments from UV/VIS to LWIR.

The goal of this project was to use Hyperspectral imaging to provide technical evaluation of camouflage materials and household application sprays with the overall goal to answer the question "What degree does the application of NIR dyes reduce the overall detectability of the candidate patterns?'

Experimental
Materials
Several NIR absorbing COTS dyes were purchased from Fabric Holding Inc. Those dyes have absorbance's at 780 and 880 nm. Two different dyes at 880 nm were chosen based upon their slight differences in thermal and light stabilities.
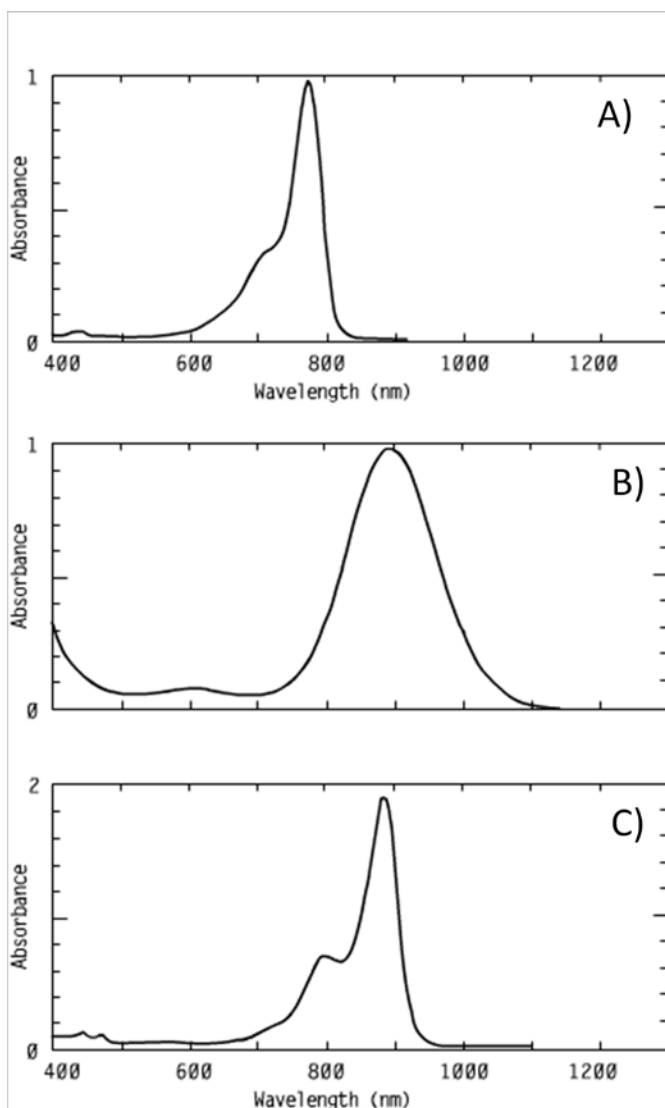
Figure 2: COTS dyes used in this study: A) λ_{max} = 780 nm, B) λ_{max} = 880 nm (high thermal and light stability), and C) λ_{max} = 880 nm (medium thermal and light stability)

Instrumentation
The Hyper-spectral imager used in the study was an OKSI Hyperscan VNIR. The Hyperscan VNIR is a Push-Broom type imager with a spectral range from 390-1060 nm with 520 bands (1.29 nm resolution). Two lenses (70 mm and 35 mm) are available for use with the system. The spectral data is analyzed using ENVI software (ITT Visual Information Solutions).

Results and Discussion
Concentration Ranges and Application Locations
Initial studies were conducted testing the concentrations of dyes that could produce the best results. Concentrations ranged from 1.5 to 0.25 mg/mL at 0.25mg/mL steps. It was determined that the range from 1.0 mg/mL to 0.75 mg/mL worked the best with minimal application density. Lower concentrations have to be applied several times to achieve an

easily measurable response while those concentrations above 1.0 mg/mL were too absorbent and thus too dark.

The application of these dyes onto the camouflaged fabrics was first done by following specific colors of the pattern. For example, once one color from the camouflage fabric was chosen the dye was applied everywhere that particular color was present in such a manner as to exactly follow the pattern on the fabric. It was determined that since most of the individual colors on all of the test patterns were not visible in the NIR and thus it did not matter on which color the dyes were applied.

Blind Field Application and Analysis - Individual Targets
Following the initial laboratory work mentioned above, the $\lambda_{max} = 880$ nm (high thermal and light stability) – (B) from Figure 2 - dye was chosen for test in a field environment. Much time was required to wait for the early spring vegetation to begin to flourish, but an area with evergreens had to be ultimately selected as time requirements were becoming a large issue. Two E-type silhouette targets where covered with two test patterns (Type 2 and Type 3) and a third target was covered with Operation Enduring Freedom Camouflage Pattern (OCP). Dye as applied to one of the fabric covered targets while the other remained as the control. Both the dyed and un-dyed targets were placed randomly into the field of view of the hyperspectral imager and a hyperspectral image was collected. No attempt was made to "check" the performance of the dyed target in the field.

Figure 3. RGB representation for Type 3 pattern without dye (L) and with dye (R).

Upon returning to the laboratory, all of the collected images were analyzed. Part of that analysis was simulating what the field of view would look like under light intensification devices. In an effort to simulate that process, a monochromatic image at 880nm was produced in the ENVI software and then colored with a green tint using the recolor picture tool available in various Microsoft office programs. The result of this process is shown in Figure 4.

19

Figure 4. Simulated image that is roughly equivalent to the scene viewed under light intensification devices.

As can be seen from Figure 4, it is definitely more difficult to find the target on the right of the picture which has had the NIR dye applied in a random, unverified manner. This process is purely qualitative, but does indicate a potential reduction in the ability of a threat sensor's ability to detect this particular target with the NIR dye applied.

For a more quantitative approach, the spectral reflectance of the dyed regions of the target was mapped using the ENVI software package and is described here. First the hyperspectral cube is visualized as a monochromatic image at 880 nm where the absorbance of the dye can be readily identified as shown in Figure 5 (A). From that image, a region of interest or ROI, can be drawn on those areas of the target where the dye is easily identified. The ROIs are shown as the red overlays on Figure 5 (B). The spectral trace from those ROIs (Figure 5 (D)) is then saved as a spectral library. A spectral library matching algorithm is then run to map that particular spectral response across the entire image. The matching algorithm used in this study is Spectral Angle Mapping or SAM. In SAM, a two-dimensional feature space defined by bands x and y and two spectral signatures representing two different surface objects can be represented as vectors v_1, and v_2. The spectral angle θ is the angle between the two vectors v_1, and v_2 i.e.,

$$\theta_{(v_1, v_2,)} = \cos^{-1} \frac{V_1 \; V_2}{\| V_1 \| \| V_2 \|}$$

Therefore, the smaller the spectral angle (θ), the more spectrally similar the two vectors. Figure 5 (C) shows the SAM map for the spectral trace (D) obtained from the dyed portions of the target. For the sake of convention, a SAM image is reversed in a color scheme as to not confuse the average observer. Thus in Figure XX (C), the bright areas demonstrate a better spectral match on a Black to White scale as utilized herein.

20
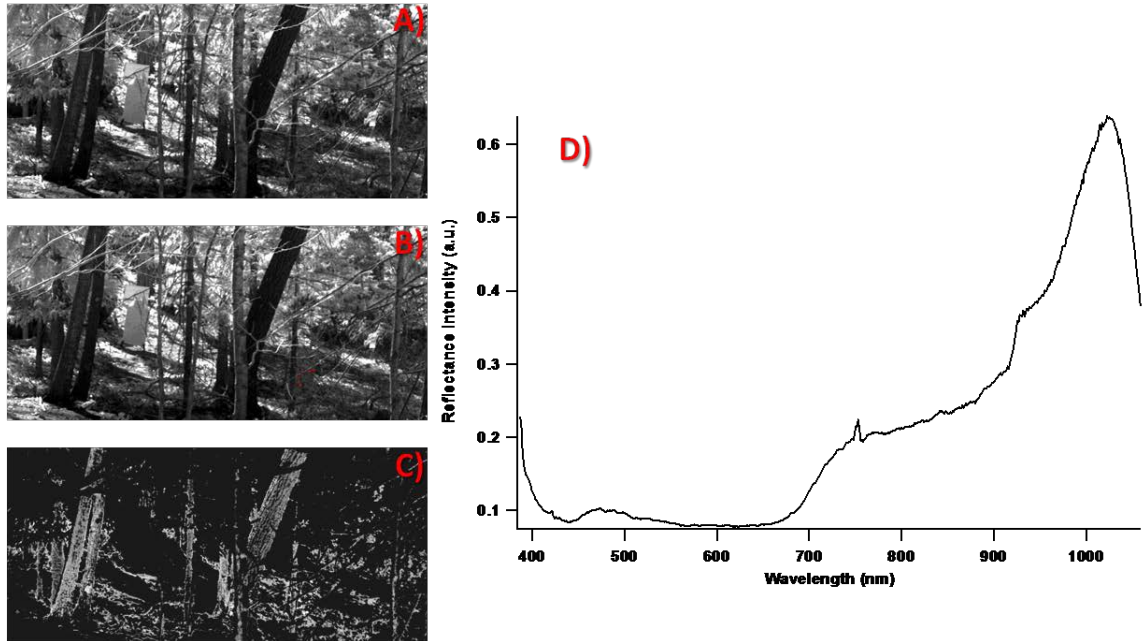
Figure 5. Hyperspectral image displayed as a monochromatic image at 880 nm. Image A) shows the image at 880 nm, B) Dye regions on target selected for analysis (red ROIs), and C) the SAM Map of the spectral response D).

Blind Field Application and Analysis – Life-sized Target
In addition to the E-type silhouette target, a manikin was dressed in a jump suit that was made from the Type 2 pattern. For the field test with this particular target, two different NIR dyes were applied: $\lambda_{max} = 780$ nm and $\lambda_{max} = 880$ nm (high thermal and light stability).

Figure 6. RGB representation for Type 2 pattern on a jumpsuit worn by a life-sized target with two NIR dyes applied (780 and 880 nm).

21

Following the same procedures as described with the E-type silhouette targets, the life-sized target is first evaluated using monochromatic images. However, in this case, two separate dyes were applied and therefore two separate images are presented here in the simulated green light field that would be viewed through light intensification devices.

Figure 7. Green tinted monochromatic images representation for the Type 2 pattern on a jumpsuit worn by a life-sized target at (A) 780 nm and (B) 880 nm.

Following the same SAM process for each of the two wavelengths, 780 and 880 nm, first the reflectance spectra from the dyed regions are collected and a spectral library for both Figure 8 C and D are produced.
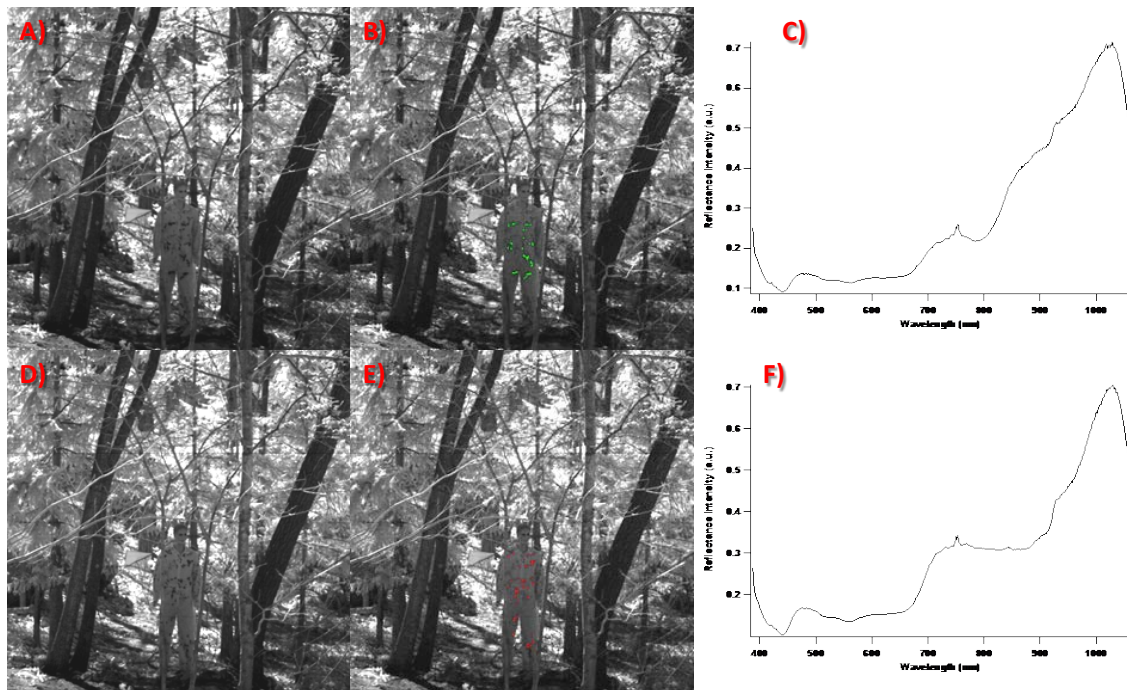
Figure 8 . Analysis of lifelike target at both 780nm (A-C) and 880nm (D-F).

The SAM results are shown in Figure 9. Although not as dramatic as the results shown in Figure 4, the lighter regions of the jumpsuit do represent a good spectral match to the lighter areas of the remainder of the scene. Additionally, the 880 nm SAM image shows

that at the longer wavelength, there is contribution from the 780 nm dyed region of the jumpsuit which does qualitatively reduce the detectability of the overall target.

Figure 9 . SAM classification image for spectra from dyed portions at 780 nm (A) and 880 nm (B).

Conclusions

There does exist the possibility for individual service members, with specific mission sets, to tailor the NIR spectral properties of their individual equipment. This capability has been shown without any on location analysis or basis.

Cadet/Faculty Involvement

Cadets: Michael Vaughn
Faculty Advisor: LTC William Pearman

Acknowledgements

References

Kruse, F. A., Lefkoff, A. B., Boardman, J. B., Heidebrecht, K. B., Shapiro, A. T., Barloon, P. J., and Goetz, A. F. H., 1993, "The Spectral Image Processing System (SIPS) - Interactive Visualization and Analysis of Imaging spectrometer Data". *Remote Sensing of Environment*, v. 44, p. 145 - 163.

Analysis of Biological Systems Using Hyperspectral Imagery

William F. Pearman, J. Kenneth Wickiser, Jaewon Lee, and Christine Sloan.

Photonics Research Center
Department of Chemistry and Life Science,
United States Military Academy, West Point, NY 10996

Abstract. This project used bacterial samples grown on agar plates to create a library of the unique spectral footprints for a particular bacterial strain. Using nearly identical processing flow to those published for mapping of minerals and vegetation, individual bacterial lawns are also mapped by discrete spectroscopic regions. Additional radiation provided by an ultraviolet light emitting diode spot light produced some additional structures with unique spectroscopic signatures. This manuscript focuses on the methodology for analyzing the hyperspectral images, establishment of a spectral library, and the classification of a separate bacterial plate using that same library.

Background

Hyperspectral imaging (HSI) is a powerful sensing technology. Its strength lies in the camera's ability to collect banded spectrum data over a defined area rapidly. HSI output data contains complete banded spectra for each pixel (Figure 1). These individual spectra can be manipulated using any number of algorithms designed for imaging the specific target. HSI output data can be viewed as a two dimensional array like a regular digital photo.

HSI has several advantages over point spectrometer or color pictures. The captured HSI scene contains all the information for calibrating and comparing unknown materials and the background reflectance. There are no errors in color matching because all the information is collected simultaneously. One 30 second scan can provide all the information needed to match test materials against the background under those lighting conditions.

Figure 1: Hyperspectral Data Cube

HSI is a rapidly expanding technology. HSI sensors are being used in many high altitude applications from measuring water content in soil to assessing different tree species in Finland to identifying mineral concentrations in the Californian deserts. Most space exploratory vehicles have an integrated HSI or multispectral sensing system. Hyper-spectral imaging is being used in agriculture to quickly assess produce for disease and ripeness. The technology has been incorporated into microscopes to conduct micro analysis on chemical composition of pharmaceuticals. HSI systems are sold commercially with coverage in increments from UV/VIS to LWIR.

Experimental

Bacterial Samples

For the purpose of this study a HB101 strain of *E. coli* with the pGLO plasmid was the primary analyte of interest. This *E. coli* contained a constitutively active ampicillin resistance cassette and GFP under an arabinose-sensitive promoter. Although not fully discussed here, *B. subtilis sp.* was also available and utilize during various sample collections.

Instrumentation

The Hyperspectral imager used in the study was a OKSI Hyperscan VNIR. The Hyperscan VNIR is a Push-Broom type imager with a spectral range from 390-1060 nm with 520 bands (1.29 nm resolution). Four 4700K D50 illuminate bounced from the 45° mirror which was also used in the optical path of the imager (see Figure 2). Two lenses (70mm and 35mm) are available for use with the system. The spectral data is analyzed using ENVI software (ITT Visual Information Solutions). Illumination in the laboratory was provided by a bank of 4700K D50 illumination lamps and a UV LED spot light (396nm – Edmunds Optics).
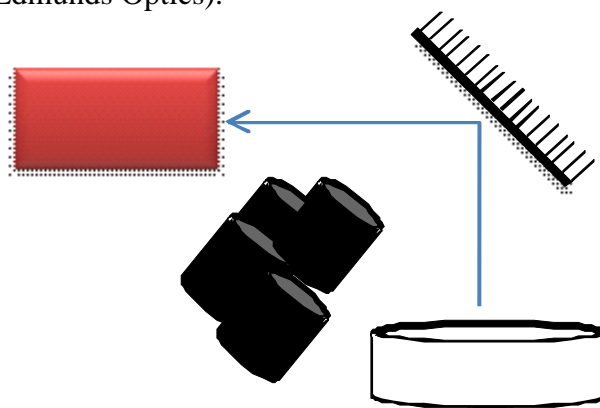
Figure 2. Instrumental and Optical Set-up for collection of hyperspectral images of bacteria
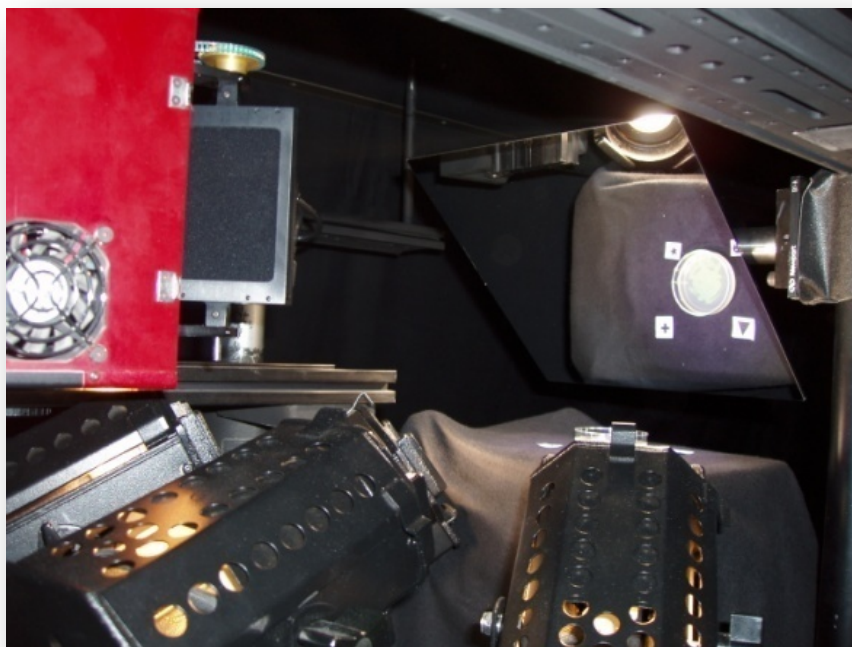
Figure 3: Experimental set-up for collection of Hyperspectral images of bacterial samples

Results and Discussion

Focus and Light Field Optimization

Care was given to optimize all collection parameters prior to the actual collection of an analytical data set. Using a spectralon panel that filled the entire field of view of the imager, the lights were arranged to given as even of distribution of the light field across the projected sample area as possible. This was verified quantitatively by analyzing this image using the ENVI software package and using the contour line overlay of the 525nm line. The contour lines provide directions to adjust the light field coverage across the sample area. A homemade focus target would allow us to optimize the focus of the imager using a small, approximately 3mm, "happy face" as our reference. If the eyes and mouth of the target could be clearly resolved, the imager was thought to be in good focus. This was later verified by the use of a NBS 1963A resolution target.

Radiance to Reflection Conversion

Each analytical collection run consisted of a minimum of three hyperspectral data cubes. The first cube collected was the "bright" cube which consisted of a HSI image of a spectralon panel as previously described, a "dark" cube (shutter closed), and finally the actual analytical cube. All the exposure settings for the imager were established in the collection of the "bright" cube and were not adjusted for the series of analytical cubes that followed. Conversion of the analytical cube from radiance units to reflectance can be accomplished multiple ways in the ENVI software package. For the purpose of these experiments, this conversion was accomplished via spectral math of the "bright" (s2), "dark" (s3), and analytical cube (s1) using the formula shown below:

$$\frac{((float(s1) - float(s3)))}{((float(s2) - float(s3)))}$$

or

Figure 4: Equation utilized for conversion of hyperspectral data cubes from radiance to reflectance units.

Once the analytical cube conversion was complete, a mask was drawn to minimize the spectrally irrelevant contribution for the remainder of the image during future processing.
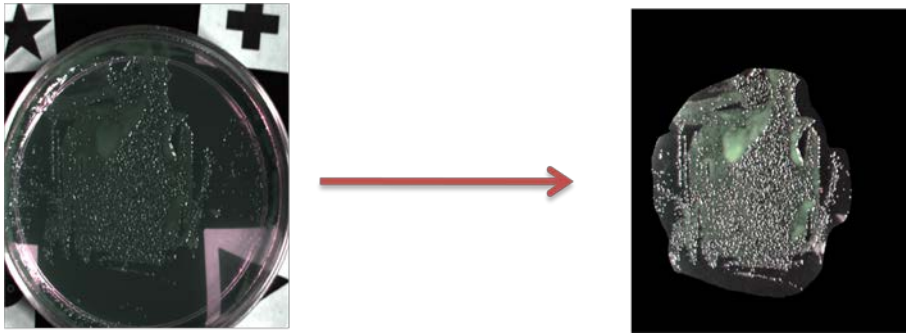
Figure 5: Application of a mask to the converted analytical cube

Spectral Data Transformation
The analytical cube then undergoes a data transformation. The transformation used for this study was the Minimum Noise Fraction (MNF) transformation as modified from Green et.al. The purpose of the MNF transformation is to remove extraneous noise from the image cube. In addition, the processing of the data results in a narrowing of the various MNF bands from hundreds down to ten or less. MNF bands represent the data with extraneous noise removed and the goal is to find the bands that isolate the desired spectral responses. The MNF transform is a linear transformation which is essentially two cascaded Principal Components Analysis (PCA) transformations. The first transformation decorrelates and rescales the noise in the data. This results in transformed data in which the noise has unit variance and no band to band correlations. The second transformation is a standard PCA of the noise-whitened data. Data transformation is necessary to separate the noise for the analytically relevant data and reduce the data set to its true dimensionality.

Reviewing the eigenvalue plot generated during the MNF transformation (Figure 6) allows you to select the MNF bands which contain the most significant spectral information. As the eigenvalue approaches unity, the image becomes dominated by noise. As can be seen from the eigenvalue plot below, as the graph approaches unity at an approximate value of 6, the score is roughly unity. Reviewing the MNF band 6 image reveals an image dominated by pixilated noise.
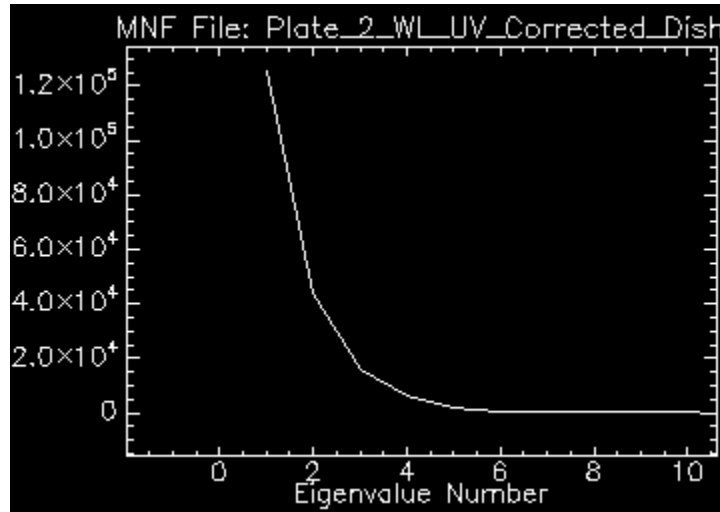
Figure 6. Eigenvalue plot generated during MNF transformation

ENVI allows for the visualization of the MNF bands as an RGB image where the user can designate different MNF bands as red, green and blue. As shown in Figure 7, (a) MNF band 1- designated as 'red', (b) MNF band 2- designiated as 'blue', and (c) MNF band 3 – designated as 'green' produce the MNF RGB image (d) as shown where the colors are indicative of the contribution of the specific areas in the image from the individual MNF bands.
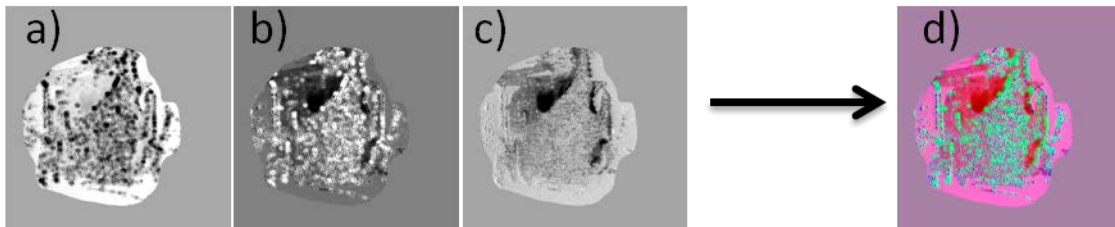
Figure 7. MNF band 1, 2 and 3 images (a, b, and c respectively) are coded as 'red', 'green', and 'blue'. The color composite image (d) shows the contribution from the individual MNF bands

Selection of Spectral Classes
Following MNF transformation, endmembers can be selected based upon the spectral similarity of the individual pixels. From an MNF image, a two dimensional scatter plot can be produced that allows for a quick comparison between two MNF bands simultaneously. Plotting the 2D scatter plots of two such MNF bands allowing for a visual methodology for selecting pixels from the image with similar spectral profiles. Figure 8 below shows a 2D scatter plot for MNF bands 1 and 2 from a sample data set.
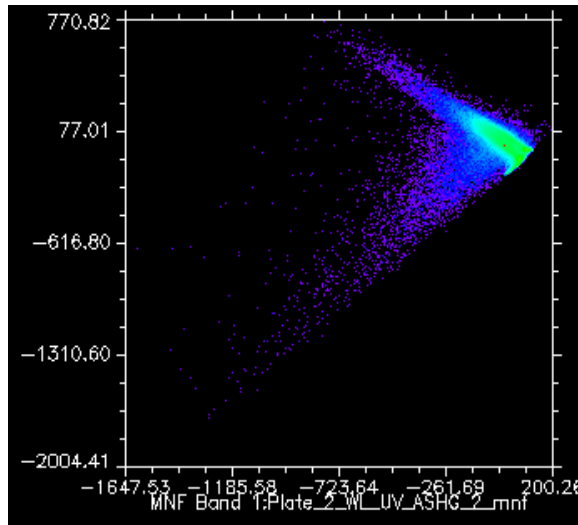
Figure 8. Sample 2D Scatter Plot of MNF Band 1 vs. MNF Band2

ENVI allows the user to query regions or "arms" in the 2D scatter plot that will highlight those pixels within the actual image. This is a good method for selecting classes of pixels with similar spectroscopic responses. From the 2D scatter plot in Figure 8, individual classes are selected and highlighted in different colors on the 2D scatter plot. The same colors are then overlaid on the image and are saved as regions of interest or ROIs. These new class ROIs can then be applied to other HSI images with the same spatial characteristics as the parent image. Figure 9 illustrates this process.
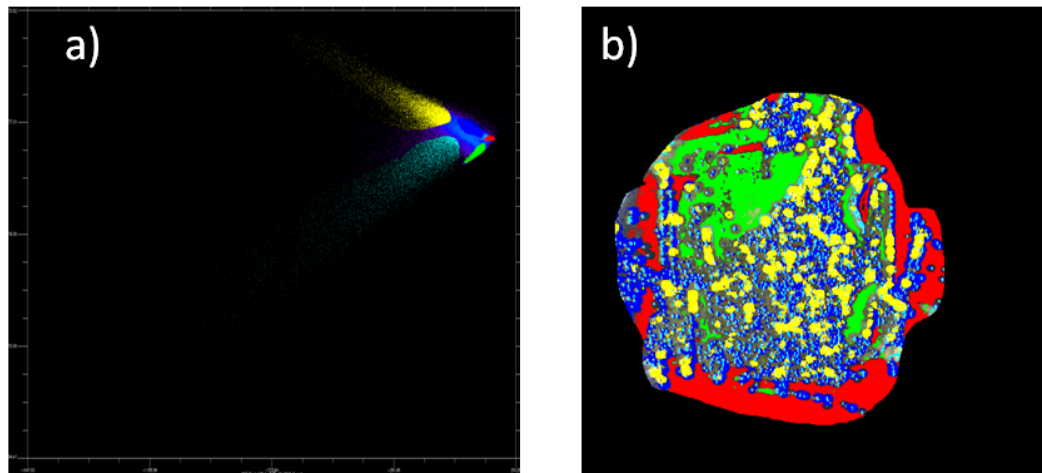
Figure 9. Selection of classes within the 2D scatter plot (a) and the resultant class ROI on the non-transformed HSI Image (b).

Once the individual spectral classes are defined in the process detailed above, the ROIs are then overlaid onto the non-transformed corrected hyperspectral image. This now allows for the collection of average reflectance spectra across all of the pixels identified as a spectral class. The collected spectra can then be saved as a spectral library and used to classify other samples of interest. Figure 10 below shows the average spectrum for each class as identified in Figure 9 above. The colors on the image correspond to the color of the spectral traces.
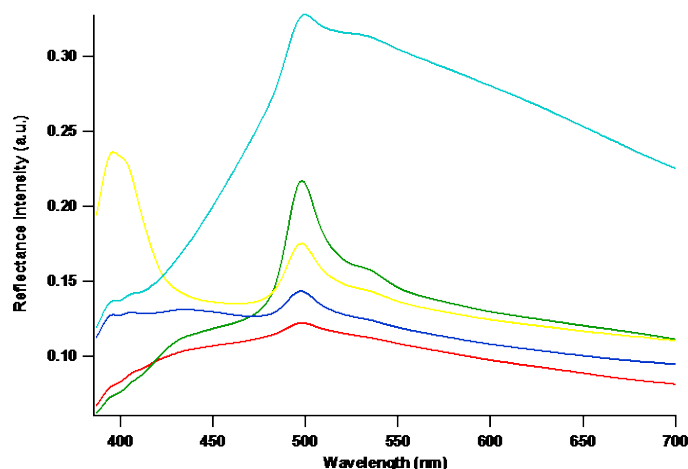
Figure 10. Average spectral traces for the individual regions identified in Figure 9 (b)

Classification of New Hyperspectral Image

The spectral library formed from the spectra shown in Figure 10 is then used to classify a new bacterial plate with the same *gfp* modified *E coli*. The same preprocessing steps are followed as previously described. However, no classes are selected with this new hyperspectral image; instead an automated spectral classification methodology is used. For this study a Spectral Angle Mapper Classification (SAM) (Yuhas et al., 1992) is used for the classification of the new image. SAM is an automated method which directly compares image spectra to known or reference spectra. In this particular case, the reference spectra are those shown in Figure 10. SAM treats spectra, the reference and the unknown spectra from the unclassified image, as vectors and calculates the spectral angle between them. The Spectral Angle Mapper computes a spectral angle between each pixel spectrum and each target spectrum. The smaller the spectral angle, the more similar the pixel and target spectra. This method is insensitive to illumination since the SAM algorithm uses only the vector direction and not the vector length. The result of the SAM classification is an image showing the best match at each pixel. The workflow in ENVI used to accomplish this classification is Target Finding with SAM and BandMax. BandMax rejects background data by determining a subset of spectral image bands that are useful in distinguishing between target and background spectra.
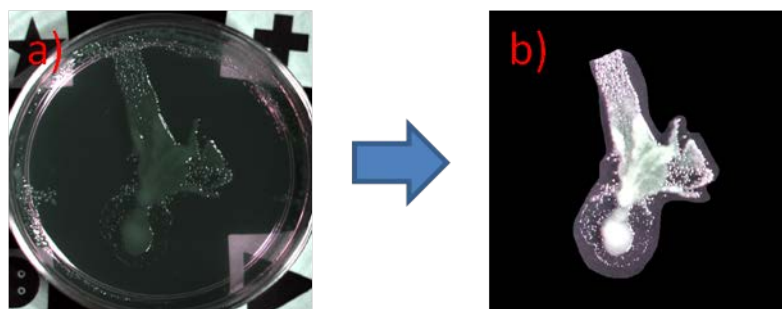
Figure 11. Corrected (reflectance) HSI image (a) and masked HSI image (b) prior to SAM classification

SAM classification creates a so-called "rule" image. The pixel values in the rule images represent the value of the spectral angle between the reference spectrum and each image pixel. These rule images are used in the classification process to assign each image pixel to the defined classes. In our case we use the angle image ("rule" image) in order to discriminate different spectral regions within the bacterial lawn on the unclassified sample plate. ROIs created from these "rule" images

allow for the extraction of spectra from the unclassified sample for further evaluation via other multivariate or statistical analysis techniques.
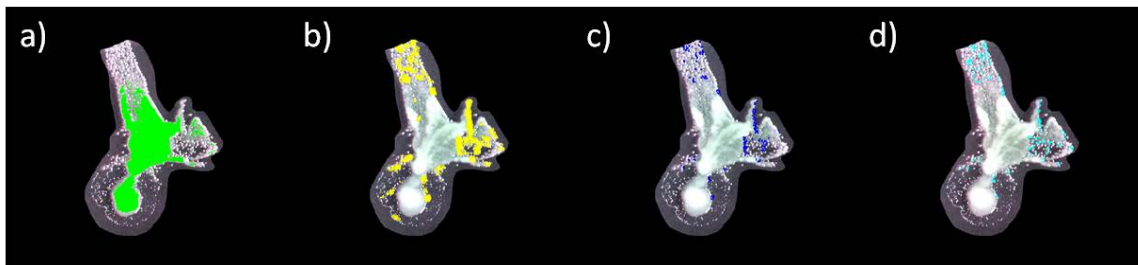
Figure 12. SAM "rule" images applied to new sample plate. The colors of the ROIs on the "rule" images are the same as the colors from the spectral library (Figure 10) and also shown on Figure 9.

Conclusion

This project has verified that the well established methodologies for the analysis of geological hyperspectral images can also be applied to bacterial samples grown on agar plates as small as 1.5" in diameter. The use of the 395nm UV flood produces some very interesting results which need to be further studied. It is not suggested that the collected spectral response will on a specific agar with a specific organism will translate to the same organism grown on different agars, but it suggested that organisms grown under the same conditions on the same agars can produce very similar spectroscopic results.

Cadet/Faculty Involvement

Cadets: Jaewon Lee, and Christine Sloan
Faculty Advisors: LTC William F. Pearman, Dr. J. Kenneth Wickiser

Acknowledgements

References

Kruse, Fred A., "Preliminary Results – Hyperspectral Mapping of Coral Reef Systems using EO-1 Hyperiod, Buck Island, U.S. Virgin Islands," Analytical Imaging and Geophysics LLC

Jun, Won, "Detection of Microbial Biofilms on Food Processing Surfaces: Hyperspectral Fluorescence imaging study," Environmental Microbial and Food Safety Laboratory Agricultural Research Service

Masschelein, B., "Towards a Colony Counting System using Hyperspectral Imaging," NICTA.

Yuhas, R.H., Goetz, A. F. H., and Boardman, J. W., 1992, Discrimination among semiarid landscape endmembers using the spectral angle mapper (SAM) algorithm. In Summaries of the Third Annual JPL Airborne Geoscience Workshop, JPL Publication 92-14, vol. 1, pp. 147-149.

Green, A. A., Berman, M., Switzer, P., and Craig, M. D., 1988, A transformation for ordering multispectral data in terms of image quality with implications for noise removal: *IEEE Transactions on Geoscience and Remote Sensing*, v. 26, no. 1, p. 65-74

Laser Induced Breakdown Spectroscopy: The Past and The Future
Caitlin N. Rinke-Kneapler

Photonics Research Center
Department of Chemistry and Life Science
United States Military Academy, West Point, NY 10996

Abstract. A boom in research involving Laser Induced Breakdown Spectroscopy (LIBS) has been experienced in recent years, despite LIBS presence as a scientific technique for many decades. Precision limitations previously plagued LIBS use in many scientific fields, but recent progress in laser technologies and chemometrics have helped overcome these limitations. The gains that have been made in LIBS analysis have opened the door to many promising applications of LIBS instrumentation in the fields of military, defense, and forensic. Now LIBS demonstrates the capability of being a promising technique for future application to crucial Army missions.

Background

Laser-induced breakdown spectroscopy (LIBS) is an atomic emission spectroscopy technique which provides elemental information based on a plasma generated by a laser source. In recent years Laser Induced Breakdown Spectroscopy, commonly known as LIBS, has stood out as an analytical technique due to its wide range of potential applications. Its simplicity of use and versatility are appealing qualities that have opened the door to its application in many fields. LIBS is an atomic emission technique which performs simultaneous multi-elemental detection for liquid, gas and solid samples. The method provides good sensitivity for many elements with minimal to no sample preparation. The minimal sample preparation is ideal for direct collection which is a desirable quality in many fields including defense, military and forensic.

The basic principles of LIBS are focused around the use of a high-power focused laser. Multiple types of laser can be used in LIBS analysis, but the most common is the Nd:YAG laser. The laser is usually pulsed between 5-10 nanoseconds, though femtosecond lasers have also been explored, to ablate the sample which atomizes and vaporizes samples to produce a plasma of free atomic species, both neutral and ionic [1]. A lens is positioned between the laser and the sample to focus the laser onto the sample, and either a second lens or fiber optic cable is positioned above the sample to collect the plasma light. The collected light is then transported to a frequency dispersive or selective device and then to a detector to produce the sample spectrum.   The setup of LIBS, Figure 1, allows for the capability of stand-off detection. This ability to detect energetic, nuclear or other potentially hazardous compounds at a safe distance is one of the major fields of interest in LIBS research. Recent articles and reviews can be found that demonstrate the needs and progress within LIBS stand-off research for field application, with a few referenced here [2-4].
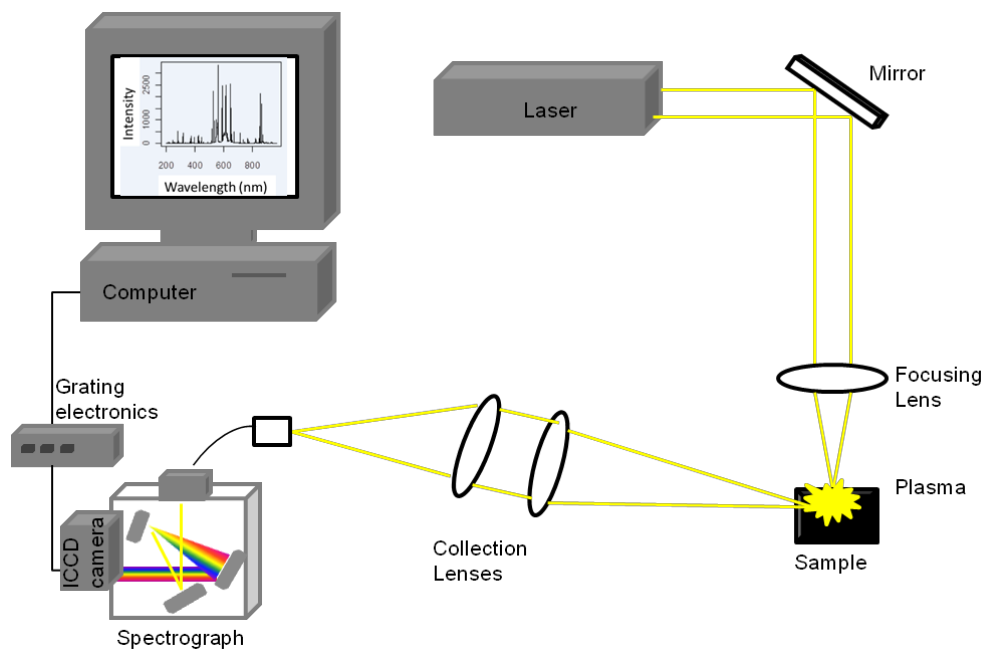
Figure 1: LIBS Components

The current set-back in LIBS applicability is its precision limitations. This issue has been attributed to many potential sources such as: pulse instability, laser pulse, laser-sample interactions, characteristics of the sample and environmental factors [2-4]. Due to this limitation, quantitation of elemental concentration demonstrates a dependence on instrumental, sample and environmental factors. Methods that have been taken to overcome this limitation include: chemometric techniques [2-4], calibration free and controlled calibration LIBS, and femtosecond or double pulse LIBS. Previous work to be discussed and the future research to be investigated focus on the chemometric techniques as will be seen in the following sections. Chemometric techniques that have been applied to LIBS data include principal component analysis, target factor analysis, Bayesian Decision Theory, and many more. Approaching the data analysis with chemometric methods allow multiple random variables and relationships between variables to be incorporated. Factoring in additional parameters allow for patterns within the data to be identified and optimized for improved results.

In the following sections previous LIBS work will be described to demonstrate some of the applications of LIBS, in addition to discuss chemometric methods that are available for data analysis [5-7]. Finally, plans for future research directions will be discussed to incorporate LIBS and chemometric analysis into suitable applications within the Army.

Experimental
Instrumentation [5-8]
The LIBS work was performed using a LIBS2000+, a commercial instrumentation from Ocean Optics (Dunedin, Fl, USA). The system consisted of a 1064nm Nd:YAG Q-switched, pulsed laser (Big Sky Lasers, model CFR200, Bozeman, Montana, USA), with a pulse width of 9 ns. The laser was focused on the sample with a single lens with a focal length of 7.5 cm. A set of bifurcated optical fibers connected to seven linear CCD array

spectrometers were used to collect the emitted light from the plasma in the wavelength range of 198.14 to 965.43nm.

Metal Transfer [7,8]
Six brands of 9mm bullets (5 of each brand) were acquired from a local gun store (East Orange Shooting Sports, Orlando, Fl), listed in Table 1. The type of jacketing was used to group the bullets into three classes: non-jacketed, metal alloy jacketed, and copper jacketed. For each brand of bullet four of the five bullets were fired into a steel plate to create metal transfers. The remaining bullet for each brand was analyzed to create a standard library for each class of bullet to be used in the chemometric analysis.

Table 1: Samples for metal transfer experiment.

Manufacturer	Bullet Type	Jacket
CCI	Blazer	Copper
Independence		Copper
Remington	UMC	Copper
Hornady	Tap (hollow-point)	Copper
Winchester	Silver-Tip (hollow-point)	Metal alloy
Winchester	Hand packed	No jacket (lead)
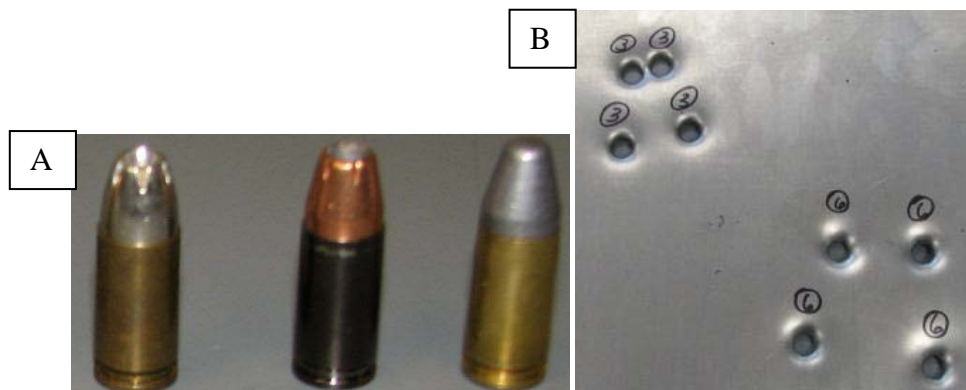
Figure 2: a) Examples of the three classes of bullets used to create metal transfers. b) One of three steel plates after bullets had been fired through to create metal transfers.

LIBS analysis was performed to obtain unknown metal transfers and a standard library of data. The standard library was compromised of six spectra from each of the six unused bullets. Each of the six spectra was an average of ten single-shot spectra. The library was prepared this way to account for the high variability often observed in replicate LIBS spectra. Twelve single shot spectra were collected within each bullet hole to compromise each of the unknown metal transfers. Varying amounts of metal transfer were expected to be observed within each of the unknown samples.

Data was analyzed using a chemometric method which combined three chemometric techniques: principal component analysis (PCA), target factor analysis (TFA) , and a modified Bayesian Decision Theory. PCA derives new latent variables which are linear combinations of the original data to obtain a reduce data set. TFA uses the reduced abstract data from PCA to identify one or more spectra that fall within the same subspace

as the principal components from PCA. Pearson correlation values are obtained from TFA that relate the similarity of the unknown sample to the library classes. The final step, Bayesian Decision Theory, uses the correlation values from TFA to obtain posterior probabilities of an unknown being classified into one of the library classes. Two criteria are set for the Bayesian Decision Theory step: a significance level (0.05 for this research) and a lower correlation cutoff (0.8 for this research). An extensive explanation of the chemometric techniques will not be discussed here, but can be found in reference [7]. The three chemometric steps utilized the standard library and unknown metal transfers to provide a probability of classification of the bullet jacketing group that created the metal transfer.

Results and Discussion
Metal Transfer [7,8]
LIBS spectra for each of the three classes of bullet jackets and the steel plate background are shown in Figure 3. The spectra for copper and metal alloy classes both have emission lines at 324.75 nm and 327.40 nm which are attributed to Cu I transitions. The metal alloy class also contains emission lines at 361.94, 341.48, and 352.45 nm which are attributed to Ni. The non-jacketed class contains emission lines that vary from the other two, with the multiple lines attributed to Pb. While the steel plate background does not contain strong emission lines from Cu I or Pb transitions, it does contain approximately 15 emission lines in common with the bullet classes. Representative spectra of bullet holes created by each of the three classes of bullet are shown in Figure 4. These spectra demonstrate the complexity of the spectral information and the difficulty in identifying contributions from a single bullet class.
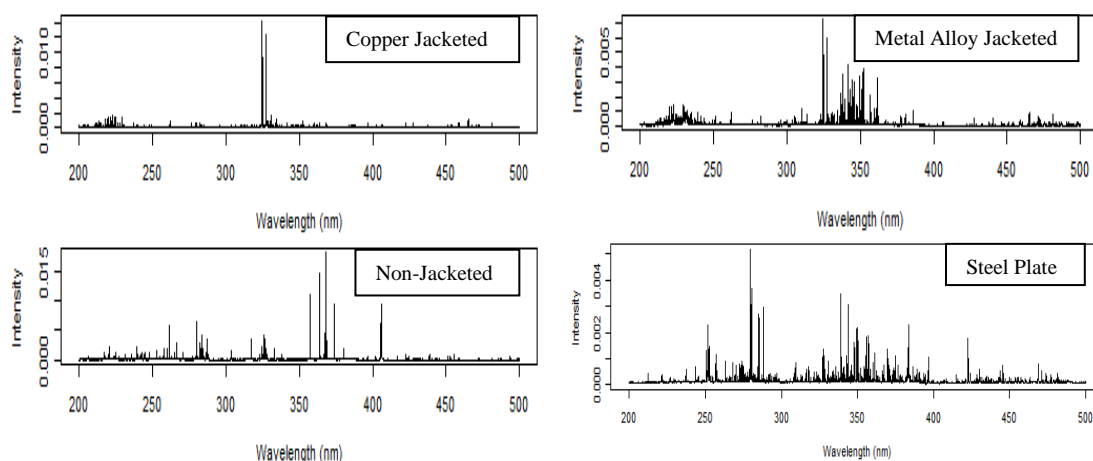
Figure 3: LIBS spectra for bullet jacketing and steel plate.
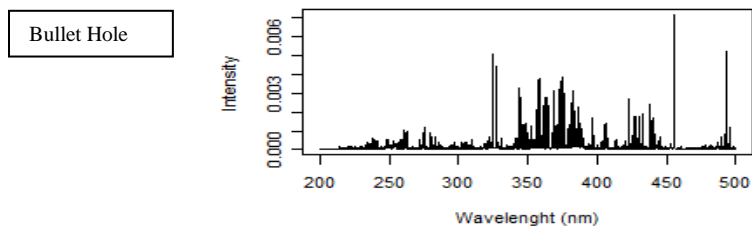
Figure 4: LIBS spectra for bullet hole created in the steel plate by a copper jacketed bullet.

The three step chemometric method was performed to obtain class conditional probabilities to obtain the data shown in the Table 2. The result demonstrated the conservative nature of the data analysis method. From Table 2 it can be seen that there was a large percentage of the bullet holes that had a probability of not being classified based on the two criteria that were set for the chemometric analysis. While leaving samples unclassified is not ideal, it is preferred to misclassification. Of the samples that had a probability for classification, all of the non-jacketed bullet holes and the majority of the copper jacketed(CJ) bullet holes had probabilities of correct classification. The misclassification in the copper jacketed bullet holes was attributed to the steel plate contribution resembling the non-jacketed (NJ) class. The zero probability of classification for the bullet holes created by the metal alloy jacketed (MJ) class was attributed to that jacketing being the hardest metals and least likely to transfer.

Table 2: Probability of classification results for LIBS bullet hole data

Sample	# of Samples	Average Posterior Probability of Classified			Posterior Probability Not Classified
		CJ	MJ	NJ	
CJ	15	0.91	0.00	0.09	0.60
MJ	4	0.00	0.00	0.00	1.00
NJ	4	0.00	0.00	1.00	0.00

.
Additional metal transfer tests were performed to gather results on different backgrounds and multiple transfer scenarios. Complete results can be found in references [7,8] on the additional experiments.

Future Work
The previous work demonstrates examples of LIBS and chemometric analysis for classification and discrimination of known versus unknown samples. Future work will look to expand LIBS technology into areas of Army research that require identification, classification and/or discrimination of samples of interest. The chemistry component of the Photonics Research Center houses a truck portable LIBS system developed during a recent DTRA-NSERC program. The system is set up with a telescope which allows for sample collection at distances ranging from 15-40 m. Numerous research applications are possible with this instrumentation.

Recent interest in using the truck portable LIBS to analyze inorganic and nuclear compounds within environmental settings has been shown. The LIBS instrumentation

provides many useful capabilities for research into this field including its ability to provide elemental information on inorganic compounds at trace levels, simplicity of use, portability, and its capability for stand-off detection for safe distance measurements of potentially hazardous materials. Due to its portability, research can be pursued which encompasses laboratory and field work. The ability to compare laboratory and field work results will provide a more realistic evaluation of the instrumentation by including environmental effects within the data. To handle the complex data matrices and results, chemometric techniques will be applied to provide beneficial information.

Conclusion

Through the previous work LIBS has been demonstrated to be a useful tool for Army related research projects. The versatility and simplicity of use, in addition to the wealth of information obtained illustrate the strong future of LIBS. Broad strides have been made recently to overcome the limitations of LIBS, which have helped to propel its use in many fields of research and into real world applications. Chemometrics and new laser technologies will help LIBS become a means for trace and stand-off detection within many scientific fields including defense, military and forensics.

Cadet/Faculty Involvement:

Dr. Caitlin Rinke-Kneapler, Dr. Nicholas Fell

Currently there are no cadets involved with LIBS research in the PRC but it is hoped within the next semester a few will be brought on board.

Publications

Rinke, C.N., Williams, M.R., Brown, C., Baudelet, M., Richardson, M., Sigman, M.E., *Discriminant Analysis in the Presence of Interferences: Combined Application of Target Factor Analysis and a Bayesian Soft-Classifier*. Analytica Chimica Acta, in press.

Acknowledgements

References

[1]   Cremers, D.A., and Radziemski, L.J., *History and Fundamentals of LIBS*, in *Laser-Induced Breakdown Spectroscopy (LIBS) Fundamentals and Applications*, A.W. Miziolek, Vincenzo, P., and Schechter, I., Editor. 2006, Cambridge University Press: New York.

[2]   Cremers, D.A., and Chinni, R.C., *Laser-Induced Breakdown Spectroscopy-Capabilites and Limitations*. Applied Spectroscopy Reviews, 2009. 44: p. 457-506

[3]   Gottfried, J.L., De Lucia, F.C., Munson, C.A., and Miziolek, A.W., *Laser-Induced Breakdown Spectroscopy for Detection of Explosives Residues: A Review*

of Recent Advances, Challenges, and Future Prospects. Anal Bioanal Chem, 2009. 395: p. 283-300.

[4]   Noll, R., Sturm, V., Aydin, U., Eilers, D., Gehlen, C., Hohne, M., Lamott, A., Makowe, J., and Vrenegor, J., *Laser-Induced Breakdown Spectroscopy-From Research to Industry, New Frontiers for Process Control.* Spectrochimica Acta Part B 2008. 63: p. 1159-1166.

[5]   McIntee, E., Viglino, E., Rinke, C., Kumor, S., Ni, L., Sigman, M.E., *Comparative Analysis of Automotive Paints by Laser Induced Breakdown Spectroscopy and Nonparametric Permutation Tests.* Spectrochimica Acta Part B, 2010. 65: p. 542-548.

[6]   McIntee, E., Viglino, E., Kumor, S., Rinke, C., Ni, L., Sigman, M.E., *Non-Parametric Permutation Test for the Discrimination of Float Glass Samples Based on LIBS spectra.* Journal of Chemometrics, 2010. 24: 312-319.

[7]   Rinke, C.N., Williams, M.R., Brown, C., Baudelet, M., Richardson, M., Sigman, M.E., *Discriminant Analysis in the Presence of Interferences: Combined Application of Target Factor Analysis and a Bayesian Soft-Classifier.* Analytica Chimica Acta, in press.
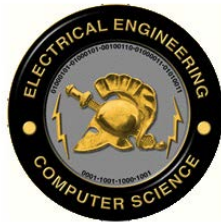
[8]   Rinke, C.N., *Selective Multivariate Applications in Forensic Science.* Diss. University of Central Florida, 2012.

Department of Electrical Engineering & Computer Science

Photonic Crystal Vertical-Cavity Surface-Emitting Laser Research

COL James J. Raftery, Jr., LTC(R) Gregory R. Kilby, COL Lisa A. Shay,
and CPT Janice T. Blane

Photonics Research Center
Department of Electrical Engineering & Computer Science
United States Military Academy, West Point, New York 10996
E-mail: james.raftery@usma.edu

Abstract. Photonic crystal vertical cavity surface emitting lasers have potential applications in areas to include optical interconnects, extended area coherent sources, and steerable beams. This research project expands the body of work in the area of photonic crystal vertical-cavity surface-emitting lasers. Opportunities for junior faculty and cadet involvement are expected in device design and characterization. External contact with government laboratories and university collaborators are expected in these areas and in the area of device fabrication.

Background

The incorporation of a two-dimensional (2D) photonic crystal (PhC) lattice containing a single defect into a distributed Bragg reflector (DBR) of a vertical-cavity surface-emitting laser (VCSEL) has proven to be effective for introducing a precisely controlled index step for lateral optical beam confinement leading to single mode device operation.[1] Such devices are desirable for short-haul optical communication systems, as well as other applications such as light sources for very compact atomic clocks. PhC VCSELs with a single lattice defect have demonstrated single fundamental mode operation at high power (> 3 mW)[2] and at high speed (> 9 Gb/s).[3]

Creating multiple defects in the PhC lattice of a PhC VCSEL has lead to coherently coupled arrays of vertically emitting microcavities producing both out-of-phase[4] and in-phase far field radiation patterns.[5] It has been found that the phase difference between these emitting defect cavities can be tuned with injection current, and can result in an electronically steerable beam as observed in the far field radiation pattern.[6] Coherently coupled 2D arrays of vertically emitting lasers offer the potential of extended area coherent sources with high spectral purity, useful in a variety of applications, such as electronically steerable laser sources for spectroscopic sensing or navigation vision systems for unmanned ground systems.

The activity reported here is a natural extension and continuation of Army supported work which began at the University of Illinois at Urbana-Champaign (UIUC) and was partially supported by award number DAAD19-03-1-0299. PRC involvement in this project began in the fall of 2005 with personnel support. PRC funding support for this project started in the second quarter of FY2007. From this time and into 2009, significant characterization apparatus and modeling capabilities have been added to the project. Experimental apparatus to measure the light, voltage and current (LIV) characteristics and the optical spectra of the devices were constructed and validated with the existing characterization equipment of our collaborator at the University of Illinois at Urbana-Champaign. Additionally, a far-field camera system was constructed and similarly validated to experimentally evaluate the far field characteristics of PhC VCSELs. Finally, a simulation capability using the commercial finite difference time domain (FDTD) software Optiwave has been added to the project.

Just three months after the November 2009 Technical Review, the laboratory that contained the PhC VCSEL experimental set-ups was unexpectedly breached during Phase 1 of the multi-year renovation project to create the Science Center. Dust and dirt infiltrated this lab and made operation of the equipment impossible. After the room's integrity was re-established, an extensive cleaning effort was undertaken to bring the experimental apparatus back online. As research was to resume in the summer of 2010, another breach of the lab occurred. The equipment was wrapped in plastic and sealed shut with tape to protect it from the dust and dirt. The separation from the construction zone was not repaired to a level that allowed work in the main lab to resume. PRC efforts were therefore focused on projects that could be supported from lab space in other parts of the facility. This impact was mitigated by CPT Janice Blane joining the Photonics Device Research Group at Illinois in the summer of 2011 en route to joining the USMA faculty in summer 2013. The lab space available could not accommodate the PhC VCSEL work. In January of 2012, the PRC moved into new laboratory space in the Science Center. The PhC VCSEL characterization set-ups have been relocated to this new space and are in the process of set-up. Continuation of research for PhC VCSEL enabled dynamically steerable optical beams, and a possible extension to low energy-per-bit optical interconnects using PhC VCSELs optimized for this application, are both very promising to extend the state-of-the-art and provide opportunities for scholarly activity to both faculty and cadets.

Theory
This basic research project has several topic areas which are being investigated within the PRC: computational modeling and simulation, device design, and characterization. These research tasks, along with the fabrication of devices outside of USMA, will allow for the completion of parametric studies aimed at achieving a better understanding of the underlying physics involved. Experimental results will be used to improve and validate the models. In turn, it is expected that these improved models will lead to successively better designs, resulting in enhanced device performance and capability. Several fundamental principles are involved, such as, coherence effects, coupled-cavity theory, optical and electrical properties of semiconductor devices, and distributed computing.

Computational Modeling & Simulation
One of the aspects of this research project has been to establish computational capabilities that will permit full three-dimensional (3-D) simulation of PhC VCSEL devices. Up to this point, computational efforts within this project have been primarily focused on simulations used to gain a better understanding of collected data. Commercial software packages have been run on a single personal computer and have been able to provide useful results in a reasonable amount of time (less than one hour of run time). For example, simulations calculated using the beam propagation method yielded insight into relative phase differences of emitting array elements as observed in the measured far field radiation patterns. While this information is useful, simulations that will provide useful design information on devices are not available with this limited computational capability. To obtain this type of information, a PhC VCSEL requires a fully three-dimensional (3D) calculation, as once the PhC lattice is added, the device has no useful symmetries to simplify calculations. Specifically, the nano-scale physical features of the alternating layers of the DBR layers and the finite etch depth of the PhC holes should be included in any calculation that would be expected to influence design choices.

To accomplish 3-D simulations, a server with dual quad-core 64-bit processors and the Optiwave OptiFDTD software package was installed in the Department of Electrical Engineering and Computer Science server room. The devices are iteratively built and simulated in the software. The software displays the 3-D Discretized Fourier Transform (DFT) for the center wavelength and a given polarization (Fig. 1) and the far-field calculation of the radiated field (Fig. 2). Simulated results also include a 2-D spectral response of the radiated field (Fig. 3). Despite the large computing capability, device simulations still take several days to complete.

The computation is used to determine the theoretical device performance. Devices with satisfactory simulation results are then compared to actual devices with the same design specifications. Current simulations are investigating the effect of hole depth and the terminating point of the PhC etch pattern in relation to the DBR layers. Future studies include adjusting the design parameters based on simulation results for various hole depths, variances associated with the PhC periodic lattice, and the width of the oxide window.
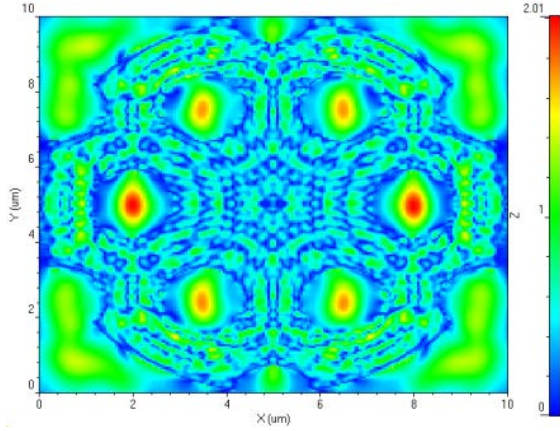
Fig 1. 3-D DFT of the simulation results using the Optiwave OptiFDTD software package for a single defect PhC-VCSEL.
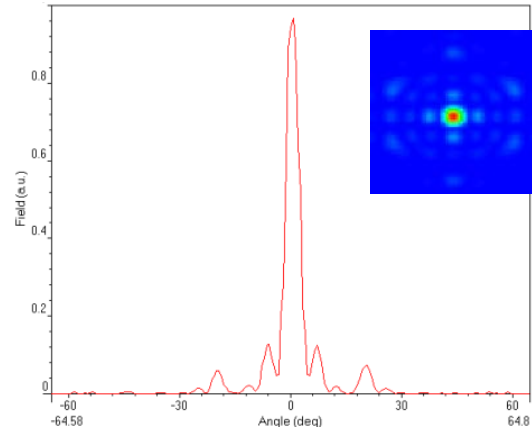
Fig 2. Far-field radiation calculation (inset shows 3-D pattern) using simulated data for the single defect PhC-VCSEL.
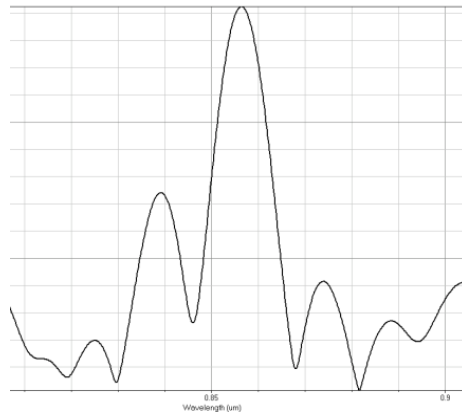
Fig 3. Spectral response using simulated data for the single defect PhC-VCSEL.

42

Device Design

This research task requires a computer-aided-design (CAD) software package which can run on a personal computer. The commercial software package L-Edit is being used. The necessary files required for device fabrication can be generated by PRC researchers and provided to external collaborators for fabrication.

Experimental Device Characterization

Characterization apparatus was constructed and validated in the original PRC laboratory spaces. These set-ups are being re-established in the new PRC laboratories in the Science Center. To measure near field radiation data of PhC VCSELs (fig 4), spectral data (fig 5), optical power data, and electrical (voltage and current) characteristics of the devices (fig 6), a Cascade-Microtech M150 optical probe station system was built. The necessary instrumentation for these measurements has been integrated to facilitate the collection of an entire data set on a particular device once the operating point has been selected.
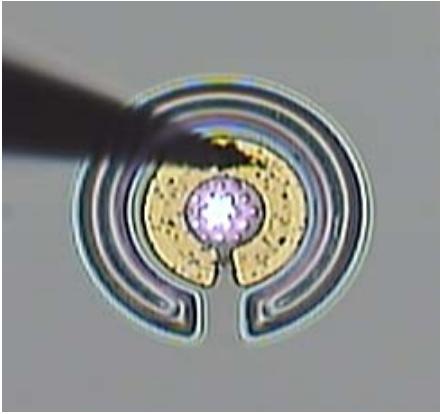
Fig 4. Near-field radiation pattern of a PhC-VCSEL sample with a single defect in the PhC lattice.
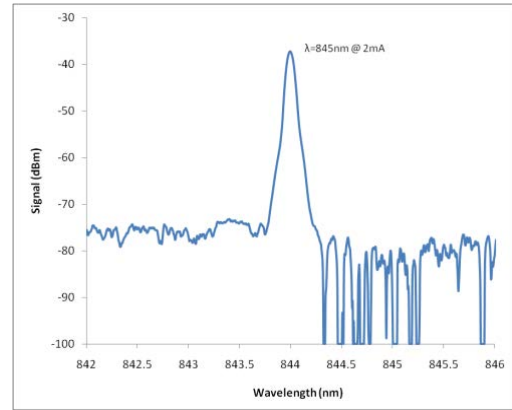
Fig 5. Spectral response of the single defect PhC-VCSEL collected using an optical spectrum analyzer.

Additionally, an experimental set-up for measuring far field radiation patterns (fig. 7) has been assembled using a Photon Inc. LD-8900 Goniometric Radiometer.
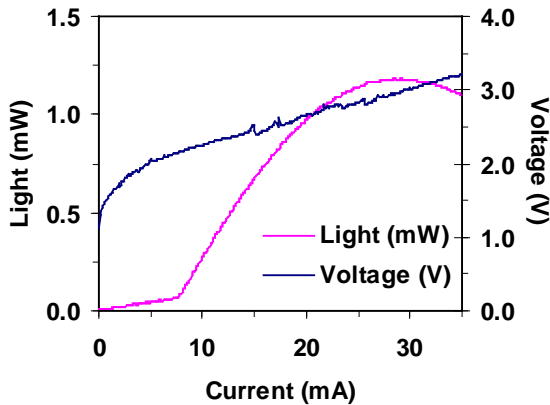
Fig 6. Automated data collection of the light and voltage versus current (LIV) characteristics using NI LabVIEW
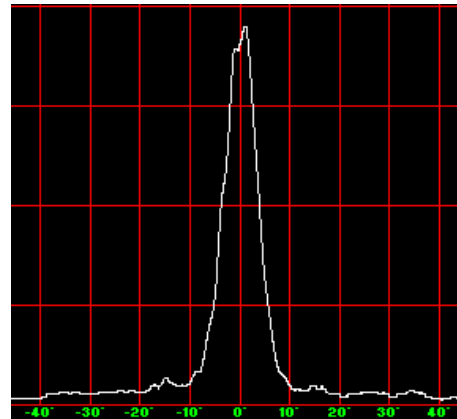
Fig 7. Far-field radiation data of the single defect PhC-VCSEL (inset shows 3-D pattern) collected using a goniometric radiometer.

The measurements from all experimental apparatus was validated by obtaining measurements on devices is the PRC lab and confirming the measurements with data recorded on the same devices from our collaborator's lab. This process will be undertaken again to re-establish this capability.

Results and Discussion
A number of noteworthy findings have resulted from this work to date, to include out-of-phase and in-phase coherent coupling in 2x1 and 2x2 arrangements of defect cavities in PhC VCSELs. These were the first such reports of these achievements. A parametric study of 100 2x1 defect cavity devices was conducted, achieving 95% device yield and leading to the discovery that the relative phase difference between the emitted beams varied with injection current. Devices were also observed to tune with current between coupled and uncoupled states. These results have lead to further discoveries related to coherence and visibility between cavities, and to observed electrical beam steering. A confirmation of the contribution of this work to the discipline is seen by the number of publications and technical presentations listed below. Of particular note is the invited technical article titled "Mode Control in Photonic Crystal Vertical-Cavity Surface Emitting Lasers and Coherent Arrays " in 2009 in the *IEEE Journal on Selected Topics in Quantum Electronics*, and most recently, a review article published in 2012 titled "Single Mode Photonic Crystal Vertical Cavity Surface Emitting Lasers," appearing in *Advances in Optical Technologies*.

Future Direction
The near term goal for this project is to re-establish the device characterization capabilities within the new PRC Science Center laboratory space in order to renew collaborative experimental ties with Prof. Choquette's Photonics Device Research Group (PDRG) at the University of Illinois at Urbana-Champaign. Communications have not ebbed during the proceeding period of renovation dictated experimental inactivity, as is evident by the 2012 review article mentioned above. From these discussions, several exciting possibilities for direction of future work include PhC VCSEL enabled dynamically steerable optical beams and/or low energy-per-bit optical interconnects using VCSELs optimized for this application. Discussions to determine interest in these areas with agencies such as the Missile Defense Agency and the National Security Agency have been initiated. Collaboration with the PDRG is expected to continue long term. With device characterization and device layout being an inherent strength of the PhC VCSEL program within the PRC, we can contribute to parametric studies that will lead to a better understanding of the underlying physics and to enhanced device performance and capabilities. It is the goal of this research project to provide the mechanism to include USMA faculty and cadets in meaningful scholarly activities leading to recognized contributions to the discipline. Ultimately, a transition of this basic research to an applied or developmental program supporting national defense is the goal.

Faculty Involvement
COL James J. Raftery, Jr., Ph.D.   July 2005 to June 2007; June 2011 to present (at USMA)
COL Lisa A. Shay, Ph.D.   August 2006 to January 2010
LTC Gregory R. Kilby, Ph.D.   May 2006 to January 2011
MAJ Kirk A. Ingold   August 2007 to August 2009
CPT Janice T. Blane   August 2011 to present

Publications

17. K. D. Choquette, D. F. Siriani, A. M. Kasten, M. P. Tan, J. D. Sulkin, P. O. Leisher, J. J. Raftery, Jr., and A. J. Danner, "Single Mode Photonic Crystal Vertical Cavity Surface Emitting Lasers," (review article) Advances in Optical Technologies, vol. 2012, Article ID 280920, 8 pages, doi:10.1155/2012/280920 (2012).

16. D. F. Siriani, M. P. Tan, A. M. Kasten, A. C. Lehman, P. O. Leisher, J. J. Raftery, Jr., A. J. Danner, and K. D. Choquette, "Mode Control in Photonic Crystal Vertical Cavity Surface Emitting Lasers and Coherent Arrays (invited)," J. Sel. Topics. Quan. Electron. 15. pp. 909-917 (2009).

15. A. C. Lehman, J. J. Raftery, Jr., P. S. Carney, and K. D. Choquette, "Coherence of Photonic Crystal Vertical Cavity Surface Emitting Laser Arrays," IEEE J. Quantum Electron., vol. 43, no. 1, pp. 25-30 (2007).

14. A. C. Lehman, J. J. Raftery, Jr., and K. D. Choquette, "Photonic Crystal Vertical Cavity Surface Emitting Laser Arrays," J. Modern Optics, vol. 53, nos. 16-17, pp. 2303-2308 (2006).

13. P. O. Leisher, A. J. Danner, J. J. Raftery, Jr., D. Siriani, and K. D. Choquette, "Loss and index guiding in single mode proton-implanted holey vertical-cavity surface-emitting lasers," IEEE J. Quantum Electron., vol. 42, pp. 1091-1096 (2006).

12. J. J. Raftery, Jr., A. C. Lehman, A. J. Danner, P. O. Leisher, A. V. Giannopolous, and K. D. Choquette, "In-Phase Evanescent Coupling of Two-Dimensional Arrays of Defect Cavities in Photonic Crystal Vertical Cavity Surface Emitting Lasers," Appl. Phys. Lett., vol. 89, p. 081119 (2006). (see also Virtual Journal of Nanoscale Science & Technology, vol. 14, no. 10, 2006).

11. K. D. Choquette, J. J. Raftery, Jr., and A. C. Lehman, "Beam Steering in Photonic Crystal Vertical Cavity Semiconductor Laser Arrays," IEEE Aerospace Conference Proceedings (2006).

10. A. J. Danner, J. J. Raftery, Jr., P. O. Leisher, and K. D. Choquette, "Single Mode Photonic Crystal Vertical Cavity Lasers," Appl. Phys. Lett., vol. 88, p. 091114 (2006). (see also Virtual Journal of Nanoscale Science & Technology, vol. 13, no. 10, 2006).

9. J. J. Raftery, Jr., A. C. Lehman, A. J. Danner, P. O. Leisher, A. V. Giannopoulos, and K. D. Choquette, "Coherent Transverse Coupling in Photonic Crystal Vertical Cavity Lasers," C. Lei and K. D. Choquette, Editors; Proc. SPIE 6132, Vertical-Cavity Surface-Emitting Lasers X, 61320I (2006).

8. A. C. Lehman, J. J. Raftery, Jr., A. J. Danner, P. O. Leisher, and K. D. Choquette, "Relative Phase Tuning of Coupled Defects in Photonic Crystal Vertical-Cavity Surface-Emitting Lasers," Appl. Phys. Lett., vol. 88, p. 021102 (2006). (see also Virtual Journal of Nanoscale Science & Technology, vol. 13, no. 3, 2006).

7. P. O. Leisher, J. J. Raftery, Jr., A. M. Kasten, and K. D. Choquette, "Etch Damage and Deposition Repair of Vertical Cavity Surface Emitting Lasers," J. Vac. Sci. Tech. B, vol. 24, pp. 104-107 (2006).

6. Y. K. Kim, A. J. Danner, J. J. Raftery, Jr., and K. D. Choquette, "Focused Ion Beam Nanopatterning for Optoelectronic Device Fabrication" IEEE J. Sel. Topics in Quan. Elect., vol. 11, pp. 1292-1298 (2005).

5. P. O. Leisher, A. J. Danner, J. J. Raftery, Jr., and K. D. Choquette, "Proton Implanted Single Mode Holey Vertical-Cavity Surface-Emitting Lasers," Electron. Lett., vol. 41, pp. 1010-1011 (2005).

4. J. J. Raftery, Jr., "Vertical Cavity Surface-Emitting Lasers Operating with Multiple Photonic Crystal Defect Cavities," University of Illinois at Urbana-Champaign, Ph.D. Dissertation, (2005).

3. J. J. Raftery, Jr., A. J. Danner, J. C. Lee, and K. D. Choquette, "Coherent Coupling of Two-Dimensional Arrays of Defect Cavities in a Photonic Crystal Vertical Cavity Surface Emitting Lasers," Appl. Phys. Lett., vol. 86, p. 201104 (2005).

2. A. J. Danner, J. J. Raftery, Jr., T. Kim, P. O. Leisher, A. V. Giannopoulos, and K. D. Choquette, "Progress in Photonic Crystal Vertical Cavity Lasers," (invited) IEICE Trans. Electron., vol. E88, pp. 944-950 (2005).

1. K. D. Choquette, J. J. Raftery, Jr., A. J. Danner, and P. O. Leisher, "Coherently Coupled Photonic Crystal Vertical Cavity Lasers for Communication Applications," IEEE Aerospace Conference Proceedings, 1-7 (2005).

Technical Presentations

12. K. A. Ingold, L. A. Shay and G. R. Kilby, "Hole Depth Studies in Single-Defect Photonic Crystal Vertical-Cavity Surface-Emitting Lasers Using 3-D FDTD Simulations," Frontiers in Optics: The 93rd OSA Annual Meeting, Optical Society of America., San Jose (Oct 2009).

11. K. A. Ingold, L. A. Shay and G. R. Kilby, "The Optical and Electronic Characteristics of Photonic Crystal Vertical-Cavity Surface-Emitting Lasers," Frontiers in Optics: The 92nd OSA Annual Meeting, Optical Society of America., Rochester, NY (Sep 2008).

10. G. R. Kilby and J. J. Raftery, Jr., "Photonic Crystal VCSEL Characterization," APS/AAPT NYSS 2007 Spring Meeting, West Point, NY, USA (Apr. 2007).

9. J. J. Raftery, Jr., G. R. Kilby, A. C. Lehman, K. D. Choquette, "Coherent Coupling in Photonic Crystal VCSELs," APS/AAPT NYSS 2007 Spring Meeting, West Point, NY, USA (Apr. 2007).

8. J. J. Raftery, Jr. and G. R. Kilby, "A Modified Single Defect Cavity Study for Coherent Coupling in Photonic Crystal VCSELs," Frontiers in Optics the 90th OSA Annual Meeting/Laser Science XXII, Rochester, NY, USA (Oct. 2006).

7. J. J. Raftery, Jr., A. J. Danner, A. C. Lehman, P. O. Leisher, A. V. Giannopoulos, and K. D. Choquette, "A Parametric Study of Coherent Coupling in Photonic Crystal VCSELs with 2x1 Arrangements of Defect Cavities," CLEO (Conference on Lasers and Electro Optics), Long Beach, CA, USA (May 2006).

6. P. O. Leisher, D. F. Siriani, J. J. Raftery, Jr., A. J. Danner, K. D. Choquette, "Loss and Index Guiding in Single-Mode Holey Vertical-Cavity Surface-Emitting Lasers," CLEO (Conference on Lasers and Electro Optics), Long Beach, CA, USA (May 2006).

5. A. C. Lehman, J. J. Raftery, Jr., and K. D. Choquette, "Coherence and phase variation in coupled 2x1 photonic crystal VCSEL arrays," CLEO (Conference on Lasers and Electro-Optics), Long Beach, CA, USA (May 2006).

4. K. D. Choquette, J. J. Raftery, Jr., and A. C. Lehman, "Beam Steering in Photonic Crystal Vertical Cavity Semiconductor Laser Arrays," IEEE Aerospace Conference, Big Sky MT, USA (Mar. 2006).

3. J. J. Raftery, Jr., A. C. Lehman, A. J. Danner, P. O. Leisher, A. V. Giannopoulos, and K. D. Choquette, "Coherent Transverse Coupling in Photonic Crystal Vertical Cavity Lasers," SPIE Photonics West Conference, San Jose, CA, USA (Jan. 2006).

2. P. O. Leisher, A. J. Danner, J. J. Raftery, Jr., and K. D. Choquette, "Proton Implanted Single Mode Holey Vertical Cavity Surface Emitting Lasers," IEEE/LEOS (Lasers and Electro-Optics Society) 18th Annual Meeting, Sydney, Australia (Oct. 2005).
1. K. D. Choquette, A. J. Danner, J. J. Raftery, Jr., "Single Mode Photonic Crystal Vertical Cavity Lasers and Arrays," (invited) Frontiers in Optics the 89th OSA Annual Meeting/Laser Science XXI, Tucson, AZ, USA (Oct. 2005).

References
[1] N. Yokouchi, A. J. Danner, and K. D Choquette, "Two-dimensional photonic crystal confined vertical-cavity surface-emitting lasers," IEEE Journal of Selected Topics in Quantum Electronics, vol. 9, no. 5, 1439-1445 (2003).
[2] A. J. Danner, T. S. Kim, and K. D. Choquette, "Single fundamental mode photonic crystal vertical cavity laser with improved output power," Electronics Letters, vol. 41, no. 6, 325-326 (2005).
[3] T. S. Kim, A. J. Danner, D. M. Grasso, E. W. Young, and K. D. Choquette, "Single fundamental mode photonic crystal vertical cavity surface emitting laser with 9 GHz bandwidth," Electronics Letters, vol. 40, no. 21, 1340-1341 (2004).
[4] J. J. Raftery, Jr., A. J. Danner, J. C. Lee, and K. D. Choquette, "Coherent Coupling of Two-Dimensional Arrays of Defect Cavities in a Photonic Crystal Vertical Cavity Surface Emitting Lasers," Appl. Phys. Lett., vol. 86, p. 201104 (2005).
[5] J. J. Raftery, Jr., A. C. Lehman, A. J. Danner, P. O. Leisher, A. V. Giannopolous, and K. D. Choquette, "In-Phase Evanescent Coupling of Two-Dimensional Arrays of Defect Cavities in Photonic Crystal Vertical Cavity Surface Emitting Lasers," Appl. Phys. Lett., vol. 89, p. 081119 (2006). (see also Virtual Journal of Nanoscale Science & Technology, vol. 14, no. 10, 2006).
[6] A. C. Lehman, J. J. Raftery, Jr., A. J. Danner, P. O. Leisher, and K. D. Choquette, "Relative Phase Tuning of Coupled Defects in Photonic Crystal Vertical-Cavity Surface-Emitting Lasers," Appl. Phys. Lett., vol. 88, p. 021102 (2006). (see also Virtual Journal of Nanoscale Science & Technology, vol. 13, no. 3, 2006).
[7] J. J. Raftery, Jr., A. J. Danner, A. V. Giannopoulos, E. C. Shyu, and K. D. Choquette, "In-Phase Coherently Coupled 2D Arrays of Defect Cavities within a Photonic Crystal VCSEL," (invited) CLEO (Conference on Lasers and Electro-Optics), Baltimore, MD, USA (May 2005).
[8] E. Miyai, K. Sakai, T. Okano, W. Kunishi, D. Ohnishi, and S. Noda, "Photonics: Lasers producing tailored beams," Nature, vol. 441, no. 7096, 946 (2006).

Photonics for Analog-to-Digital Conversion And Multidimensional Image Processing

Eugene K. Ressler, Wenli Huang and Barry L. Shoop

*Department of Electrical Engineering and Computer Science
and Photonics Research Center,
U.S. Military Academy, West Point, NY 10996*

Ashish Tripathi [†] and Augustus W. Fountain III [‡]

[†] Science Applications International Corporation, Aberdeen Proving Ground, MD 21010
[‡] Edgewood Chemical Biological Center, Aberdeen Proving Ground, MD 21010

Abstract. This project is a continuation of the effort to extend the performance of analog-to-digital (A/D) conversion using photonic techniques and the application of a neural algorithm to multidimensional image processing applications. Applications of high-performance A/D conversion are found in many sectors but those requiring the highest performance A/D converters are found in defense, with electronic warfare and radar applications requiring the highest performance. Limitations on high-performance A/D conversion are generally bounded by aperture jitter and comparator ambiguity. Photonics offers a number of advantages over traditional electronic A/D conversion including high-speed sampling, low sampling jitter, optical sampling of optical signals, no electrical-optical signal coupling, parallelism and extended dimensionality including the use of intensity, phase, polarization and wavelength. Extensions include multidimensional image processing for color halftoning and Raman chemical imaging.

Background

The analog-to-digital (A/D) interface is generally considered to be the most critical part of any signal acquisition and processing system. Because of the difficulty in achieving high-resolution and high-speed A/D converters, this A/D interface has been and continues to be a barrier to the realization of high-speed, high-throughput systems. There continues to be interest in new and innovative approaches to A/D conversion, with a significant emphasis on both biologically-inspired and photonic techniques. Our contributions in this area have been to understand traditional oversampling A/D conversion techniques and the relationship with biologically-inspired A/D conversion and apply this understanding to a distributed approach to A/D conversion which holds promise to improve A/D performance.

Biologically-inspired A/D conversion considers the performance of an A/D architecture inspired by the coordinated neuronal firings of biological systems. These neural connections cause statistical temporal patterns in the summed output of the network, which result in enhanced spectral noise shaping and improved signal to noise ratio performance. Our research has involved the study of neural network signal and image processing as applied to A/D conversion. We have shown that the coordinated neuronal firings of biological systems allow for low-noise processing and transmission of analog signals through a network of coupled neurons. Our analysis has further shown that the inherently high noise levels associated with biological neurons are mitigated over a specific frequency range using a network of interconnected neurons that cause statistical temporal patterns in the summed output of the network resulting in spectral noise shaping and improved signal to noise ratio performance. We have also shown that the statistical behavior of the network is a result of self-organization which can be enforced by design.

We have investigated a biologically motivated A/D architecture employing a large numbers of slow, imprecise conversion paths that holds promise in extending the conversion speed and resolution beyond that of current A/D converters. Traditional A/D performance improvements rely on faster clocks and improved timing accuracy in a small number of precisely calibrated components. Unfortunately, A/D converter improvement has not kept pace with conventional VLSI and, in fact, is approaching a fundamental limit due to transistor switching speeds. Other strategies to obtain higher sampling rates have used multiple slower A/D converters arranged in parallel or channelized configurations. The performance of these systems, however, is fundamentally limited by timing error and mismatch effects. In the biologically inspired A/D converter, the system operates asynchronously and is not dependent on either precise timing or accurate voltage comparisons to achieve high-resolution A/D conversion. In fact, analogously to stochastic resonance, the system is inherently nonlinear and requires randomness to achieve optimal system performance. The performance enhancements occur because we have essentially increased the sampling rate by the size of the network. In effect, the oversampling ratio is a product of the time oversampling and the spatial oversampling, where the spatial oversampling is proportional to the number of neurons in the network.

Theory and Calculations: Multidimensional Image Processing
Digital image halftoning is an important class of A/D conversion within the context of image processing. Halftoning can be thought of as an image compression technique whereby a continuous-tone, gray-scale image is printed or displayed using only *binary-valued* pixels. This particular technique has important applications to Army users in such areas as transmission of high-resolution maps and images to battlefield locations using tactical communication links and facsimile. Error diffusion is one method of achieving digital halftoning in which the error associated with a nonlinear quantization process is diffused within a local region and subsequent filtering methods employed in an effort to improve some performance metric such as signal-to-noise ratio. Classical error diffusion is a one-dimensional, serial technique in that the algorithm raster scans the image from upper-left to lower-right and as a result, introduces visual artifacts directly attributable to the halftoning algorithm itself. A fully-parallel implementation of the error diffusion algorithm, however, provides the advantage that all pixel quantization decisions are computed in parallel and therefore the error diffusion process becomes two-dimensional and symmetric. Visual artifacts attributable to the halftoning algorithm are eliminated and overall halftoned image quality is significantly improved. An optoelectronic implementation of the error diffusion algorithm is one approach to this fully-parallel implementation. In addition to attributes already identified, the inherent parallelism associated an optical implementation reduces the computational requirements while decreasing the total convergence time of the halftoning process.

Previously we developed a new artificial neural network architecture based on the mathematical foundation of the error diffusion algorithm, which we call an *error diffusion neural network*. One significant advantage of this new implementation is that arbitrary size and shape diffusion kernels can be implemented thereby reducing the visual artifacts which have become characteristic of halftoned images. This can be accomplished with no penalty in terms of computation speed. The error diffusion neural network computes the halftoned image asymptotically faster than a conventional Hopfield-type neural network. The error diffusion neural network also provides full-rank connectivity across the entire image whereas other error

diffusion techniques only provide local error diffusion. We have quantitatively compared the resulting halftoned images with those produced using other halftoning techniques using performance metrics such as the radially averaged frequency spectrum and anisotropy of continuous-tone gray-scale images. The halftoned images that result from this new halftoning process are currently the *best* halftoned images available, producing artifact-free images.

We extended the fundamental concepts of two-dimensional, symmetric error diffusion to other promising image processing applications. We demonstrated the applicability of our error diffusion neural network to color halftoning, demonstrating excellent color image reproduction while simultaneously achieving a modest image compression ratio of 8:1. Figure 1 shows the results of this error diffusion network to color halftoning.
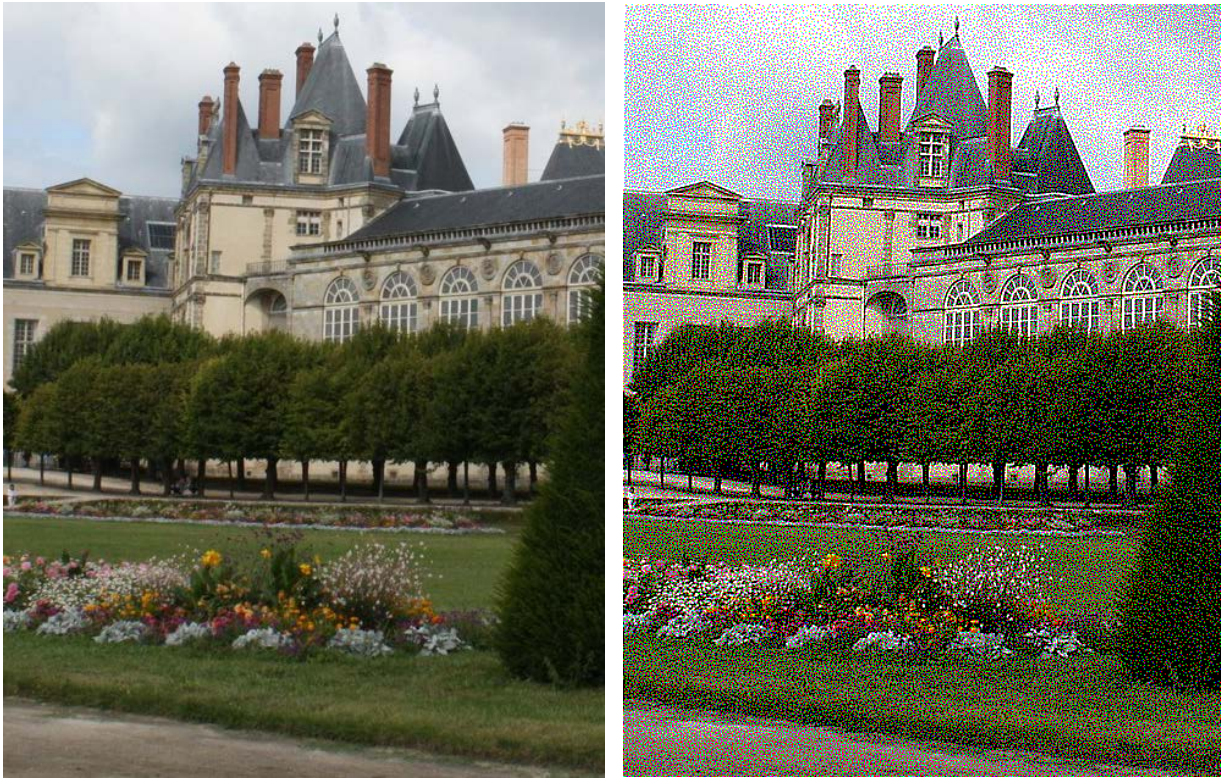
(a) (b)

Figure 1. Color halftoning using an error diffusion neural network. (a) Original color image of the Fontainebleau, and (b) halftoned color image.

The results shown in Figure 1 were achieved by simply implementing three independent error diffusion networks in parallel, one for each of the primary colors in the image. Figure 2 shows results for color halftoning on a 517×398 SPOT image achieved using the same approach. The original image in Figure 2(a) contains 24 bits/pixel and is 610 kbytes in size while that of the color halftone in Figure 2(b) contains 3 bits/pixel and is 77 kbytes in size. This is a fairly substantial reduction in storage and communication bandwidth while maintaining image quality.

(a)   (b)
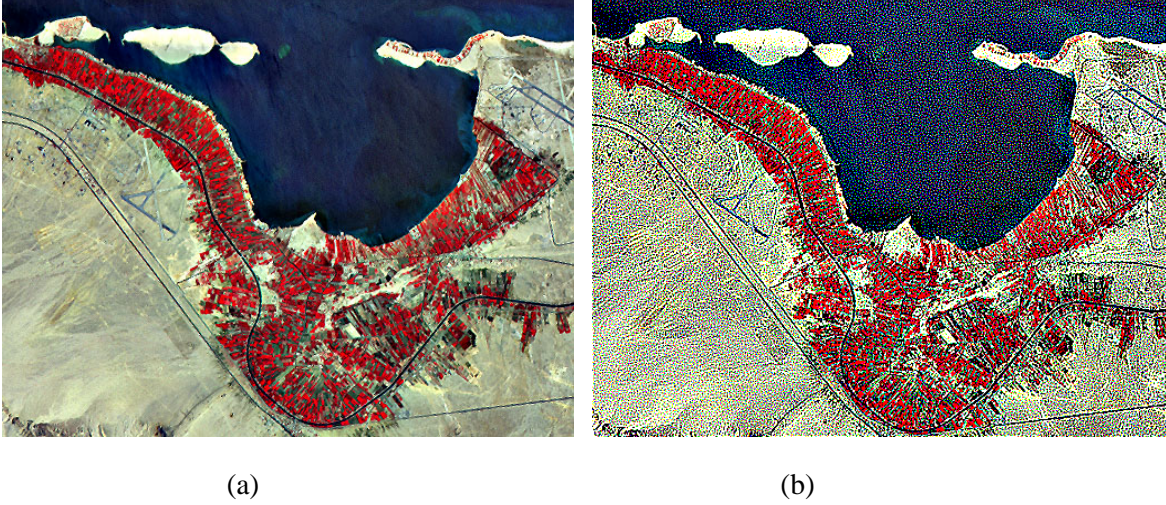
Figure 2. Color halftoning using an error diffusion neural network. (a) Original color image (24 bits/pixel), and (b) halftoned color image (3 bits/pixel).

The halftoning algorithm is a function, $y=h(x)$, where x is a discretely sampled, real-valued input. Values of x are drawn from $[0,1]$. The corresponding binary output, y, is drawn from $\{0,1\}$. By convention, zero is black and one is "as bright as possible" for the output device. A halftone algorithm is considered good if it produces good halftoned images. We consider the function $E(x,y)$ defined as the sum of squares of spatial frequency-weighted error between x and y and a low value of E is equivalent to a good halftone. Thus the algorithm that achieves minimum E for a given x is optimal. Figure 3 shows the block diagram of an error diffusion network (EDN).
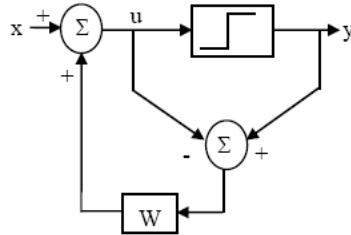
Figure 3. Block diagram of an error diffusion architecture.

In equilibrium, the error diffusion neural network satisfies

$$u = W(y - u) + x \tag{1}$$

which results in an equivalence to a Hopfield network. Hopfield showed that when the matrix of interconnect weights W is symmetric with zero diagonal elements and the high-gain limit of the sigmoid $\Im[\cdot]$ is used, the stable states of the outputs are the local minima of an energy function. It can be shown that our network tends toward states near local minima of the energy function

$$\begin{aligned}
E(x, y) &= y^T A y - 2 y^T A x + x^T A x \\
&= \underbrace{(y - x)}_{error}^T A \underbrace{(y - x)}_{error} = e^T A e
\end{aligned} \text{, where } A = (I + W)^{-1} \tag{2}$$

51

The Fourier transform of this convolution yields a useful alternative form of Equation (2)

$$\tilde{E}(x,y) = \sum_{k=0}^{n-1} \left|\tilde{A}\right|_k (\tilde{y}_k - \tilde{x}_k)^2 = \sum_{k=0}^{n-1} \left|\tilde{A}\right|_k (\tilde{e}_k)^2 \qquad (3)$$

Equation (3) shows that EDNs offer a natural tool for digital halftoning subject to a frequency-weighted square error. Behavior of the network is determined by the $N \times N$ matrix of weights W, which filters the errors. Filtered errors are distributed to neuron inputs through a vector sum element which adds to the input gray image x.

An EDN for color halftoning has, in our case, three neurons per pixel, one for each primary color. We assume these to be red, green, and blue. Hence the color of an input pixel is completely described by a triple $<x_R, x_G, x_B> \in [0,1]^3$, and an output pixel by $<y_R, y_G, y_B> \in \{0,1\}^3$. Output pixels therefore have one of eight possible colors including black and white. Figure 4 illustrates our three-dimensional error diffusion scheme. The arrows indicate the directions in which error diffuses. We choose 7×7 matrices as the error diffusion weights, W. Consider a green pixel in the center of a 7×7 color pixel array. The quantization error from the green pixel diffuses symmetrically in three dimensions as follows: The error is distributed by weights W_{GG} to its 48 neighbor green pixels; the error is also distributed to its 49 neighbors in the red plane by interconnect weights W_{GR} and to its 49 neighbors in the blue plane by interconnect weights W_{GB}. The same scenario applies to red and blue pixels.
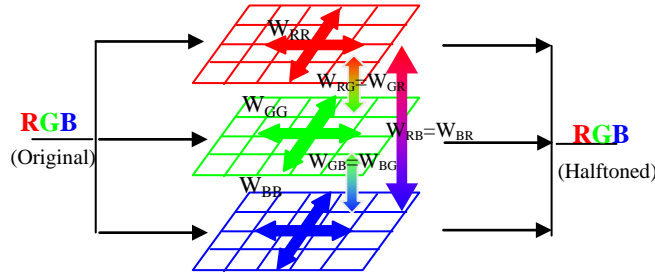
Figure 4. Three-dimensional error diffusion network.

The in-plane error diffusion weights, W_{RR}, W_{GG} and W_{BB}, can each be taken as the ones we previously found in monochromic halftoning,

$$W_{RR} = W_{GG} = R_{BB} = \begin{bmatrix} 0.0005 & 0.0020 & 0.0052 & 0.0069 & 0.0052 & 0.0020 & 0.0005 \\ 0.0020 & 0.0104 & 0.0249 & 0.0329 & 0.0249 & 0.0104 & 0.0020 \\ 0.0052 & 0.0249 & 0.0584 & 0.0767 & 0.0584 & 0.0249 & 0.0052 \\ 0.0069 & 0.0329 & 0.0767 & 0 & 0.0767 & 0.0329 & 0.0069 \\ 0.0052 & 0.0249 & 0.0584 & 0.0767 & 0.0584 & 0.0249 & 0.0052 \\ 0.0020 & 0.0104 & 0.0249 & 0.0329 & 0.0249 & 0.0104 & 0.0020 \\ 0.0005 & 0.0020 & 0.0052 & 0.0069 & 0.0052 & 0.0020 & 0.0005 \end{bmatrix} \qquad (4)$$

The sum of the weights is unity so that the error is preserved and not amplified or reduced and the total intensity is kept the same for each primary color. The cross-plane weights, W_{RG}, W_{RB} and W_{GB}, the 3rd error diffusion dimension, must maintain the advantage of being nondirectional

and symmetric. The sum of the weights must be zero so that there is no net transfer of color from one primary to the others. Such filters are constructed based on minimizing the luminosity error.

We have developed an EDN with a three-dimensional interconnection scheme that can coordinate the red, green, and blue halftoning solutions so that luminosity error is shaped concurrently with the error in each of the primaries, with user-adjustable emphasis on the relative importance of weighted error in luminosity. The result is shown in Figure 5(c) where the enlarged halftone pattern has smoother color transitions and less contrast compared to Figure 5(b), especial the gray scale images that represent the luminance information. As a result, the visibility of the halftone texture, which consists of pixels with high contrast, is minimized. Thus the overall image appears to have a more homogeneous tone.
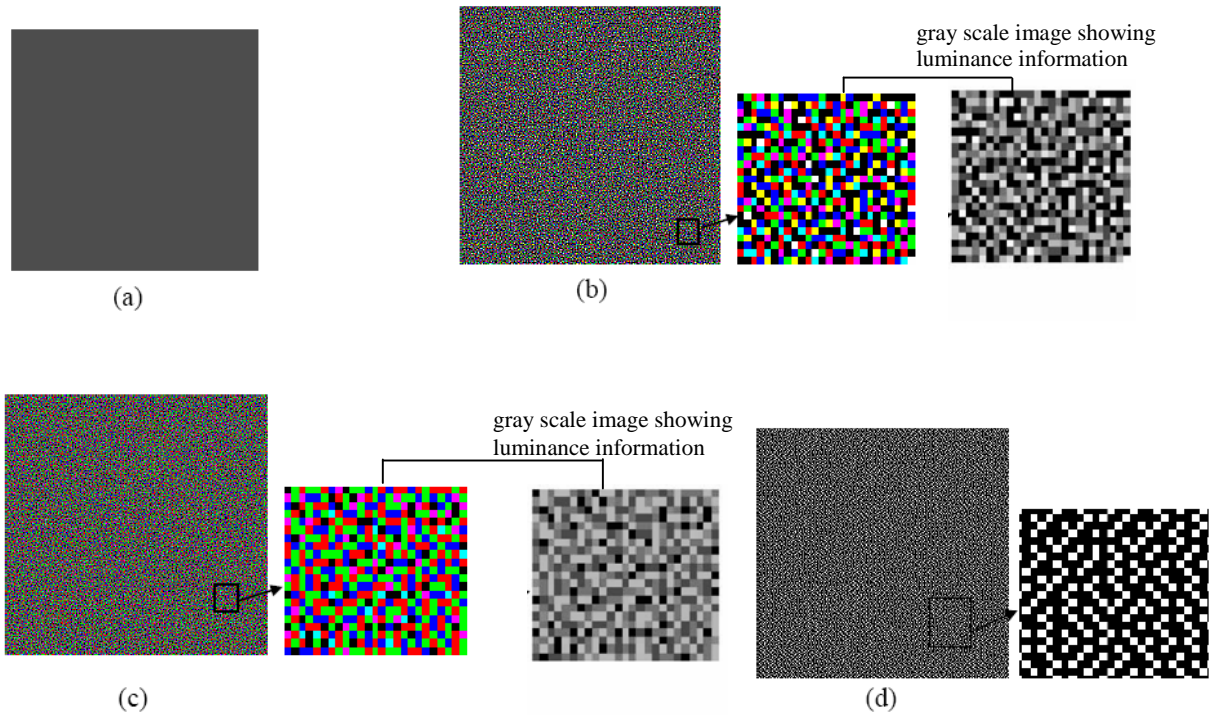
Figure 5. A gray scale image and its halftone results. (a) The original 30% gray scale continuous tone image; (b) Halftone image generated from two-dimensional gray scale EDN independently on each color plane; (c) Halftone image generated from the 3-D interconnect weights when $\rho_R = 2.0$; (d) Halftone image generated from Floyd-Steinberg's filter.

The correlation among the primary planes in the 3D EDN reduces the overall visibility of the halftone texture and results in a closer reproduction of the continuous tone image. The 3D EDN filter consequentially leads the halftoned solution to meet the minimum brightness variation criterion, which is known to be a measure of a good color halftoning algorithm.

Another recent result is a theorem showing that error minimization properties of the network are maintained when the real-valued vector of inputs is replaced with a tensor – each "pixel" itself consisting of a vector – and each "neuron" output is chosen from a fixed set of pattern vectors, the Euclidean-nearest to the neuron input.

An immediate implication of this theorem is a generalization of our color halftoning algorithm. This algorithm necessarily converts an RGB continuous input into an RGB output where each primary is either 1 or 0, for 8 possible colors in all (black, white, cyan, magenta, yellow, red, green, and blue). The theorem says that colors may be deleted from this set of admissible outputs (for example select black, white, red, green, and blue), and the algorithm will still choose an optimal output.

A more important implication is that our EDNs can be used as error-conserving multispectral classifiers. For this we choose the output pattern vectors to be the spectra of "materials" expected in the output. The classifier will initially choose the Euclidean-nearest pattern for each pixel, and then gradually converge to a solution that globally incorporates error of these choices diffused across the output image according to any of a broad class of weighting schemes. The most logical method of choosing weights is to deconvolve likely diffraction errors in the imaging device that produced the inputs. Experiments to test this implication of the new theory are in progress.

While the primary emphasis of our work to date has assumed a specialized hardware (photonic or VLSI) implementation of the EDN algorithm, the algorithms we have designed to simulate this hardware, evolved over a period of years, has recently shown to be almost perfectly adapted to massively parallel implementation on Graphical Processing Units (GPUs). Early tests using the Nvidia Fermi GPU technology indicate the capability of color-halftoning a full page at 1200 dpi laser printer resolution in less than 10 seconds. Since our algorithm compares favorably in a well-regarded suite of standard tests with the best-quality algorithms in literature, we are finding that Moore's Law has promoted our approach from the category of highly specialized to the mainstream, with commercial potential.

Discussion: Applications to Raman Spectroscopy for Trace Explosive Detection
Wide-field Raman chemical imaging (RCI) has been shown to be a promising technique for detection and identification of the presence of trace explosives in contaminated fingerprints. Raman spectroscopy is a particularly appealing technique for detecting explosives on surfaces because it is typically non-destructive and requires no sample preparation. The former trait is important in forensic applications as it leaves the sample intact for further analysis. Additionally, the spectral features associated with Raman scattered light are generally very sharp allowing for the detection and analysis of complex mixtures. RCI provides an additional level of discrimination due to the fact that many components are spatially separated in a heterogeneous sample.

This project is a collaboration with the U.S. Army Edgewood Chemical Biological Center. In this work, fingers were contaminated with explosives by pressing against a small sample of powder and removing the excess by scrubbing the thumb across the surface of the contaminated finger. The contaminated finger was then pressed on a clean surface, leaving a fingerprint. Figure 6 shows an example of this process.

Figure 6 (A) Finger after pressing into sample (not used for analysis) (B) Finger in Frame A after scrubbing bulk residual and used to produce fingerprint in Frame C (C) Fingerprint on a surface ready for analysis.

Here the fingerprint serves as the object sample and the process of collecting the Raman spectra is described in Figure 7.
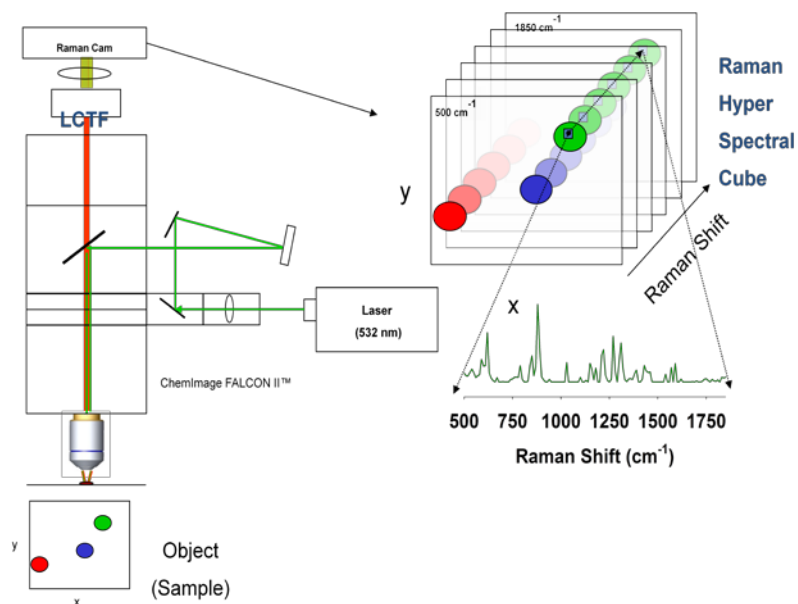
Figure 7. Collection of Raman chemical imaging (RCI) spectra from sample object (fingerprint).

The library spectra used for cross-correlation analysis and ultimately trace element identification included energetics like $NaNO_3$, RDX, PETN, and HMX, interferants like caffeine, aspirin finger skin and finger oil, and the scattering surfaces such as Teflon, polystyrene and polycarbonate. The Raman spectra used in this cross-correlation analysis are shown in Figures 8, 9, and 10.
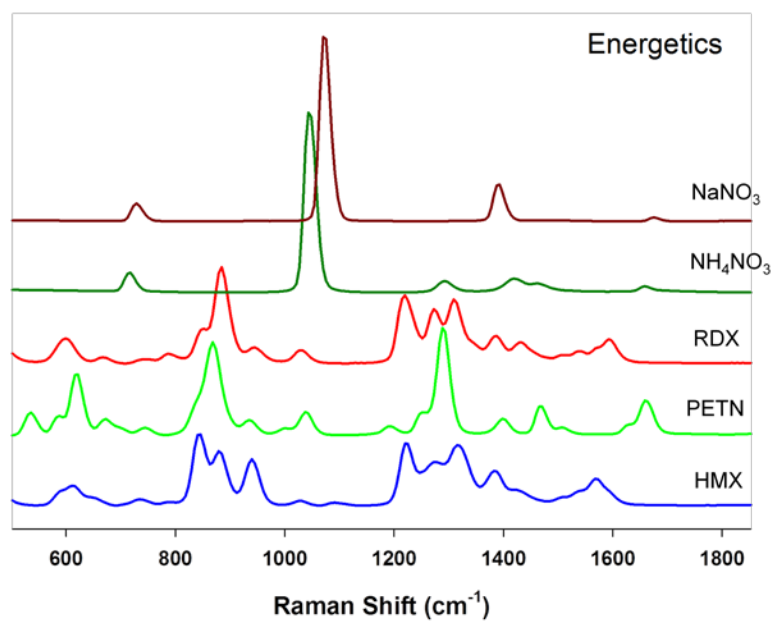
Figure 8. Raman spectra of typical energetics.
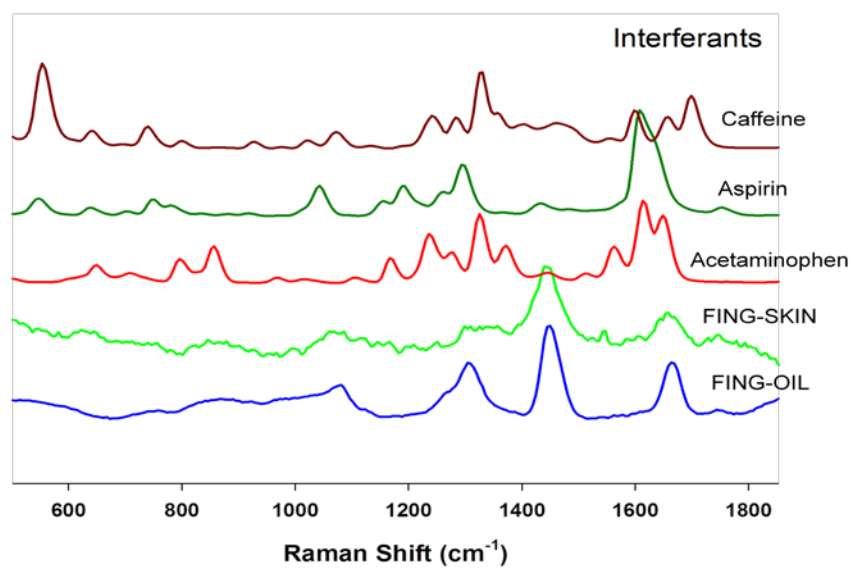
Figure 9. Raman spectra of typical interferants.
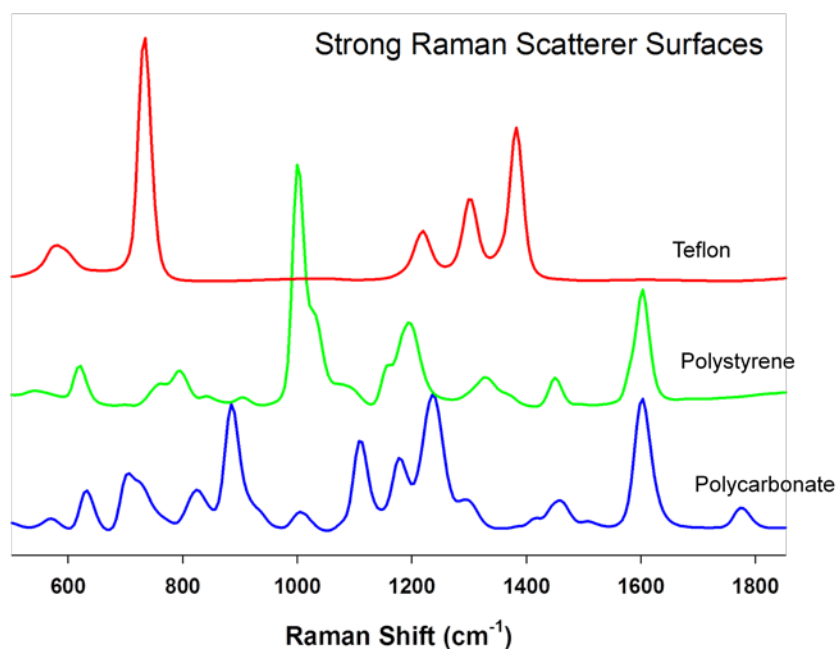
Figure 10. Raman spectra of typical scatterer surfaces.

A Falcon II wide-field Raman chemical imaging microscope was used for the acquisition of Raman data. Excitation of the Raman scattering was performed with a 532 nm Coherent Verdi V-2 laser. This system uses the wide-field imaging method in which a laser spot completely envelopes the field of view (FOV). To spectrally resolve the Raman scattered light, a liquid crystal tunable filter (LCTF) was used for imaging onto a CCD camera. The native spatial resolution of the Raman CCD camera is 512×512 pixels. Binning groups of 3×3 pixels produced an effective resolution of the Raman CCD camera of 170×170 binned pixel groups (BPG). The LCTF was sequentially tuned to allow Raman shifted scattered radiation from the 500 to 1850 cm^{-1} range in 10 cm^{-1} increments, with an LCTF full width at half height (FWHH) of 8 cm^{-1}. At each wavenumber shift an image was taken with the Raman CCD camera with 15 second integrated exposures and two co-added replicates, producing a Raman hyperspectral cube (RHSC). The RHSC comprises 136 image frames, with each image frame representing a Raman wavenumber shift. Each binned pixel group in the RHSC provided the Raman spectrum from that region of the field-of-view to which it was exposed.

In addition, a mercury lamp was used to excite the sample for fluorescence imaging. Excitation was at 365 nm, with the broadband fluorescence emission being detected from 400-720 nm. Microscope objectives with 5×, 10×, and 20× magnifications were used to obtain the Raman chemical images with laser spot diameters of approximately 650 μm, 325 μm, and 133 μm, respectively. The spatial resolution of the BPGs for these objectives were 3.4 μm × 3.4 μm, 1.7 μm × 1.7 μm, and 0.85 μm × 0.85 μm, respectively. Laser power densities varied in the range of 35-500 W/cm^2.

The process begins with a broadband filter image (BFI) of the fingerprint, proceeds to invert and binarize that original image and then rank pixel intensity. The artifacts of this process are shown in Figure 11.

(a)   (b)   (c)
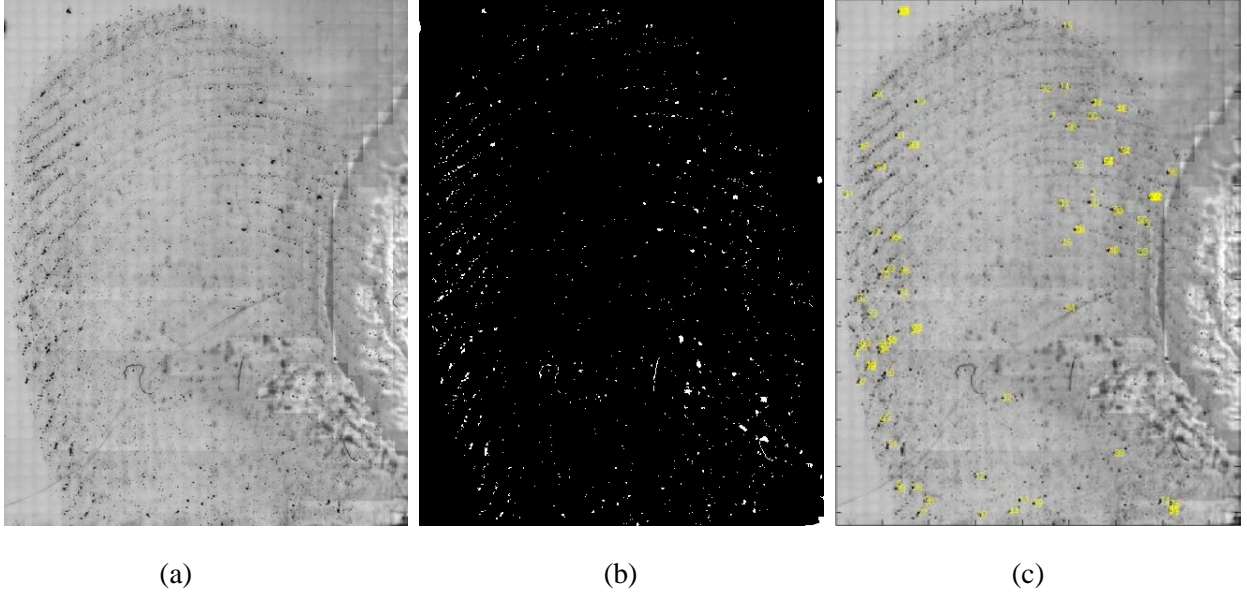
Figure 11. (a) BFI of fingerprint, (b) Inverted and binarized image, and (c) Ranked pixel intensity.

The application of our error diffusion neural network to this problem has taken two forms to-date. First, the binarization process used in the current approach is a simple thresholding of the original BFI image. Initial results show that the error diffusion algorithm provides a higher-quality binary image, retaining more of the original image information. An example of using the EDN to accomplish the binarization of the fingerprint image is shown in Figures 12 and 13.

(a)   (b)   (c)
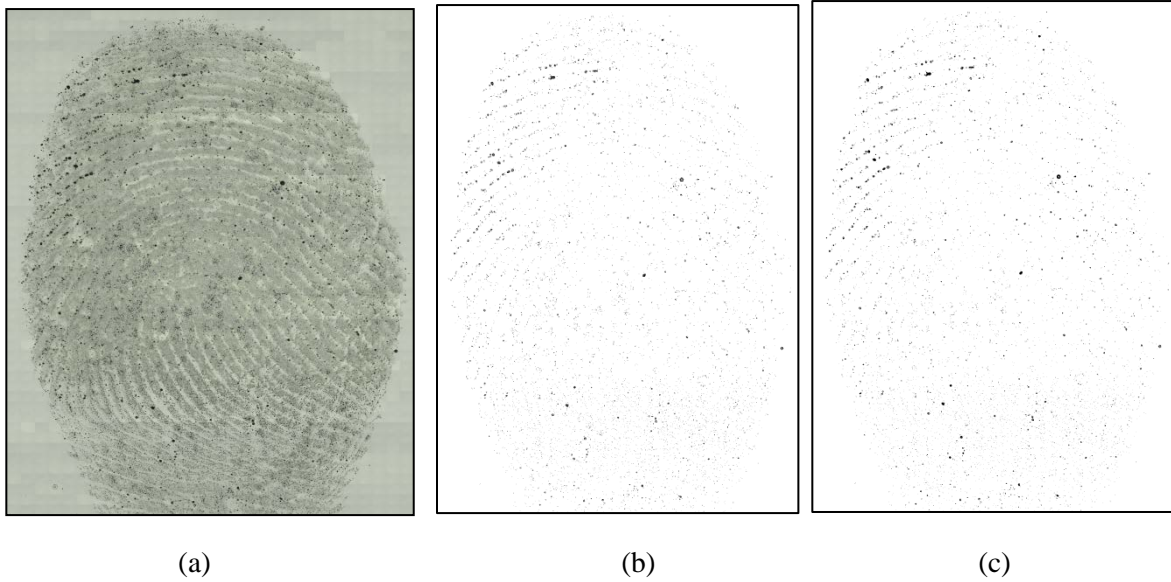
Figure 12. Binarization of the fingerprint image using the EDN (a) original fingerprint image, (b) halftoned image after 3 iterations using the EDN with a 21×21 bandpass filter with cutoff frequencies of 0.7 – 0.9 and a threshold of 0.45 and (c) halftoned image after 50 iterations.

(a)   (b)   (c)
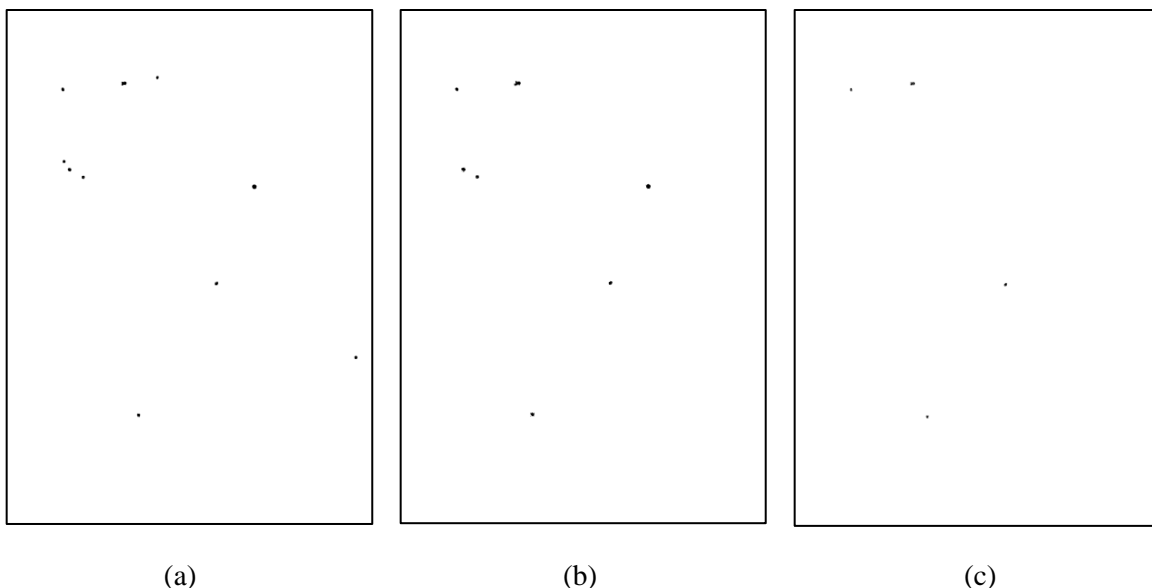
Figure 13. Further refinement of the halftone keeping only the highest intensity clusters which corresponds to the highest probability locations to investigate, (a) - (c) show increasing restrictiveness on the cluster intensity and therefore the targets with the highest probability locations for spectral analysis.

Additionally, by applying the EDN in the form of a multidimensional algorithm, similar to what we have previously done for color halftoning, we can accomplish target recognition in the image when viewed from the perspective of trace element identification. By coding the Raman spectra of the target energetic into the weighting of our neural algorithm we allow the network to process the image, minimizing the error across multiple special planes and providing visual target identification. This work is in progress.

Future Direction
Extensions of this work include multidimensional applications of the EDN to target identification and target recognition including the trace explosive detection effort and other sensing and imaging applications.

Faculty Involvement
Barry L. Shoop, Eugene K. Ressler, Wenli Huang, Jean R. S. Blair, Robert W. Sadowski, Andre H. Sayles, George Nowak, Glen P. Dudevoir, Gregory R. Kilby, James J. Raftery, Jr., Edward C. Shaffer, Guy M. Burrow, Bryan G. Goda, Dirk A. Hall, Thomas D. Wagner, David A. Nash, Brian Gollsneider, Thomas R. Moore, Anthony J. Megofna, Timothy J. Talty, James R. Loy, Gregory B. Tait, Diana Thomas, Daniel M. Litysnki, Bradford C. Tousley.

Cadet Involvement
Mark Buck, Daaron Spears, R. Lynch, B. Bailey, J. deLottinville, D. Downs, Zachariah G. Morford, Michael J. Sullivan, Jr., Jason H. Cuneo, Scott A. Bradley, Kirk A. Ingold, Brian J. Smith, John Kettula, Jordan J. Fisher.

Publications

1. B. L. Shoop and K. B. Robinson, "ABET accreditation and optics and photonics engineering: An association whose time has come," *Invited Paper*, SPIE Optics Education Conference, 2012 SPIE Optics + Photonics Conference (San Diego, CA), August 2012.

2. B. L. Shoop and E. K. Ressler, "Developing the critical thinking, creativity and innovation skills of undergraduate engineering students," International Journal of Engineering Education, Vol. 27, No. 5, pp. 1072-1080, 2011.

3. B. L. Shoop, "Photonics for analog-to-digital conversion," *Jack S. Kilby Lecture*, 34th Annual Government Microcircuit Applications and Critical Technology Conference (Reno, Nevada), March 2010.

4. W. Huang, E. K. Ressler and B. L. Shoop, "Minimization of color halftone texture visibility using three-dimensional error diffusion neural network," Proc. of the 21st Annual IS&T/SPIE Symposium on Electronic Imaging, San Jose Convention Center, San Jose, CA, Jan 18-22, 2009.

5. W. Huang, E. K. Ressler and B. L. Shoop, "A Three-Dimensional Interconnect Scheme for Color Error Diffusion," J. of Electronic Imaging, vol. 17, issue 2, April 2008.

6. W. Huang, E. K. Ressler and B. L. Shoop, "Error Diffusion for Color Halftoning Using Three-Dimensional Neural Interconnects", Proceedings in The 3rd International IEEE EMBS Conference on Neural Engineering, pp. 553-556, Kohala Coast, HI, 2-5 May 2007.

7. E. K. Ressler, W. Huang, B. L. Shoop, "Three-Dimensional Error Diffusion For Color Halftoning," Conference presentation in Frontiers in Optics 2006 OSA Annual Meeting, Rochester, NY, 8-12 Oct 2006.

8. W. Huang, B. L. Shoop, E. K. Ressler, C. Bonamigo, A. Garcia, "Application specific multispectral imaging processing using a novel halftoning algorithm," FIO the 89th OSA Annual Meeting, Laser Science XXI, Tucson, AZ, 16-20 Oct 2005.

9. J. J. Liu, B. R. Gollsneider, W. Chang, "Two-Dimensional Opto-Electronic Interconnect-Processor and Its Operational Bit-Error-Rate", in Proceedings of Optics East Conference, (Philadelphia, Pennsylvania), October 2004.

10. J. R. S. Blair, T. D. Wagner, D. A. Nash, E. K. Ressler, B. L. Shoop, and T. J. Talty, "Partitioning schemes for use in a neural network for digital image halftoning," Proceedings of the SPIE, vol. 4055, pp. 36-48, April 2000.

11. B. L. Shoop, P. K. Das, and E. K. Ressler, "A novel approach to photonic A/D conversion based on a fully-connected, distributed mesh feedback architecture," Proceedings of the SPIE, vol. 4089, pp. 333-344, June 2000.

12. B. L. Shoop, P. K. Das, E. K. Ressler, and T, J. Talty, "High-resolution photonic A/D conversion using oversampling techniques," in Proceedings of Conference on Lasers and Electro-Optics, (San Francisco, California), May 2000.

13. E. K. Ressler and B. L. Shoop, "High quality digital halftones from error diffusion networks," Proc. of the Society for Information Display, (San Diego, California) 506-509 (1996).

14. B. L. Shoop and E.K. Ressler, "An error diffusion neural network for digital image halftoning," Proc. of the IEEE Workshop on Neural Networks, 427-436 (1995).

Acknowledgements

Pan-Species Chemical Agent Detection via Opto-Mechanical Surface Acoustic Waves

CPT John Zehnpfennig, CDT Matthew Letarte, CDT David Covell

Photonics Research Center
Department of Electrical Engineering and Computer Science
United States Military Academy, West Point, New York 10996
E-mail: john.zehnfpennig@usma.edu

Abstract.   Here we exploit the ultra-high optical quality factor of silica whispering gallery resonators to generate mechanical surface acoustic waves via the strong photon-phonon interplay leading to Brillouin scattering and interaction between the resultant Stokes optical line with the original pump line.   The surface acoustic waves thus generated likewise enjoy a very high mechanical quality factor on the order of tens of thousands, leading to strong resonance and displacement of the resonator's surface.   The speed of these surface waves, at a given wavelength, varies with the speed of sound of the material surrounding the silica resonator.   Detecting the frequency of the surface wave, we are able to observe, quantify, and identify material changes in the environment surrounding the resonator via frequency shift.

Background

The Army – and the world – presently use outdated chemical agent detection methodologies related to detecting specific species of categories of chemical agent weaponry in the ambient environment surrounding forces or populations. Although work has been done in the various sectors of research, commercially available chemical detection devices are rarely much more than fancy "litmus paper" implementations – good to say that "the air has changed" yet riddled with uncertainty.   Every private Soldier in the US Army undergoes chemical agent training wherein they are shown that common dish detergent registers as "nerve agent" in the various field detection equipment.

We suggest the use of opto-mechanically energized surface acoustic waves upon tens-of-micron scaled silica whispering gallery resonators. A whispering gallery resonator was first reported [1] by Lord Rayleigh in St. Paul's Cathedral, but was well known and employed prior by architects and masons. A whispering gallery is a circular structure that is exactly an integer number of wavelengths in circumference. In this geometry, a resonant frequency constructively interferes with itself a finite number of times, related to the quality factor of a wave of that type – photonic, phononic, or electronic – within the resonant cavity. In the case of St. Peter's, whispers (phonons) around 1500Hz were amplified in this manner. Naturally, any number of frequencies may be resonated by the same resonator as long as the following equation holds:

$$M = \frac{C}{\lambda} \ \ where \ M \epsilon \mathbb{Z}$$
<div align="right">Eq. 1</div>

M is the mode number or number of times a traveling wave oscillates in one full trip around the circumference. M must be an integer for maximum resonance, but M values close to an integer will also resonate weakly. C is the circumference of the circular resonator and λ is the center wavelength of the wave.

The maximum oscillation amplitude is related to the average number of round-trips that a single photon or phonon takes within the resonator – prior to scattering out or being absorbed by the

material. This number of round trips is quantified in the dimensionless value known as quality factor, Q. The optical quality factor of homogeneous fused silica with optimal coupling in on the order of $Q_{opt} \approx 5 \times 10^8$. Given optimal coupling and homogeneous silica, we can excite a phononic, or mechanical, mode with a mechanical quality factor on the order of 10^4, which is a tremendous improvement over electro-mechanical systems.[2]

Figure 1 illustrates the method for excitation and the deformation profile of one such opto-mechanically generated surface acoustic wave. Excitation is carried out via evanescent coupling, here from a tapered fiber, into a whispering gallery resonator, here a sphere. The resonator is mounted on a stem of the same material as the resonator, here pictured as a cone.
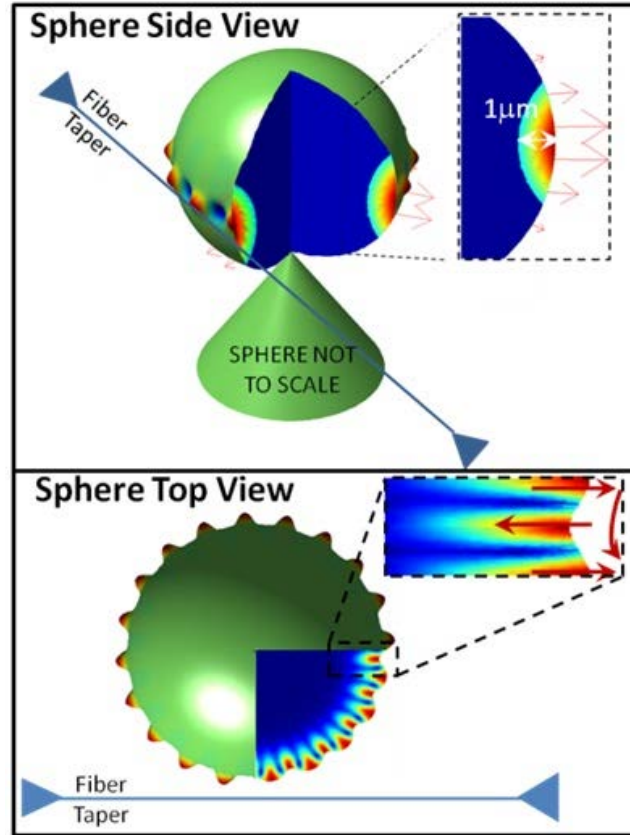
Figure 1. Illustration of the mechanical whispering gallery resonance in a sphere. Deformation of the outer surface describes the exaggerated mechanical deformation. The cuts reveal also the internal deformation as indicated by colors.

Theory
This ultra-high mechanical Q factor results in a large amplitude deformation on the surface of the resonator. This deformation is a periodic, moving train of virtual electrodes – meaning areas of high and low concentration of material, separated periodically on a distance of some wavelength, Λ_{SAW}, which is calculated using the conservation of momentum vectors:

$$K_{SAW} = k_p - k_S \hspace{3cm} \text{Eq. 2}$$

K_{SAW} is the momentum vector of the surface acoustic wave (SAW), measured in units $\left[\frac{1}{m}\right]$. k_p and k_S are the momentum vectors of the optical pump and Stokes lines, respectively. Given that

k is the inverse of wavelength, we are able to derive the relationship between the acoustical wavelength of the SAW, Λ_{SAW}, and the pump and Stokes optical wavelengths:

$$\Lambda_{SAW} = \frac{\lambda_p \lambda_S}{\lambda_S - \lambda_p} \qquad \text{Eq. 3}$$

Figure 2 illustrates the optical and mechanical modes as they are generated and interact.
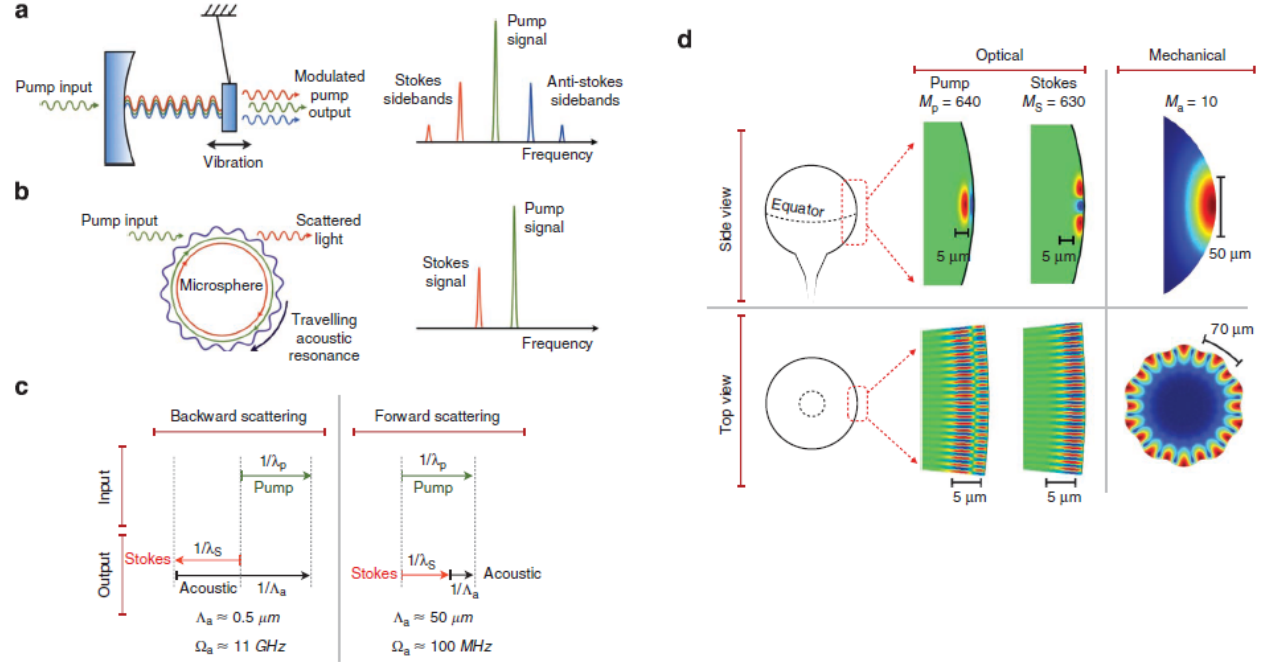
Figure 2.[3] Illustration for distinguishing stimulated cavity-optomechanics from parametric cavity-optomechanics. (**a**) In parametric excitation when one feeds the cavity with the laser right at the optical resonance, the pump is modulated due to a shifting optical resonance, resulting in two optical side bands accompanied by higher harmonics. If the laser is detuned, one can obtain asymmetric spectra to allow net energy transfer from light to the mechanical mode or vice versa. (**b**) In stimulated optomechanics (this work), the pump is scattered to only one Stokes sideband since the acoustic wave acts as a grating continuously moving away from the pump. (**c**) Wave vector conservation in forward Brillouin scattering leads to a much lower acoustic frequency regime when compared with backward Brillouin scattering. (**d**) Numerically solved optical and mechanical modes for phase-matched stimulated optomechanical interaction on a microsphere resonator, where colors represent electric field of the optical mode and the deformation of the mechanical mode. The mechanical mode (bottom-right) is a Rayleigh-type surface acoustic wave with experimentally observed frequency 57.8 M Hz.

This resonant mechanical wavelength, once established, holds steady in length and amplitude as long as the optical pump (wavelength, phase, and power) and coupling distance remain constant. The frequency of this mechanical surface wave is

$$\upsilon_{SAW} = \frac{v_{sound}}{\Lambda_{SAW}} \qquad \text{Eq. 4}$$

where υ_{SAW} is the mechanical frequency, v_{sound} is the velocity of sound at the interface (resonator-environment), and the SAW wavelength. Because our wavelength must remain constant in order to conserve momentum, observed υ_{SAW} shifts in a resonator of constant pump and coupling characteristics can only be explained by a change in the v_{sound} at the resonator-environment boundary.

Sound velocity is constant in homogeneous materials, or in a resonator that is para-homogeneous. Para-homogeneous is the apparent homogeneity of the materials over a path. If a photon's path about the resonator does not vary each round trip, any material inconsistencies are traversed in each round trip, the net effect being that the overall trip time, thus velocity, does not change over many cycles through the resonator. This net effect on velocity is important when considering the v_{sound} on the surface of an unchanging resonator but within a changing environment – air.
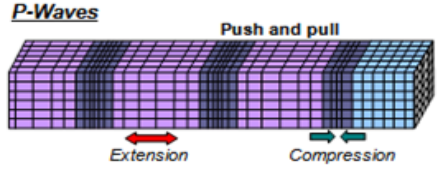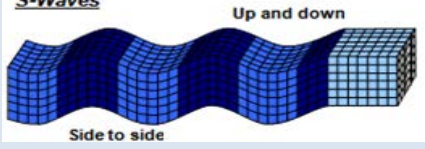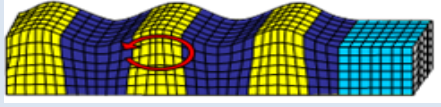
Over time, given the same wave and on the same resonator in 'air', the v_{sound} will experience slight fluctuations as environmental conditions change – concentration of chemicals in the 'air,' pressure, or temperature of 'air' may cause shifts of v_{sound}. This phenomenon is rooted in the fact that v_{sound} is dependent upon the density of the material through which the sound phonons propagate.

Therefore, where acoustic wavelength is a function of pump and coupling only, the frequency of the SAW is dependent upon both the acoustic wavelength and the density of the material(s) in which it is resonating. We suggest a relationship of

$$v_{sound} = v_{SAW} = \alpha v_{s,bulk} + \beta v_{s,fluid} \qquad [4\text{-}6] \qquad \text{Eq. 5}$$

where $v_{s,bulk}$ is the velocity of sound of a surface acoustic wave of a known family at the bulk (resonator) material interface at the bulk-air boundary and $v_{s,fluid}$ is the velocity of sound purely in the fluidic material surrounding the resonator.   Table 1 gives the analytical general solutions and deformation profile of the three most prominently observed SAW families on silica WGRs:

Table 1. Analytic solutions [7-10] and deformation profiles of most prominently observed SAW on silica WGR. Values for velocity are for surface waves on purely planar interface between silica and air.

Analytic Solution on Bulk SiO_2		
Wave	**Velocity [m/s]**	**Deformation**
Longitudinal	$V_L = \left(\dfrac{E(v-1)}{\rho(2v^2+v-1)} \right)^{1/2}$ $= 5972$	
Transverse	$V_T = \left(\dfrac{E}{2\rho(v+1)} \right)^{1/2} = 3766$	
Rayleigh	$V_R = \dfrac{V_T(0.87+1.12v)}{(1+v)} = 3413$	

Given Eq.5, we expect to see a shift of v_{SAW} when we introduce pollutants into the environment surrounding a resonating WGR as the change in fluidic properties (density, etc.) will result in a differing $v_{s,fluid}$.

Results

We have shown theoretical, numerical, and empirical results related to opto-mechanics of a surface acoustic wave. Figure 3 illustrates the culmination of our analytical study into surface acoustic wave generation via finite element method calculations. The method for generating these calculations in the FEM package COMSOL [11] is found in our work at [12, 13]. Figure 3 shows solutions to each of the waveforms proposed in Table 1. We find that each waveform 'family' is capable of producing surface with maxima in both the azimuthal and transverse (radial, polar) directions.
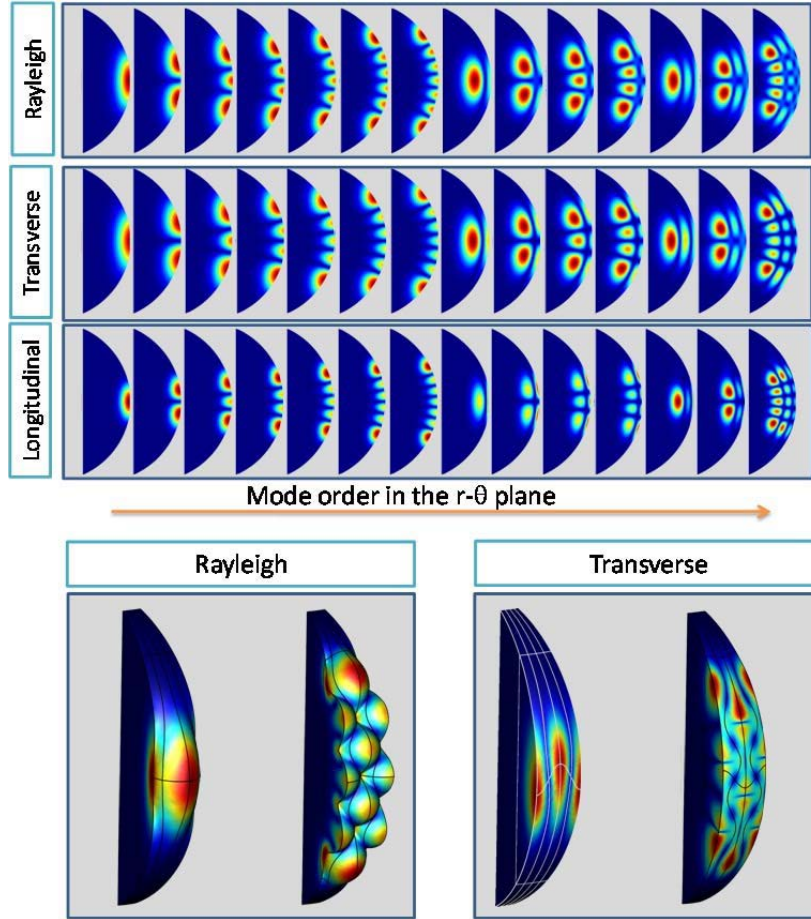
Figure 3. [14, 15] High-order mechanical whispering gallery modes. Top: Increasing the mode order in the radial and polar directions for mechanical whispering galleries in a silica sphere. Color stands for deformation; the sphere circumference is 20 in units of wavelength. Below: We depicted several of the top modes and present them in 3D. The presented section is one wavelength in the azimuthal direction. The equator is seen to deform into a sine while for the Rayleigh mode, the sine deformation is in the radial direction and for the transverse mode the sine deformation is in the polar direction.

Our initial results showed that SAW on silica WGR can have stable frequencies for lengthy periods of time. Figure 4 shows a single stable 150MHz line on a spherical micro-resonator of 120micron radius:
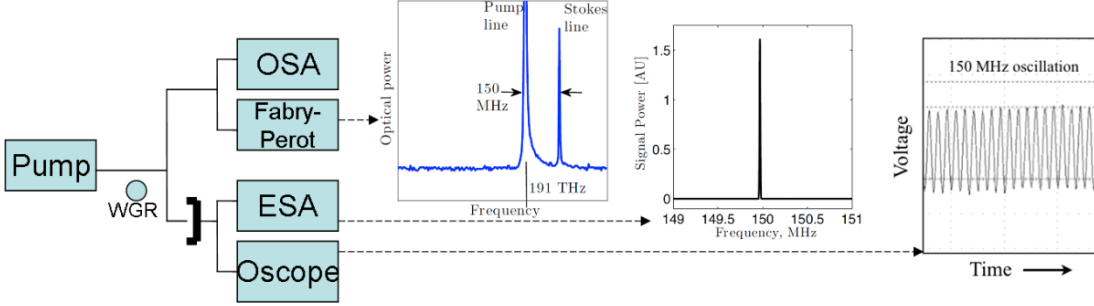
Figure 4. [16] (From left) Experimental setup showing pump laser exciting mechanical resonances in the WG resonator (WGR). Forward Brillouin scattered Stokes lines are detected optically and electronically. The Optical spectrum analyzer (OSA) and Fabry-Perot interferometer (left inset) show a pure 150MHz tone with no extraneous resonances. The electric spectrum analyzer (ESA, middle inset) shows the 150MHz resonance in frequency domain to have an extremely high SNR as well as be a pure tone. The oscilloscope (right inset) shows the time-domain 150MHz oscillations of the resonance.

We have shown that a single microresonator is capable of providing many different mechanical resonant frequencies, simply by changing the input optical pump wavelength. Figure 5 shows the various resonances of a single microresonator of radius 108 microns. We achieved this spectrum by scanning the pump laser across its tuning range of approximately 60 nanometers in increments of 100pm every 200ms. These modes are detected using the ESA in the setup described by Figure 4, which is designed to capture forward-scattered SAW via stimulated Brillouin scattering, hitherto considered impossible [17].
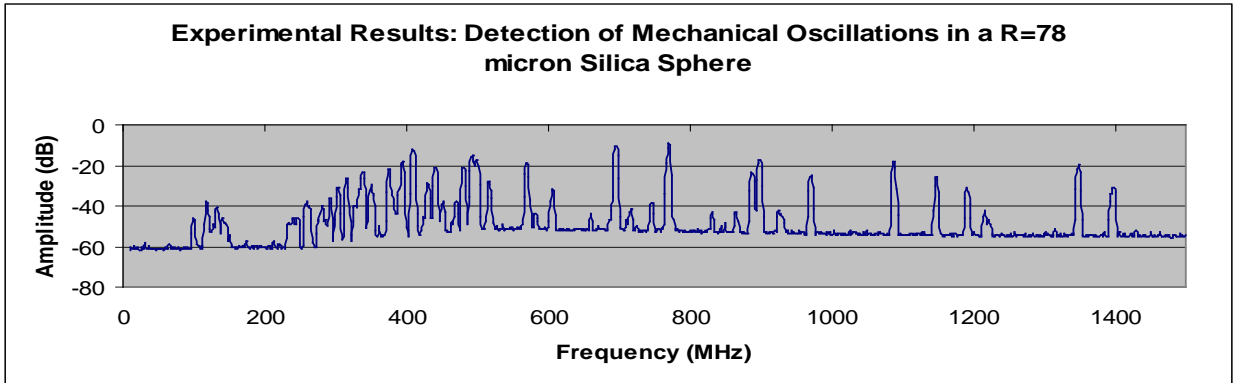
Figure 5. Experimental data showing the various resonances within a single microresonator of radius 78 microns. Each peak represents an individual resonance, and each resonance occurs alone and independent of other mechanical resonances. We used the 'max hold' feature of our ESA to display and store all resonances.

Naturally, we wonder what applications may benefit from our device and methods. Several come immediately to mind: local oscillation, particle detection, and chemical detection.

Local oscillation for the purposes of measuring time is possible, but our research into the phase noise of these surface acoustic waves finds that within the constraints of our lab, the phase noise is unacceptable for sensitive time applications. Research continues by DARPA ORCHID and others to devise methods of bringing this phase noise down, as the tunability of a cheap microsphere at GHz range is desirous.

Particle detection is possible with a surface wave as described here, but the surface wave is not an essential component. It has been shown that particles resting on the surface of a resonator

cause a mass increase, and thereby shift the optical Stokes line relative to the pump.[18] The use of surface waves to detect particles is currently under study.[19]

We look to detect changes in the chemical composition of the air via a change in density. We have long proposed that the speed of the surface wave varies based upon the composition of the fluidic environment surrounding the resonator, as the velocity of the surface wave should be a weighted average between the speed of sound of a surface wave on the purely planar material and the velocity of sound in the fluidic material. Equation 5 is the most generalized format of this prediction. As noted, wavelength must remain fixed in order to conserve momentum, thus changes in the velocity of the SAW must be related to a change in SAW frequency.

Recently, we showed that the α likely equals $\alpha = 1 + \sin\left(\frac{\Lambda_{SAW}}{r_{WGR}}\right)$ and β likely equals $\sin\left(\frac{\Lambda_{SAW}}{r_{WGR}}\right)$ where r_{WGR} is the radius of the whispering gallery resonator. Figure 6 shows our match between FEM, Equation 5 with the above substitutions for α and β.
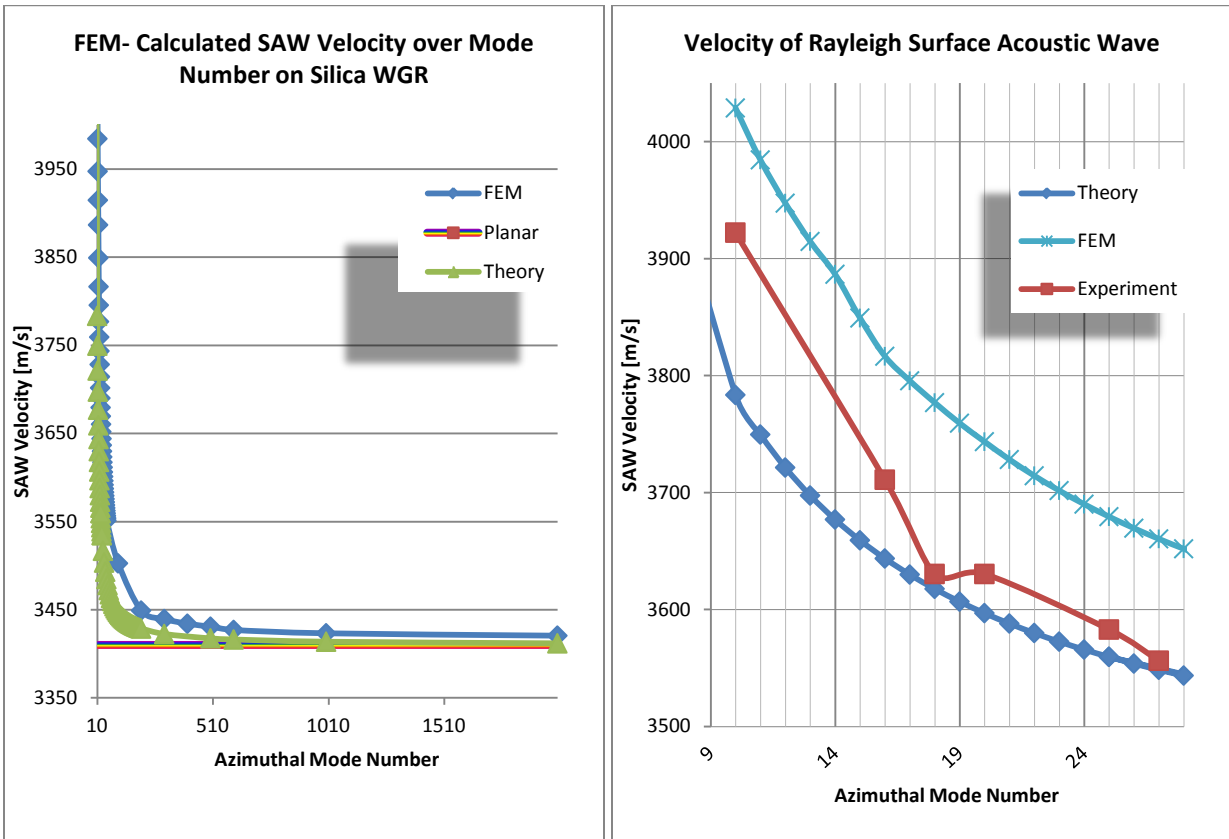
Figure 6. [5] These charts depict the velocity of a Rayleigh-type surface acoustic wave on silica in air. LEFT: Eqn 5 (Theory) versus FEM calculated surface acoustic wave velocity. The Planar line is the speed of a Rayleigh wave on planar silica, as calculated in Table 1. RIGHT: a zoom-in of azimuthal modes 9-28 with experimental results added for comparison. Note that although there is a large error between Eqn 5 and the FEM, the error between the FEM and experiment is consistently higher than the error between Eqn. 5 and experiment.

We conducted a parametric study in a FEM software comparing the speed of SAW on a silica sphere in an environment of air plus varying concentrations of carbon dioxide. Our data in Figure 7 supports Equation 5 from 0% carbon dioxide to 50%, and then contradicts the prediction up to 100% carbon dioxide. We are looking in to what caused this error and build a

better FEM calculation model. We are working in the lab to experimentally validate both Eqn. 5 and the results of Figures 6 and 7.
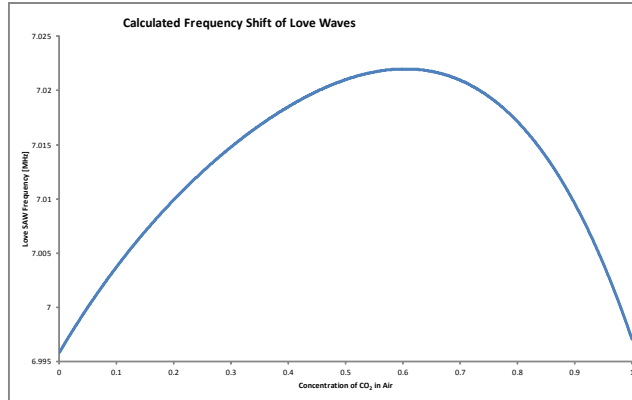
Figure 7. [6] FEM calculations of expected frequency shift of a Love-type surface acoustic wave on a silica microresonator.

Future Direction

Our present concern is to fully simulate and empirically verify the phenomenon reported here. We intend to have a functioning chemical sensor by mid-winter 2012-13. Our University of Michigan collaborators have reported a functioning sensor functioning on liquids flowing through a micron-scaled capillary; our device will be superior in that it does not require a flow mechanism other than what is passively available in the ambient environment.
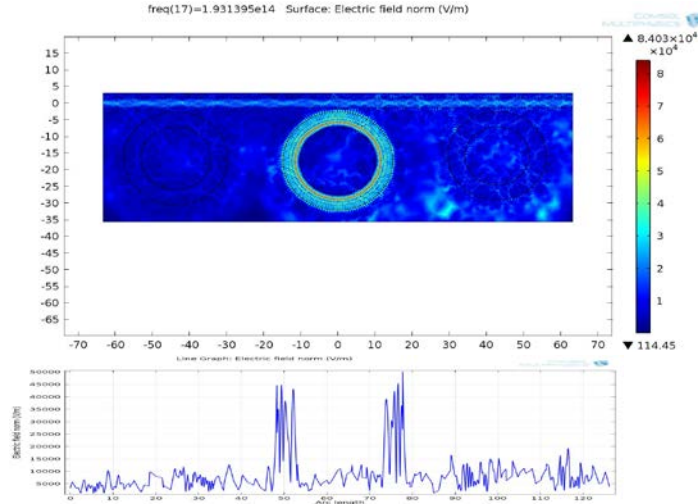
Figure 8. FEM simulations of all-optical de-multiplexing. The waveguide (top image) is pumped with one to three optical signals, each separated by 10nm. Here, we are pumping with 1.55micron light; the middle ring is strongly resonant (lit) while the other two rings reject the signal (dark). The chart below shows electric field, taken across the center of all three rings.

Additionally, we have commenced a separate WGR study wherein we are working towards a high-speed all-optical (de)multiplexing, switching, and binary/analog logic functions. Our group is actively pursuing high-speed de-multiplexing in collaboration with Professor Keren Bergman's group at Columbia University. Our stated goal is to have a 4x4 mux/demux device

operating at 40Gb/s with an FSR of 10 nanometers. Our initial simulations results, featured in Figure 8, are promising.

Future advances in WGRs may lead to compact, all-encompassing digital routers with sensors or labs on chip. Exploiting the local oscillation capabilities of a single mode-locked WGR for timing and using separate filtering WGRs to switch, multiplex, de-multiplex, and carry out logic we have an ideal ultrafast switch, bridge, and router.

In the same device, we can integrate WGRs dedicated to sensing. We can use several sensor WGRs to report chemical, particulate, and meteorological data – this data can be fed directly into the multiplexed stream on a separate channel.

Conclusion

The study and use of surface acoustic waves on microresonators is a vibrant field of research, and may lead to advances in local oscillation and chemical/particle detection. Further, WGRs may be exploited to benefit ultra-high-speed data operations – filtering, switching, and logic. All of our work is at the state of their various arts, as demonstrated by our consistent selection to present our work at a variety of optics and physics conferences. We look forward to continuing in this vein and advancing the state of the arts to the benefit of the Army and our Nation.

Cadet and Faculty Involvement
COL James J. Raftery, Jr. (EE&CS and PRC)
COL Robert W. Sadowski (EE&CS)
LTC Kraig E. Sheetz (P&NE)
MAJ Matthew Rapp (EE&CS)
CPT John Zehnpfennig (EE&CS and PRC)
CDT Matthew Letarte '13 (C&LS)
CDT David Covell '13 (EE&CS)
CDT Rachel Pauley '13 (EE&CS)
CDT Justin Hyder '13 (EE&CS)
CDT Zachary Newman '14 (EE&CS)

Publications
1. John Zehnpfennig "Calculating and Observing Opto-Mechanically Induced Surface Acoustic Waves in Silica Whispering Gallery Microresonator" *Proceedings CD of COMSOL Boston 2011.* Moderator: Vladimir Leonov, available at www.comsol.com (13 Oct 2011) 6.

2. G. Bahl, J. Zehnpfennig, M. Tomes, and T. Carmon "Stimulated optomechanical excitation of surface acoustic waves in a microdevice" *Nature Communications.* Vol. 2, Article 403, DOI: 0.1038/ncomms1412 (26 Jul 2011) 6.

3. J. Zehnpfennig, G. Bahl, M. Tomes, and T. Carmon "Surface optomechanics calculatingoptically excited acoustical whispering gallery modes in microspheres" *Optics Express.* Vol. 19, Issue 15, pp. 1424014248, doi:10.1364/OE.19.014240 (11 Jul 2011) 9.

Technical Presentations

1. J. Zehnpfennig, D. Covell, M. Letarte, K. Sheetz, J.J. Raftery, "Surface Optomechanics: Analytic Solution of Detection Limits of Surface Acoustic Waves in Various Fluids" *Frontiers in Optics 2012*, Rochester, NY 14-18 Oct 2012, 2. (**Cadet Coauthorship)**

2. J. Zehnpfennig, G. Bahl, M. Tomes, T. Carmon "Surface Optomechanics: calculating surface acoustic wave generation on microsphere via photon-phonon interaction" *XIV International Conference on Phonon Scattering and Condensed Matter.* Ann Arbor, Michigan, 8-13 July 2012, 2.

3. J. Zehnpfennig, M. Letarte, R. W. Sadowski, J. J. Raftery, Jr. "Surface Optomechanics: Calculation of Love Surface Acoustic Waves on Microresonators" *Conference on Lasers and Electro Optics(CLEO) 2012.* San Jose, CA, 6-11 May 2012, 2. (**Cadet Coauthorship).**

4. J. Zehnpfennig "Calculating and Observing Opto-Mechanically Induced Surface Acoustic Waves in Silica Whispering Gallery Microresonator" *COMSOL Conference Boston 2011.* Boston, MA. October 23, 2011. 4.

5. J. Zehnpfennig, G. Bahl, M. Tomes, T. Carmon "Surface Optomechanics: Calculating Optically Excited Acoustical Whispering-Gallery Modes in Microspheres" *Frontiers in Optics/Laser Science (FIO/LS) 2011.* San Jose, CA. October 16-20, 2011. 4.

6. G. Bahl, J. Zehnpfennig, M. Tomes, and T. Carmon "Surface Optomechanics: Observation of Surface Acoustic Resonances in Whispering Gallery Resonators" *Quantum Electronics and Laser Science Conference (CLEOQELS) 2011.*Baltimore, MD. May 26, 2011. 2.

7. G. Bahl, J. Zehnpfennig, M. Tomes, and T. Carmon "Characterization of Surface Acoustic Wave Optomechanical Oscillators" *IEEE International Frequency Control Symposium 2011.* San Francisco, CA. May 15, 2011. 4.

8. J. Zehnpfennig, G. Bahl. M. Tomes, and T. Carmon "Surface Optomechanics: Observation of Surface Acoustic Resonances" *OSA Frontiers in Optics Conference 2010.* Rochester, NY. October 24-28,
2010. 1.

9. J. Zehnpfennig, M. Tomes, and T. Carmon "Surface Optomechanics: Mechanical Whispering-Gallery
Modes in Microspheres" *IEEE Optical MEMS and Nanophotonics Conference .* Sapparo, Japan. August 9-12, 2010. 2.

References
[1]   L. Rayleigh, "The problem of the whispering gallery," Philos. Mag, vol. 20, pp. 1001–1004, 1910.
[2]   D. K. Armani, T. J. Kippenberg, S. M. Spillane, and K. J. Vahala, "Ultrahigh-Q toroid microcavity on a chip," Nature, vol. 421, pp. 925-928, 2003.
[3]   G. Bahl, J. Zehnpfennig, M. Tomes, and T. Carmon, "Stimulated optomechanical excitation of surface acoustic waves in a microdevice," Nature Communications, vol. 2, p. 6, 26 July 2011 2011.
[4]   J. Zehnpfennig, "Surface Optomechanics: Forward and Backward Scattered Surface Acoustic Waves in Silica Microsphere," Masters of Science in Engineering (Electrical Engineering) Written in University of Michigan, Ann Arbor's Rackham Graduate School Doctoral Dissertation format, Electrical Engineering and Computer Science, University of Michigan, Ann Arbor, ProQUEST, 2011.
[5]   J. Zehnpfennig, M. Letarte, D. Covell, K. E. Sheetz, and J. J. Raftery Jr., "Surface Optomechanics: Analytic Solution of Detection Limits of Surface Acoustic Waves in Various Fluids," presented at the Frontiers in Optics 2012, Rochester, NY, 2012.
[6]   J. Zehnpfennig, M. Letarte, R. W. Sadowski, and J. J. Raftery Jr., "Surface Optomechanics: Calculation of Love Surface Acoustic Waves on Microresonators," presented at the Conference on Lasers and Electro Optics 2012, San Jose, CA, 2012.
[7]   L. Kinsler, A. Frey, A. Coppens, and J. Sanders, "Fundamentals of acoustics," 1999.
[8]   D. S. Ballantine and Knovel, Acoustic wave sensors: theory, design, and physico-chemical applications. San Diego: Academic Press, 1997.
[9]   Pham Chi Vinh and P. G. Malischewsky, "Improved Approximations of the Rayleigh Wave Velocity," Journal of Thermoplastic Composite Materials, vol. 21, pp. 337-352, July 1, 2008 2008.
[10]   J. Zehnpfennig, M. Letarte, D. Covell, K. E. Sheetz, and J. J. Raftery Jr., "Surface Optomechanics: Analytic Solution of Detection Limits of Surface Acoustic Waves in Various Fluids," presented at the Frontiers in Optics 2012, Rochester, NY, 2012.
[11]   COMSOL, "COMSOL Multiphysics v4.3," 4.3 ed: COMSOL, 2012, p. Multiphysics finite element solver.
[12]   J. Zehnpfennig, "Calculating Opto-Mechanically Induced Surface Acoustic Waves in a SilicaWhispering Gallery Microresonator," in COMSOL Boston 2011, Newton, MA, USA, 2011, p. 5.
[13]   J. Zehnpfennig, "Calculating and Observing Opto-Mechanically Induced Surface Acoustic Waves in Silica Whispering Gallery Microresonator," presented at the COMSOL Boston 2011, Newton, MA, USA, 2011.
[14]   J. Zehnpfennig, G. Bahl, M. Tomes, and T. Carmon, "Surface optomechanics: calculating optically excited acoustical whispering gallery modes in microspheres," Optics Express, vol. 19, p. 9, 2011.
[15]   J. Zehnpfennig, G. Bahl, M. Tomes, and T. Carmon, "Surface optomechanics: calculating surface acoustic wave generation on microsphere via photon-phonon interaction," presented at the PHONONS2012 - XIV International Conference on Phonon Scattering and Condensed Matter, Ann Arbor, MI, 2012.

[16]   J. D. Zehnpfennig, G. Bahl, M. Tomes, and T. Carmon, "Surface Optomechanics: Observation of Surface Acoustic Resonances," presented at the Frontiers in Optics 2012, Rochester, NY, 2010.

[17]   R. W. Boyd, Nonlinear optics. San Diego, CA: Academic Press, 2003.

[18]   J. Zhu, S. K. Ozdemir, Y.-F. Xiao, L. Li, L. He, D.-R. Chen, et al., "On-chip single nanoparticle detection and sizing by mode splitting in an ultrahigh-Q microresonator," Nature Photonics, vol. 4, pp. 46-49, 2009.

[19]   Y. Shen and J.-T. Shen, "Nanoparticle sensing using whispering-gallery-mode resonators: Plasmonic and Rayleigh scatterers," presented at the Frontiers in Optics/Laser Science 2012, Rochester, NY, 2012.

Cadet Capstone Design and Independent Study Projects

Background

Cadets in the Department of Electrical Engineering and Computer Science must participate in a capstone design experience during their final two semesters at the academy. The capstone design experience requires the students to integrate math, science, and engineering into the design of a comprehensive system. To succeed, each student must participate as a member of a design team to execute the engineering design methodology to design, build, and test an electronic system or sub-system. The experience is a culminating event bringing together skills and knowledge develop while pursuing a major in electrical engineering, computer science, or information technology. Because these three different majors exist within a single department, the ability to form multidisciplinary and interdisciplinary teams often present. Projects are open-ended and must result in a demonstration, usually by a hardware, software, or information technology prototype system, meeting the pre-determined or negotiated constraints. The project listed below was conducted in the Photonics Research Center (PRC). Throughout the project, faculty advisors served as government materiel developers or customers driving the specifications and constraints of the problem. The cadet design team served the prime contractor, researching and developing their prototype system for demonstration at Projects Day.

Select EE&CS cadets choose to participate in an advanced individual study course. This course is a one-on-one experience with a faculty advisor investigating a topic of mutual interest to the cadet and faculty member. The research projects done as part of these efforts do not require the amount of design required of the capstone courses. Cadets seeking to meet the requirements for Honors distinction will commonly choose to take an advanced individual study course to help them do so. Likewise, cadets who desire to compete in recognized fellowship and scholarship programs, such as the National Science Foundation or Hertz Fellowships, will often participate in an advanced individual study course in order to broaden their scholarly experience and deepen their knowledge about a specific topic further than might normally be found at the undergraduate level.

Sponsorship of capstone projects and advanced individual study course by the Photonics Research Center allows cadets to leverage the facilities and capabilities of the Center while learning or researching photonics technologies and science.

The capstone project report for the *DemonEye – Laser Target Location Module* project is provided. Likewise, an example of a paper prepared by a cadet as part of his advanced individual study course is provided. Additionally, short one-page synopses of two additional cadet advanced individual study courses are provided.

Capstone Project Report: DemonEye – Laser Target Location Module

Cadets Derek Wales, George Hopkins, and John Eischer
Faculty Advisors: LTC Gregory R. Kilby and Dr. Wenli Huang

Photonics Research Center
Department of Electrical Engineering and Computer Science
United States Military Academy
West Point, NY 10996. USA

Abstract. We as a team set out to build a device that would allow the individual 11 series and 19 series soldier to receive a 10 digit grid of what the soldier is looking at, a 10 digit grid of where the soldier is, and the distance to the target. It needed to be inexpensive enough that it could be mass produced and commercialized. The end state of the project was a design with all commercial parts and came in under $2000, under 3 lb, and has maximum range of 2000m. This way every squad leader deploying could get one. We produced a module that had a backlight system for use in night operations and met the weight, cost, and range specifications. The current module is still being tuned to achieve the desired accuracy of +/- 10m. Currently our target's accuracy is +/- 14m at 250m.

Introduction

On the modern battlefield, it has become increasingly important to know your own position as well as the position of key terrain, enemy, and civilians about the battlefield. Recently, four Marine advisors embedded with an ANA (Afghan National Army) unit were killed in Afghanistan. Caught in an ambush by an entrenched enemy force that held the high ground, air cover was not immediately available, and indirect fire was withheld because of concerns about rounds striking a nearby village. If the advisors possessed a device that could determine the precise grid coordinates of enemy positions, indirect fire assets would have been far more likely to provide the immediate suppressive fire needed. This is especially true as the Excalibur (GPS Global Positioning System) guided artillery shell) and EPIAFS (Enhanced Portable Inductive Artillery Fuse Settlers) artillery fuse (GPS guided screw in fuse body for standard "dumb" rounds) now give artillery sub 10 meter accuracy at extreme ranges, but only if precise target grid coordinates are available.

The Army's current solution to providing precision target coordinates is the MELIOS (Mini Eye Safe Laser Infrared Observation Set). This has several drawbacks from the standpoint of non field artillery users. First, MELIOS weighs six pounds. With soldiers already carrying between 70-100 pounds of equipment, and with current laser range finders weighing 6 ounces a lighter weight system can be fielded. Additionally, the MELIOS system with required components costs upwards of $15,000 makes widespread fielding to the squad level unlikely. Finally, MELIOS is not a standalone system, but feeds data into a personal computer, which is typically used for field artillery observers, before there are any sort of actionable coordinates that can be fed to AFATDS (Advanced Field Artillery Tactical Data System). This requires a higher level of user training.

MELIOS is a good solution for the field artillery community however; the cost, weight, and complexity prevent it from reaching the majority of Army users who need it. Team DemonEye is not trying to replace the MELIOS. Our Team just hopes to design a low cost, lighter module that

meets squad and platoon level needs. We believe that in partnership with industry our design can be rapidly fielded and deployed to line units who want to increase their combat effectiveness and situational awareness on the battlefield.

Problem Statement

Team DemonEye will develop a low cost module that will provide the warfighter with an accurate target location, as well as the soldier location and distance to target. A key to this success will be constraining requirements to what can be reasonably adapted from COTS (commercial off the shelf units) units available for the high end sportsman. There is an order of magnitude difference between this level and the more expensive equipment a surveyor might use. DemonEye will have the ability to sense a reflective target at 2000 meters, and provide a target grid coordinate with +/- 1 degree of azimuthal accuracy, combined with displaying an observer grid coordinate that is accurate to within 10 meters. The system should meet the following specifications:

- The objective range for the system is 2000 meters. Threshold range is 1000 meters.
- The objective system accuracy is +/- 5 m. The threshold accuracy is +/- 10 m.
- Under 3 lbs
- Eye safe
- Size under 80 in^3
- System must produce a set of grid coordinates for the target as well as for the physical location of the unit.

Description of the System

Several components are used to construct the target laser module. Refer to Figure 1 for a block diagram of the system. The main component is the microprocessor. This will connect the sensors to output the information to the user. The different sensors are a laser range finder, a compass, a GPS module and an inclinometer. The laser range finder will collect the distance to the target. The compass will give the direction that the target is from the user. The GPS module will give the location of the user. The inclinometer will give the angle of tilt that the target is from the user. Using the GPS coordinates as a reference, the compass and the inclinometer determine from that point where the object is with respect to the user. The laser range finder determines the distance to that object. In essence, the module obtains a vector to the object using the GPS coordinates as the origin. The information is sent to the microprocessor where it is interpreted and output as a grid coordinate of the object. The concept behind the prophecy is not to create something someone has never attempted because a similar system is already in place. The concept is to create a cheaper and lighter item that is more practical for a soldier to use. The system is simple so that it is less complicated to use and repair. The parts that were purchased for the construction of the project were mass-produced and easy to obtain and install. The final concept will be all of the components integrated in a more compact design.

Figure 1. Block Diagram of the Subsystems
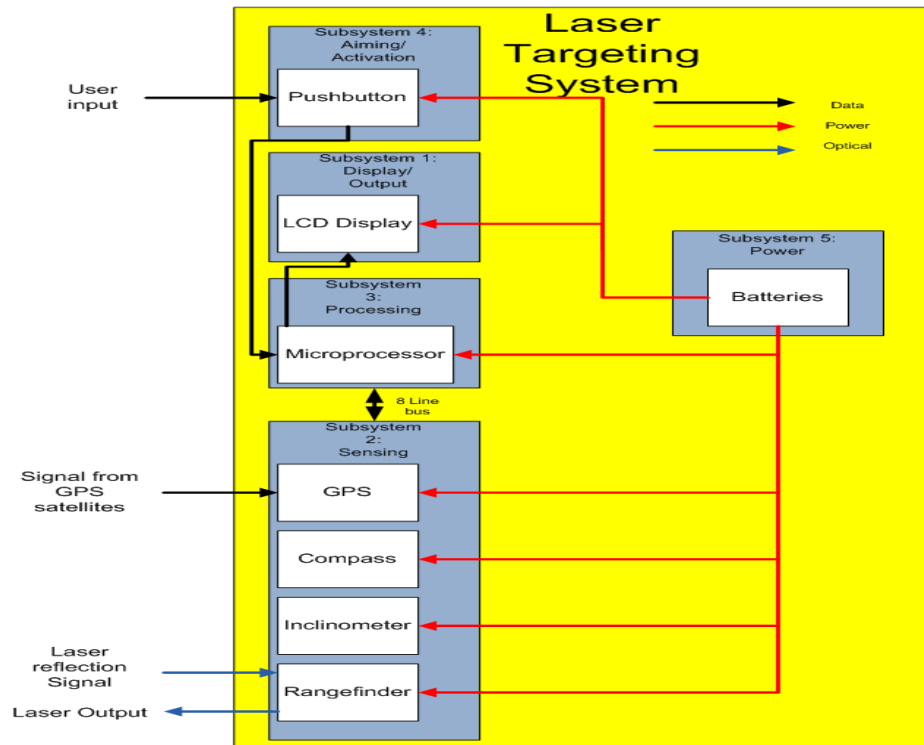
Results

The final result of the project is a working prototype. The integration of all the subsystems was successful and the final prototype is a packaged, handheld module that can easily be carried around for use and testing. The final prototype meets most of the specifications. The subsystem testing of different components have all been verified and they meet the specification for range and accuracy. The final prototype testing is to ensure that the integrated systems still meets the project specifications.

The final prototype did not meet our size requirement of less than 80 cubic inches. The module is around 150 cubic inches. The reason for this are the packaging limitations at our lab and the discrete components used. The future vision for the product is a much smaller module that meets the size requirement; this can easily be achieved by custom building a board for the microprocessor and not using the development board which has a lot of unused space. Also the use of surface mounted components and a more compact LCD screen would reduce the size. The project did meet the weight specification of being less than 3 pounds. The prototype weights 2.25 pounds. This weight would decrease as well through the miniaturization process.

The target's 10 digit grid coordinate was +/- 14 meters off at 250 meters from the target. The test was conducted using a map and the module itself. We used a known point as the origin and targeted another known point. Part of the error came from using a map that only gave an 8 digit grid coordinate. Unfortunately, without the expertise and measuring equipment of a professional surveyor, this is the best accuracy we can achieve. The current prototype uses a hand adjusted compass mount which allows for calibration between the laser range finder and the compass. This is also a cause of error.
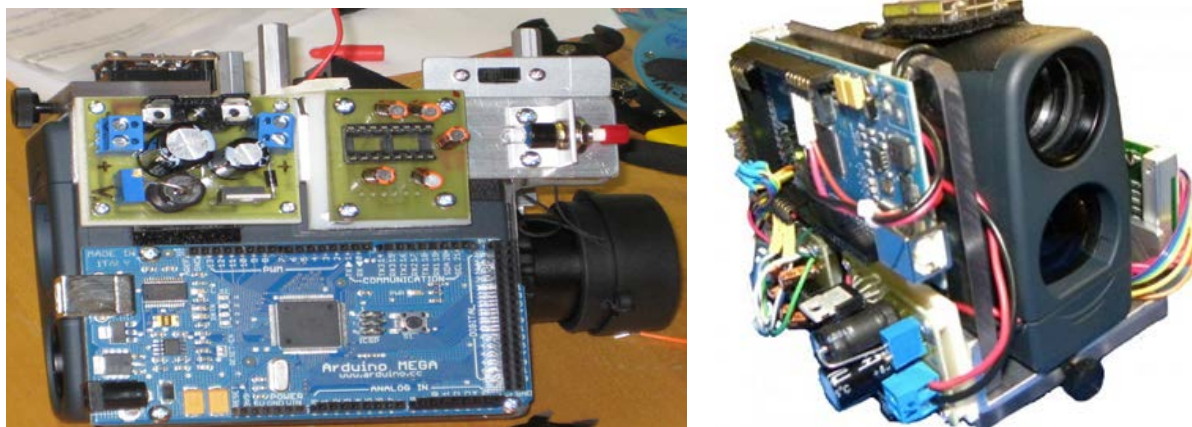
Project Pictures

Figure 2. Picture of Final Prototype

Recommendations for Future Work

From our working model, we as a team learned a lot about some future improvements before DemonEye is given to the individual warfighter in Iraq or Afghanistan. The most obvious ones are the size and the weight of the components themselves. Since the microcontroller is on a development board its size and power consumption could be reduced. Also if the module was build from the ground up for this functionality many of the components could be surface mounted or built into an integrated circuit. Another important consideration for the warfighter is power; soldiers need a device that lasts for more than an hour. This is another improvement that could be made. Since the Arduino board draws the most power once the microcontroller in taken off the board, we can switch to a new power source. We want to switch to AA batteries because they are readily available in the S-4 as they power the AN/PVS-14 night vision goggles. Another issue with power consumption is that many of the subsystems being powered do not necessarily have to stay on. The only device that needs to be on constantly is the GPS module. A solution to this is to create a program that shuts off systems that do not need to be powered constantly and only turns them on when the button is pushed in order to receive a ten digit grid coordinate. Additionally, a power save option which turns off the entire system after 2 minutes would compensate for a soldier's forgetting to turn it off, allowing the system to be used in times of need. If these improvements were made, the module could be much smaller and have significantly greater battery life.

Conclusions

DemonEye met most of the design specifications. Further testing is required to make sure the integrated system meets the specifications in achieving the desired grid coordinate. The module is currently hand calibrated which requires minute adjustments. The batteries tend to die quickly (within three hours). A more efficient design to improve battery life is to turn off subsystems that are not in use and only allow those parts that are necessary to be on in between targeting. The project was a success in that we were able to produce a working prototype that met most of the specifications.

Additional Information from the Faculty Advisors

- MIT Soldier Design Competition - 3d Place Award
- USMA Clark Innovation for Soldiers Award Winner
- EE&CS Best Solution to a Military Problem Award Winner
- Picked up by the U.S. Army Asymmetric Warfare Group for Prototyping at Johns Hopkins
  Applied Physics Lab (2LT Wales involved)

Then 2LT Derek Wales, '10, at the
Asymmetric Warfare Group

Capstone Project Report: Stimulated Raman Scattering in Single Mode Fiber

Cadet Kamal R. Wheeler
Faculty Advisors: COL Robert W. Sadowski, LTC Gregory Kilby

Photonics Research Center
Department of Electrical Engineering and Computer Science
United States Military Academy
West Point, NY 10996. USA

Abstract. The experiment demonstrates the generation of multiple Stokes lines through stimulated Raman scattering using a pulsed 532nm laser in 300m of silica fiber. Using the pulsed laser and silica fiber, it was possible to generate up to eight visible Stokes lines. The stimulated Raman scattering occurred when a threshold of 4W was reached by the laser with a 870 ps pulse at a 9.75 kHz repetition rate. The peak power of the laser was in excess of 250W. The Stokes lines were observed from 546 to 656 nm.

Introduction

Stimulated Raman scattering is a relatively simple experiment with numerous applications. The experiment can be completed with a pulsed output laser and silica fiber. Coupling with the vibrations of the host glass causes a broad optical emission at a longer wavelength in glass fiber. The Stokes lines can pump additional lines provided sufficient intensity remains. The output consists of various Stokes orders of different wavelengths depending on the pump power in the fiber, core dimensions, and fiber length. Coupling can result in Raman scattering with many colors within the visible light spectrum and near infrared spectrum.

Stimulated Raman scattering has a variety of real world applications. It can be used to make optical amplifiers and lasers. The optical amplifiers created with Raman scattering have a number of advantages compared to typical erbium doped fiber amplifiers. The Raman fiber amplifier has a wider bandwidth, it is extendable by use of multiple pumps, operates over a broad range of wavelengths, it is an arbitrary fiber host, and it is compatible with existing links.[2] Raman fiber lasers can be constructed from Raman optical amplifiers by providing feedback to the amplifiers. These lasers offer a greatly expanded range of possible wavelengths.[2] Another practical application of simulated Raman scattering is spectroscopy. Spectroscopy is possible because Raman scattering reveals the underlying vibrational characteristics of a material.[2]

Theory

Raman Scattering

Stimulated Raman scattering is a process which cause a photon at a frequency defined as hv_1 to shift to a lower frequency defined as hv_2. The frequency shift occurs because of an interaction with a material. The process of Raman scattering is inelastic.[2] Raman scattering results because of an interaction with the rotational and/or vibrational mode of a molecule or solid.[2] As the photon travels through the medium it releases energy which causes the molecules within the material to vibrate. The vibrations cause the unusual behavior.

Stimulated Raman Scattering

Stimulated Raman scattering is achieved when two photons enter a medium. One photon is known as the signal photon and the other is the pump photon. The signal photon creates a second signal photon from the pump photon. The energy from the pump photon is Stokes shifted so its frequency will match the frequency of the original signal photon. The Stokes shift creates an excess of energy within the medium. The extra energy is transferred to the vibrational modes of the medium.[2] The interaction in Raman scattering is a parametric third order nonlinear optical process.[2]

Experimental Setup

The experiment was designed to be relatively simple to create stimulated Raman scattering. The basic components were the pulsed output laser, mirrors, single mode fiber, lenses, and diffraction grating.
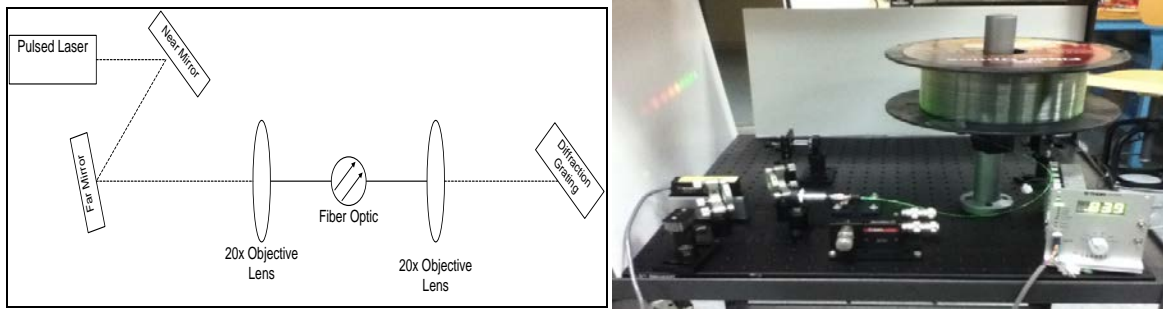
Figure 1. Experimental Setup

The schematic and picture of the experimental setup is depicted in depicted in Figure 1. The laser is aligned along the optical bench using two turning mirrors. The 20x objectives focus the beam and prepare it to be coupled into the fiber. The fiber optic cable is 300m of single mode fiber at 633 nm. The long interaction length and high source peak power enabled the necessary nonlinear behavior to achieve Raman scattering. The diffraction grating is used to separate the different wavelengths from the output beam.

Fiber Optic Cable

SM600 fiber was used to achieve the desired effects during the experiment. SM600 fiber is a standard gerrmanosilicate core with an N.A. ~ 0.12 and approximate mode field diameter of 4.3 μm at a wavelength of 633 nm. Fixing the input lens to a standard 20x microscope objective required careful placement of the objective in order to maximize coupling via modematching. The goal was to match the mode field diameter of the fiber with the diameter of the incident beam. The divergence angle was experimentally determined to be 4.67 mrad. The divergence angle was used to mathematically determine the initial laser beam waist and the optimal objective distance matching the focused spot size to the fundamental fiber mode. Calculations indicated that maximum coupling should occur at a distance ≈150 mm from the source.

Pulsed Output Laser

The laser used in the experiment was a JDS Uniphase pulsed microchip laser. The average output power was determined to be approximately 4.5 mW. The laser is a doubled Nd:YAG device operating at 532 nm in the center of the visible spectrum. The laser had an average pulse width of 872 psec and average pulse repetition rate of 9.75 kHz. The approximate peak power at

532nm was 529W. The source supply required ±15V and 1.5A total. A TEC controller stabilized the pump laser wavelength. The diode pump lasers operated with 800mA current.

Predicted Input Power for Raman
Based up Stolen's prediction for initial input pump power of 18.5 W into 50m of single mode fiber with a 3.75 micron diameter, we can estimate the launched pump power required to initiate the first Stokes order through Equation [1]

$$P_{Critical} = P_{Critical\ Stolen} \cdot \frac{L_{Eff\ Stolen}}{A_{Eff\ Stolen}} \cdot \frac{A_{Eff\ SM600}}{L_{Eff\ SM600}} \quad [1]$$

We estimate this power to be 4.05W. With an incident power of 529W and 50% coupling, we should easily see the first Stokes Order. .

Results
During the experimentation, stimulated Raman scattering was observed. The number of stokes orders was proportional to the amount of power coupled into the fiber. During the experimentation, nine different Stokes orders were observed. The orders are shown below in Figure 2.
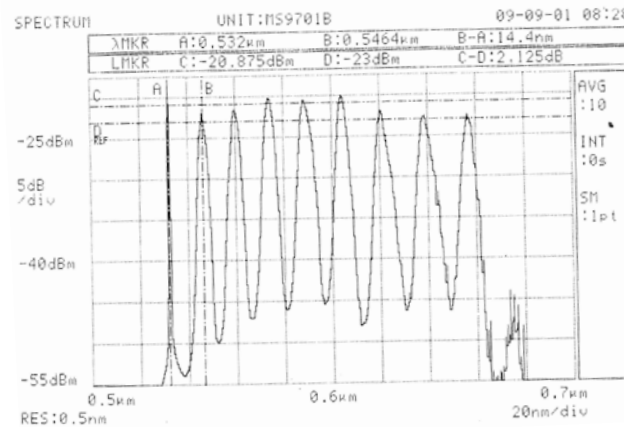
Figure 2: Stokes Lines

As the amount of peak power coupled into the fiber increased the number of Stokes modes increased. The maximum number was limited to nine Stokes modes. Adjusting the alignment allowed the coupling efficiency to increase until the coupling efficiency was about 50%. The Stokes orders demonstrated the same behavior as experimentally determined by Bell Laboratories. The first Stokes spectrum was dependent on the power of the laser.[1] As seen in Stolen, the broad peak around 440 cm^{-1} saturates (depicted in Figure 3 at 12.76 nm) as launched pump power is increased and becomes a sharp peak at 490 cm^{-1} (14.4 nm) as seen in Figure 2.

The chart in Figure 2 depicts the Stokes orders. The difference between the peak of the highest Stokes order and the lowest Stokes order is 14.4 nm. The ninth order is shown on the far right and is smaller than all the other orders. Its smaller size is attributed to the coupling efficiency into the fiber. The order is nearly in the infrared.
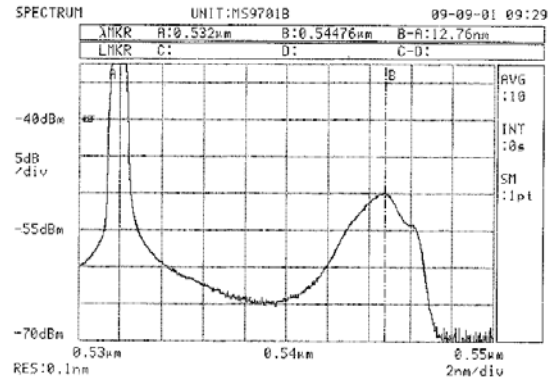
Figure 3: Stokes spectra

Figure 3 shows how the first Stokes order behaves as a pump for the second stokes order. The power of the laser is increased and the power of the second Stokes order increases faster than the first Stokes order. The peak at .532 µm is acting as the pump and the peak at .545 is the pump order.

Discussion and Conclusion

We demonstrated stimulated Raman spectrum in a standard single mode fiber. It was possible in our setup create up to nine different Stokes orders although the ninth required the optical spectrum analyzer to measure. The Stokes orders not only transfer energy to longer wavelengths but also transfers energy to longer wavelengths within each Stokes order.[1] It may be possible in the future to generate more Stokes orders by using a more powerful laser. Operating the experiment in the infrared may increase the number of orders available also because infrared experiences less loss as it propagates through the fiber. Figure 4, shown below, is an image of the final experiment with the Stokes orders projected on the left side of the image. Only the Stokes orders in the visible light spectrum are seen in the image.
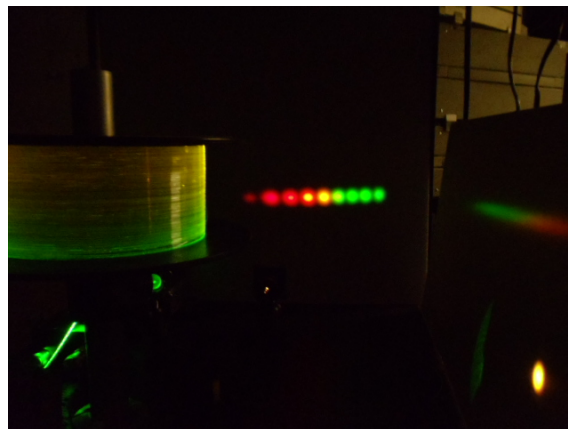
Figure 5: Diffracted Output

References

R. H. Stolen and Clinton Lee, "Development of the stimulated Raman spectrum in single-mode silica fibers," J. Opt. Soc. Am. B, vol. 1, No. 4, pp. 652-657, August 1984.

B.E.A. Saleh and M.C. Teich, "Fundamental of Photonics," John Wiley & Sons, Hoboken, 2007.

Thorlabs, "Single Mode Fiber: 600 to 860nm," Thorlabs.

Capstone Project Report: Dense Wavelength Division Multiplexing

Bradley E. Campbell
Faculty Advisor: COL Robert W. Sadowski

Photonics Research Center
Department of Electrical Engineering and Computer Science
United States Military Academy
West Point, NY 10996. USA

Abstract. We report on multiplexing 40 distributed feedback lasers with ITU 100 GHz channel spacing onto a single mode telecommunications fiber in the C band near 1550 nm. A commercial arrayed waveguide grating coupler was utilized for both input and output enabling Dense Wavelength Division Multiplexing or DWDM. A 50km strand of standard SMF-28 telecommunication fiber and EDFA were to be used in the optical channel.
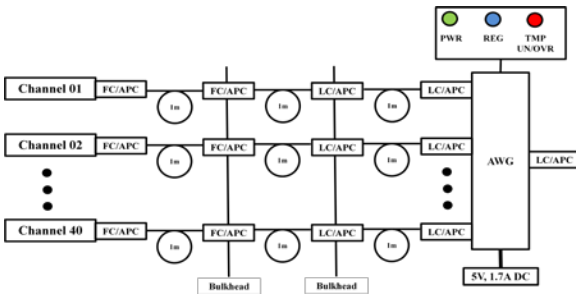
Figure 1. Mux/Demux Setup
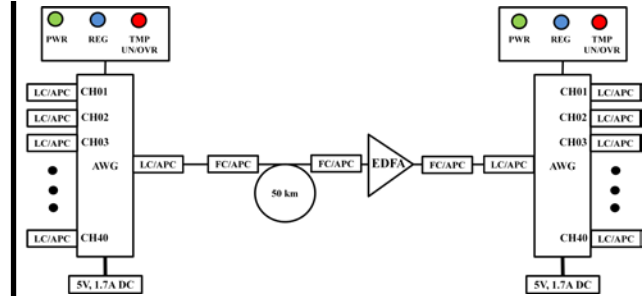
Figure 2. Link Setup

Figure 3. Patch Panel

Channel	Laserbank		Tested	
	Centered Frequency (nm)	Power (mW)	Centered Frequency (nm)	Power (mW)
1	1528.77	10.7	1528.69	9.1
2	1529.55	9.7	1529.51	6.7
3	1530.33	10.9	1530.31	9.6
4	1531.12	10.2	1531.09	9.6
5	1531.81	10.6	1531.75	10.3
6	1532.68	10.4	1532.65	9.5
7	1533.47	9.97	1533.45	8.1
8	1534.25	11	1534.23	10.1
9	1535.04	10.9	1535.03	9.9
10	1535.82	10.8	1535.79	9.9
11	1536.61	10.5	1536.57	10.1
12	1537.4	10.9	1537.35	9.1
13	1538.19	11.4	1538.15	9.5
14	1538.98	12.8	1538.91	12.3
15	1539.77	11.6	1539.73	10.7
16	1540.56	11	1540.53	10.2
25	1547.72	11.1	1547.66	12
26	1548.51	12.3	1548.48	11.7
27	1549.32	13.7	1549.28	10.9
28	1550.12	12.2	1550.06	11.8
29	1550.92	11.8	1550.94	8.9
30	1551.72	12.6	1551.7	11.4
31	1552.52	12.5	1552.46	12
32	1553.33	11.5	1553.3	11.8
33	1554.13	11.5	1554.12	9.7
34	1554.94	11.3	1554.9	9
35	1555.75	10.2	1555.72	9.5
36	1556.55	11.1	1556.52	9.9
37	1557.36	10.5	1557.32	10.3
38	1558.17	10.9	1558.06	10
39	1558.98	10.8	1558.94	11.1
40	1559.79	11.4	1559.74	9.8

Figure 4. DFB Test Data

Capstone Project Report: Compact Ultra-Bright Supercontinuum Light Source

Cadet Logan J. Hardy
Faculty Advisor: COL Robert W. Sadowski

Photonics Research Center
Department of Electrical Engineering and Computer Science
United States Military Academy
West Point, NY 10996. USA

Abstract. We report on supercontinuum generation in a nonlinear photonic crystal fiber using a passively Q-switched laser at 1064nm. The input beam is a pulsed 6.5 kHz rep rate laser with a peak power of more than 14 kW that is coupled into 50m of photonic crystal fiber. The primary generation mechanism arises from four-wave mixing due to the high non-linear coefficient of the fiber. Average power exiting the fiber was 6.8 mW with output ranging from 450 nm to 1750 nm.

Figure 1: Experimental Setup

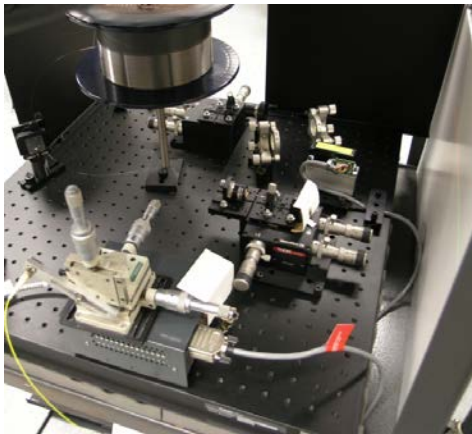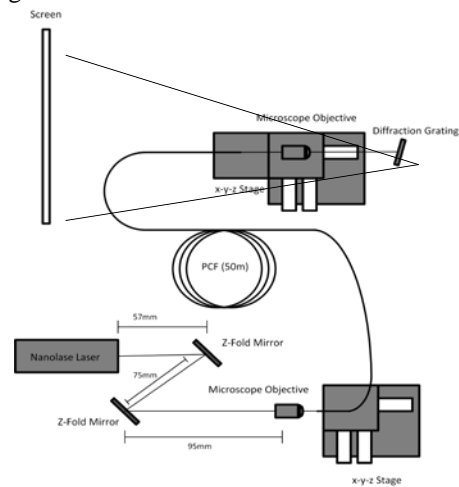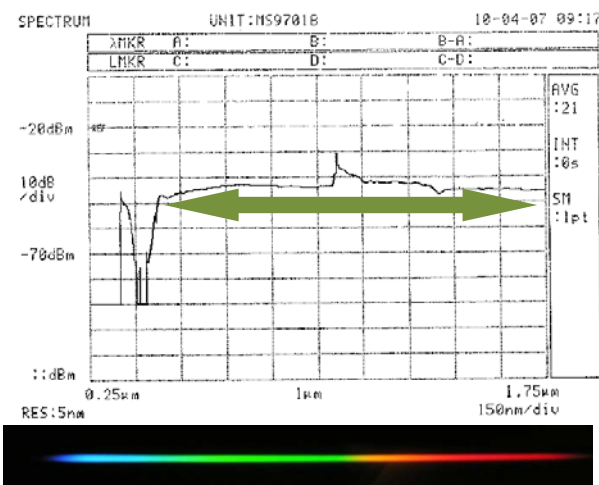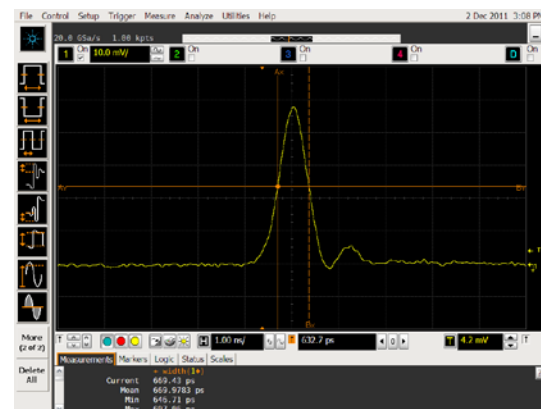Figure 2: Diagram of Experimental Setup

Figure 3: Output Spectrum

Figure 4: Input Pulse

Department of Physics and Nuclear Engineering

Analysis of the Joint High Energy Solid State Laser for Neutralization of Mortar Rounds in Flight

LTC Lou Florence and LTC John Hartke

Photonics Research Center
Department of Physics and Nuclear Engineering
United States Military Academy, West Point, New York 10996
Email: louis.florence@usma.edu

Abstract. This project develops models and verifies assumptions of a High Energy Laser engagement with an 81mm mortar projectile in flight. Work centers around the absorptive and refractive atmospheric effects on the beam, the light-matter interactions at the target, the mechanical employment of the system, the economic viability of the system, and tactical employment considerations. Conclusions of each study feed additional studies in an attempt to better model the targeting effects while teaching cadets essential modeling and experimental techniques.

Background

The West Point High Energy Laser team first formed in August, 2006. The original mission of the team was to analyze the effectiveness of directed energy weapons against Improvised Explosive Devices (IEDs). Then, the High Energy Laser Joint Technology Office (JTO-HEL) dictated the design criteria for a 100kW laser with the purpose of defeating enemy rocket and artillery rounds. While the effects of High Energy Laser systems on rocket and missile targets have been well documented by the Airborn Laser (ABL) system, effects on artillery and mortar rounds have not been studied as well. Cadets at the United States Military Academy (USMA) formed a multidisciplinary team to analyze the effectiveness of the JHPSSL to neutralize an 81mm mortar round.

Initial studies concentrated on the deployment of the system and crude modeling of the heat transfer on the target. This included a detailed analysis of the atmospheric effects on the propagation of the High Energy Laser. The HEELIOS program developed for the ABL provided a modeling system to determine the effective power delivered to the target as a function of atmospheric disturbances such as dust, clouds and humidity. The cadets also evolved the heat transfer model of the projectile from a cylinder ("the flying soup can") to a mortar round shape using MATLAB to conduct a finite element analysis.

During the academic year 11-12, the cadet team continued to focus on the use of the JHPSSL. The mechanical engineering cadets developed a MATLAB-based heat transfer model, and then compared results to commercial heat-transfer software (COMSOL). Physics cadets determined the beam characteristics at the target, accounting for atmospheric propagation and beam quality. Additionally, the physics cell of the PRC acquired a 1-kW laser operating at 1.07 microns in order to verify the heat transfer model outcomes of the mechanical engineers. The system engineer cadets produce comparative studies of weapons systems to determine the feasibility of employing a system based the JHPSSL.

Theory
When the explosive portion of a mortar round reaches a certain temperature, the round will fail. The time required to achieve this temperature for a given laser power is the system's kill time. Necessary and reasonable assumptions are that the mortar round can be accurately tracked throughout its flight, and that the laser spot size can be continuously controlled by the beam steering system. These assumptions are validated by the testing of the Airborne Laser (ABL) system. The kill time allows comparison of weapons systems and evaluation of various system parameters.

Determining the kill time is possible through modeling efforts. If the amount and distribution of laser power on the outer surface is known, and the heat acceptance of the outer surface is known, the heat transfer throughout the round can be modeled. As heat is continuously transferred into the system, the temperature of the inner surface will increase. This temperature change is dependent upon the geometry and the material properties of the casing. By accurately modeling these parameters, finite element analysis of the steel casing should produce accurate kill times for various laser powers.

The kill times of the laser system, along with atmospheric limitations (weather) and the system's logistical chain, allow for comparative studies with other anti-mortar system such as the C-RAM. Atmospheric effects can be modeled using HEELIOS software developed for the ABL system. The logistic chain can be determined based on power requirements. By weighting such properties as speed of acquisition, average engagement times, and range limitations, recommendations can be made pertaining to the deployment of the system.

Experimental
The ultimate comparative data would be the kill time of an actual HEL system on an actual mortar round. Unfortunately, unclassified kill times are not available. Therefore, the modeled change in temperature of the inner surface must be compared with actual measurements. These measurements can be accomplished by placing a 1kW laser with a given beam profile onto a piece of steel with known dimensions. The temperature at several locations on the back surface of the steel can be measured with thermocouples. The model should be able to predict the temporal and spatial changes in temperature as measured by the thermocouples. Once the model is verified, assumptions can be made to determine the effects of laser systems with greater powers.

The HEL is directed onto the target with one pick off with 99% reflectivity and a turning mirror. This 1% of power that transmits through the pick off provides power to a power meter and to a beam profiler so that any laser transience can be monitored. A FLIR systems infrared camera collects information about the infrared heating effects of the front surface of the target. This data can be converted to a two dimensional temperature map by knowing *a priori* the emissivity of the steel. Additionally, a CCD camera with an infrared filter monitors the front surface topographic changes. See Figure 1. These monitoring systems allow for temperature readings as a function of time and space which can then be compared to predictions from the finite element heat transfer model.
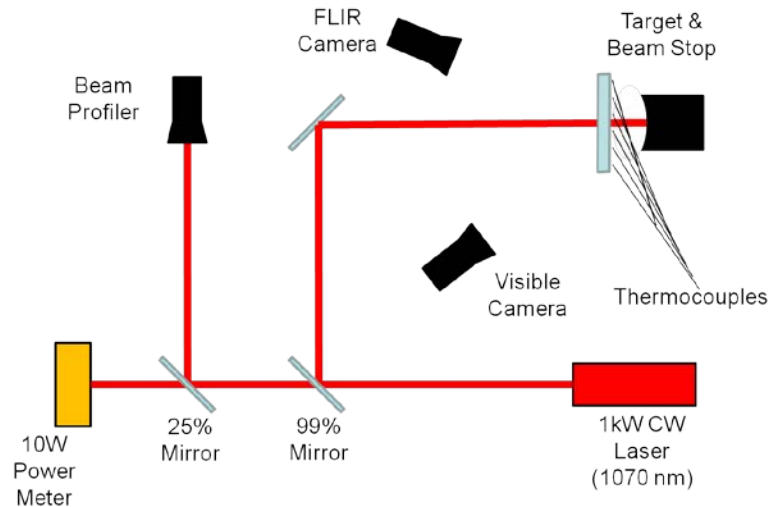
Figure 1. Experimental set-up of the 1kW HEL experiment.

Results and Discussion

The temporal and spatial temperature changes are shown in Figure 2. There is a notable difference between the modeled predictions and the measured data. The model underestimates the time required to achieve the temperatures. We believe this is due to heat removal caused by the flowing of metal away from the center of the power distribution.

A systems comparison with the Phalanx system showed that the laser system was less effective. The two systems had similar average engagement times, but the laser system was not as available due to weather concerns. It should be noted that cost, logistics, repair and upkeep, and training were not included in the comparison.
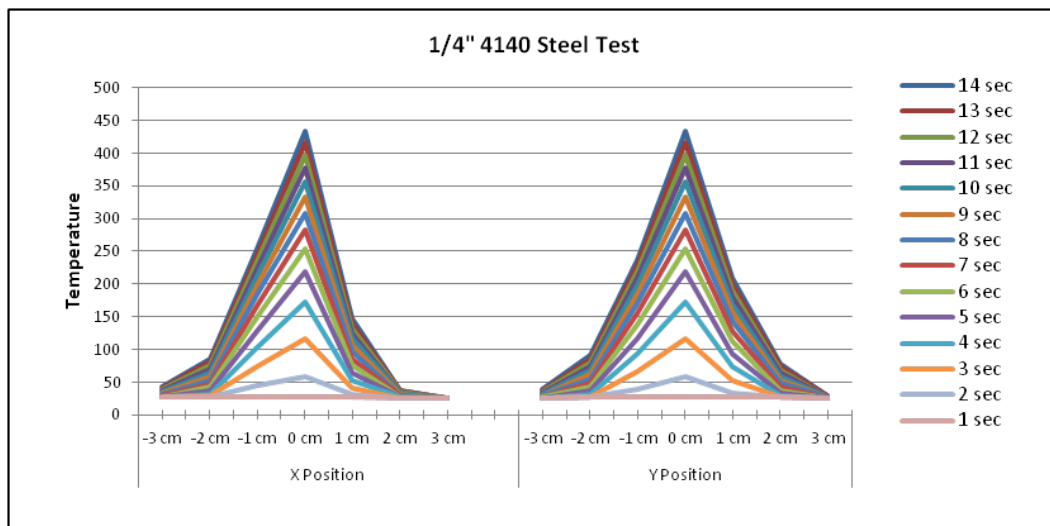
Figure 2. Kill Time experimental validation measurements.

Future Direction

As discussed above, greater fidelity between the model and the measured data can be achieved by adding heat removal to the model. This can be accomplished by precisely measuring the metal flow away from the center of the power distribution. Additionally, the model does not account for mechanical jitter in the laser system or movement of the target as it travels through the air. By varying the beam location at low and high frequencies and analyzing the effects on measured temperatures, the model can be improved to account for realistic movement of the beam and the target. Finally, this system can be used for the engagements of other military targets. The ability to engage both metal and composite targets from a secure location will add to the force protection of the Army and its Soldiers.

Conclusion

This interdisciplinary project directly contributes to the education of numerous cadets in the context of defense related project development. Cadets are afforded the ability to interact with professional researchers in a meaningful way. By advancing the capability to model and measure useful quantities of this project, the development of cadets into technically capable leaders is enhanced.

Cadet/Faculty Involvement

Cadets: Jordan Smith, Tyler Federwisch, Daniel Blaine, Tim Bowers, Cliff Crawford, Robert Allibone, Jeffrey Gorn, John Paulson , Zachary Brownlee, Benjamin Troxell, Bethany Houdeshell, Adam Demoss, Benjamin Koenigsfeld, Theodore Yang, Josh Maurmeier, Lisa Taylor, Steven Wathen, Matthew Krause, Dhruvkumar Desai, Clay Canning, Dan Gluszko, Christopher Larson, Nicole Myers, and Ryan Townsend.

Faculty Advisors: LTC John Hartke (Physics), MAJ Rob Grimming (Physics), Dr. Gunnar Tamm (Mechanical Engineering), Dr. Roger Burk (Systems Engineering), LTC Lou Florence (Physics), MAJ John Evangilista (Mechanical Engineering), MAJ Karl Ludeman (Physics), MAJ John Delong, LTC Walter Cole (Physics), MAJ Walt Zacherl (Physics), Dr. John Dehn (Law), COL David Wallace (Law)

Publications/Presentations

1. Gorn, J., Paulson, P., Brownlee, Z., Smith, J., Burk, R. "High Energy Laser as a Competitive Defense Against Rockets, Artillery, Mortars and UAV's," presentation at the 2012 Directed Energy Systems Symposium, National Institute of Standards, Gaithersburg, MD, 2-5 April 2012.

2. Smith, J., Grimming, R., Sheetz, K., Hartke, J., "Development of a Laboratory Experimental Platform to Validate Laser Engagement Models," presentation at the 2012 Directed Energy Systems Symposium, National Institute of Standards, Gaithersburg, MD, 2-5 April 2012.

3. Koenigsfeld, B., Dehn, J., Wallace, D., Sheetz, K., Hartke, J., "High Energy Laser Weapon System: Legal Analysis," presentation at the 2011 Directed Energy Systems Symposium, Naval Postgraduate School, Monterey, CA, 28 March – 1 April 2011.

4. Peterson, P., Tamm, G., Grimming, R., Johnston, J., Delong, J., Sheetz, K., Hartke, J., "Computational Thermal Model for Destroy a Mortar with a High Energy Laser," presentation at the 2011 Directed Energy Systems Symposium, Naval Postgraduate School, Monterey, CA, 28 March – 1 April 2011.

5. Maurmeier, J., and Taylor, L. , "High Energy Laser as an Army Defense against Rockets, Artillery, and/or Mortars (RAM)", presentation at the 2010 Directed Energy Systems Symposium, Naval Postgraduate School, Monterey, CA, 28 March – 1 April 2010.

6. Maurmeier, J., Taylor, L., Wathen, S. and Krause, M., "Value Modeling to Score Alternative System Designs for Forward Operating Base Defense", presentation at the 2010 Directed Energy Systems Symposium, Naval Postgraduate School, Monterey, CA, 28 March – 1 April 2010.

7. Desai, D., "Target Discrimination with a Laser Interrogation", presentation at the 2010 Directed Energy Systems Symposium, Naval Postgraduate School, Monterey, CA, 28 March – 1 April 2010.

8. Myers, N., "Is It Worth It? Defense Procurement Impacts at the Sub-State Level", presentation at the 2009 Directed Energy Systems Symposium, Naval Postgraduate School, Monterey, CA, 2-5 March 2009.

9. Larson, C., Canning, C., "Thermal Modeling of High Energy Lasers Using Dynamic Simulation With A Finite Element Analysis," presentation at the 2009 Directed Energy Systems Symposium, Naval Postgraduate School, Monterey, CA, 2-5 March 2009.

10. Gluszko, D., Townsend, R., "High Energy Laser Characteristics' Impact on Neutralization of an 81mm Mortar Threat," presentation at the 2009 Directed Energy Systems Symposium, Naval Postgraduate School, Monterey, CA, 2-5 March 2009.

Yb^{3+}:KGW Ultrashort Pulse Laser Development, Characterization and Application

LTC Louis A. Florence and LTC Kraig E. Sheetz

Photonics Research Center
Department of Physics and Nuclear Engineering
United States Military Academy, West Point, New York 10996
E-mail: kraig.sheetz@usma.edu

Abstract. Over the past decade, ultrashort pulse lasers have become valuable research tools across many scientific disciplines. The extremely high peak powers achievable with femtosecond pulses has created the opportunity to leverage nonlinear light-matter interactions and open windows into molecular structures and processes previously beyond the reach of optical differentiation. We explore ultrashort pulse laser development to facilitate a deeper understanding of materials and interactions through applications such as nonlinear microscopy and micro-machining/micro-manipulation.

Background

Advancements in ultrafast laser technology over the past two decades have served as the driving force behind a wide range of high intensity light-matter interaction studies as well as metrology, micro-machining and biological research applications. Thanks in part to precision engineering of optical components and detectors, important developments in ultrashort pulse characterization and manipulation and creative application of nonlinear optical effects, researchers are applying an exciting new understanding of ultrashort pulse phenomena to a wide range of scientific challenges such as: advanced imaging techniques to examine how groups of cells function, such as networks of neurons, to better understand dynamic processes in the brain; extreme optical intensities to study laser-plasma interactions through the formation and sustainment of filaments in air; or careful manipulation of precision focal volumes to machine materials with a precision unimaginable just a decade ago. For all of these cutting-edge applications to move forward, so must the fundamental science behind the generation, propagation and characteristics of ultrashort pulses--from the oscillator design to the spectral manipulation and control, to the physics of the interaction with matter.

The term "ultrafast" is generally applied to lasers capable of generating pulses with a duration of 100 ps or less. In the four decades since the first demonstration of a picosecond pulse train [1], ultrafast lasers have evolved to the point where scientists without expertise in laser design and maintenance can purchase reliable off-the-shelf or "black box" ultrafast laser systems for application in their particular area of study.

A tremendous amount of research has gone into oscillator configuration, lasing media, pumping sources, mirror coatings and techniques for transitioning from continuous wave operation to stable pulse train generation, or mode-locked operation. Among the many significant advancements in ultrafast laser technology, two bear mention. First is the development of semiconductor diode lasers [2]. The cost, physical size, performance and reliability of laser systems were all drastically improved when diode lasers replaced lamps as pump sources. Second, and arguably the most

significant advancement in ultrafast laser technology, is the theoretical development and practical application of mode locking. Passive mode-locking techniques for the generation of ultra-short pulse trains are generally preferred over active techniques due to the ease of incorporation of passive devices, such as semiconductor saturable absorber mirrors (SESAMs) into laser cavities.

Leaning on the flurry of interest in ultrafast research and development, and driven by the broad range of emerging applications, the commercial laser industry has exploded with bench-top picosecond and femtosecond laser systems within the past 5-10 years. Most commercial systems are built around Ti:Sapphire–the workhorse of the ultrashort pulse research community since 1992 [3]. However, Yb-doped crystals and Yb or Er fibers are getting a foothold in the industry that addresses compact systems emitting at wavelengths that pick up where Ti:Sapphire leaves off (about 1 μm) and extends to about 1.5 μm.

In 2000, Brunner et al., demonstrated the first mode-locked $Yb^{3+}:KG(WO_4)_2$ (or KGW for short) laser [4]. Using a semiconductor saturable absorber mirror (SESAM) for passive mode locking, they generated 176-fs pulses at 1.1 W average power and 112-fs pulses at 200 mW average power. The center wavelength of their pulses was tunable from 1032 nm to 1054 nm using a knife edge as a spatial filter inside the cavity. In solid state lasers, stable soliton mode locking is obtained by the interplay of self-phase modulation (SPM) in the gain material and negative group-delay dispersion [4]. In most of the early KGW/KYW (KYW uses Yttrium instead of Gadolinium but lasing characteristics are very similar) laser designs, prism pairs were used for dispersion compensation in the cavity, which allowed oscillator designers access to a few "buttons" for varying the center wavelength or bandwidth of the output pulses. Changing the prism insertion distance and, as above, exploiting the spatial chirp to filter with a knife edge are two such examples. In the past few years, Gires-Tournois interferometer (GTI) mirrors (sometimes just called "chirped mirrors") have become a more popular means of dispersion compensation due to their compactness and alignment simplicity. SESAMs, due largely to their operating stability at high powers and cavity design simplicity, have emerged as the the preferred method for passive mode locking of KGW and KYW lasers.

Although the demand for ultrashort pulse lasers with a wide range of pulse characteristics has generated a vast commercial market, we find that designing and building our own oscillators has a few significant advantages: (1) Cost. We can build our own KGW laser for about 10-20% of commercial cost; (2) Flexibility. We prefer to design the laser to fit the experiment rather than having to force the experiment to fit the "black box" laser characteristics; and (3) Discovery. We find that in designing and building our oscillators, we "stumble" on to some tremendous basic physics simply by pursuing efficiencies and unique pulse output characteristics.

Theory
Many of the efficiency advantages of Yb3+-doped double tungstates discussed above result from the rather simple energy level scheme consisting of only two relevant Stark manifolds: $^2F^{7/2}$ and $^2F^{5/2}$. However, there is also a downside to the energy scheme. The system is described as "quasi-three-level" because the closely spaced Stark levels within each manifold are only "quasi separate" and are actually connected by a Boltzmann distribution. As such, the lower laser level of quasi-three- level systems is so close to the ground state that an appreciable population in that level occurs at thermal equilibrium. A general energy diagram for quasi-three-level lasers is shown in

Figure 1(a). Given the spectral proximity of the absorption and emission lines (low quantum defect) this thermally populated lower laser level leads to reabsorption of the laser light which increases pumping thresholds and reduces efficiencies.
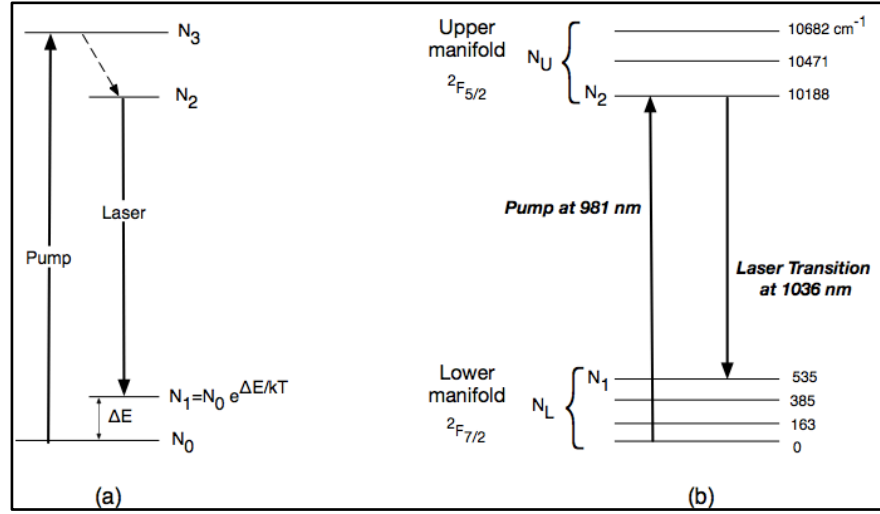

Figure 1. Quasi-three-level energy diagram. (a) General. (b) Yb3+:KGW with Stark levels shown in cm^{-1}. Arrows indicate pump and laser transitions.

Figure 1(b) shows the three degenerate Stark levels of the up- per manifold and the four degenerate Stark levels of the lower manifold. Arrows indicate the most relevant transitions for optical pumping and lasing. Phononic transitions lead to rapid intra-manifold thermalization so inversion can only be achieved at the lowest Stark level of the upper manifold. The total separation of the manifolds is <10,000 cm^{-1}. Because the next excited manifold is at <100,000 cm^{-1}, there are no nearby manifolds to serve as additional channels of loss such as upconversion or excited state absorption [5]. The primary loss mechanisms are thus spontaneous emission and reabsorption of laser light due to thermal population of the lower manifold Stark levels.

As we design and build our KGW lasers, it is important to have a theoretical model at hand in order to understand how various design parameters affect the performance of our oscillators. Below, we describe a general model for end-pumped solid state quasi-three level laser systems that begins with rate equations and works to an expression for pump power required for lasing threshold and ultimately to laser output power as a function of pump power. The following treatment is a combination of various quasi-three level models that have been developed over the past two decades [6–9] to address the presence of reabsorption loss and the effect of pump beam–laser beam overlap in the laser crystal. In this treatment, we will model the $^2F^{7/2} \rightarrow {}^2F^{5/2}$ lasing transition at <1036nm in KGW as shown in Figure 1(b). We assume that the ion population densities in the upper and lower lasers levels, N_2 and N_1 respectively, are in thermal equilibrium during steady state CW lasing and their relative populations can be described by a Boltzmann distribution. As such, N_2 and N_1 can be expressed as functions of total upper manifold ($^2F^{7/2}$) population density N_U and the total lower manifold ($^2F^{5/2}$) population density N_L according to: $N_2 = f_2 N_U$ and $N_1 = f_1 N_L$. The fractional populations in the lower and upper laser levels f_1 and f_2 are given by:

$$f_{1,2} = \frac{g_{1,2}}{Z_{1,2}} \exp\left(-E_{1,2}/kT\right) \qquad (1)$$

where,

$$Z_{1,2} = \sum_i g_i \exp\left(-E_i/kT\right) \qquad (2)$$

is the partition function. The laser rate equations governing the population density for the upper and lower laser levels can be written as:

$$\frac{dN_2(r,z)}{dt} = f_2 R r_p(r,z) - \frac{N_2(r,z) - N_2^0}{\tau_f}$$
$$- \frac{f_2 c\sigma[N_2(r,z) - N_1(r,z)]}{n} \Phi\phi_0(r,z) = 0, \qquad (3)$$

and

$$\frac{dN_1(r,z)}{dt} = -f_1 R r_p(r,z) - \frac{N_1(r,z) - N_1^0}{\tau_f}$$
$$+ \frac{f_1 c\sigma[N_2(r,z) - N_1(r,z)]}{n} \Phi\phi_0(r,z) = 0, \qquad (4)$$

where N^0 is the unpumped population in the respective level, c is the speed of light in vacuum, n is the index of refraction of the laser medium, σ is the stimulated emission cross section and τ_f is the lifetime of the upper manifold. R is the pump rate and is given by,

$$R = \frac{P_p \eta_a \eta_p}{h\nu_p}, \qquad (5)$$

where Pp is the incident pump power, $\eta_a = 1 - \exp[-\alpha l]$ is the fraction of incident pump power absorbed in a crystal of length l and absorption coefficient α, η_p is the pump quantum efficiency (the number of ions moved to the upper manifold per absorbed photon) and $h\nu_p$ is the pump photon energy. Φ is the number of laser photons, defined as the total laser energy after one round trip divided by the laser photon energy, and is given by,

$$\Phi = \frac{2l_c^* P_L}{ch\nu_L T}, \qquad (6)$$

where $l_c^* = l_c + (n-1)*l$ is the optical path length of the laser cavity with physical length l_c, P_L is the average laser output power, $h\nu_L$ is the laser photon energy and T is the transmission of the output coupler. The functions $r_p(r,z)$ and $\varphi_L(r,z)$ are the spatial distributions of the pump photons and laser photons, respectively. The pump photon distribution is normalized over the crystal:

$$\iiint_{\text{crystal}} r_p(r,z)\, dV = 1, \qquad (7)$$

and the laser photon distribution is normalized over the cavity:

$$\iiint_{\text{cavity}} \phi_L(r, z) \, dV = 1. \tag{8}$$

Using the population inversion density $\Delta N(r, z) = N_2(r, z) - N_1(r, z)$ together with (3) and (4) the rate equation for the population inversion density is,

$$\frac{d\Delta N(r, z)}{dt} = (f_1 + f_2)Rr_p(r, z) - \frac{\Delta N(r, z) - \Delta N^0}{\tau_f}$$
$$- \frac{(f_1 + f_2)c\sigma\Delta N(r, z)}{n}\Phi\phi_L(r, z) = 0 \tag{9}$$

where $\Delta N^0 = N_2^0 - N_1^0$ is the unpumped population inversion density. In thermal equilibrium, $N_1^0 \gg N_2^0$ so $\Delta N^0 \approx -N_1^0$. From (9) the steady state solution for the population inversion density can thus be written as,

$$\Delta N(r, z) = \frac{\tau_f f Rr_p(r, z) - N_1^0}{1 + \frac{fc\sigma\tau_f}{n}\Phi\phi_L(r, z)}, \tag{10}$$

where $f = f_1 + f_2$ is used for compactness. Note that at or below lasing threshold ($\Phi = 0$), the population inversion is,

$$\Delta N_{\text{th}}(r, z) = \tau_f f Rr_p(r, z) - N_1^0 \tag{11}$$

which is the same as for that of a four-level laser [170] except for the lower laser level population term N_1^0.

The corresponding rate equation for the total number of photons in the cavity can be written as,

$$\frac{d\Phi}{dt} = \frac{c\sigma}{n} \iiint_{\text{crystal}} \Delta N(r, z)\Phi\phi_L(r, z) \, dV - \frac{\Phi}{\tau_c} = 0, \tag{12}$$

where $\tau c = 2 \, l_c^*/c \, \delta$ (sometimes called the "cold cavity lifetime") is the average lifetime of photons in the cavity expressed as the round-trip time of a photon in the cavity ($2 \, l_c^*/c$) divided by the total fractional loss $\delta = L + T$ per round trip due to intrinsic cavity losses L, and output coupler

transmission T . The population inversion equation (10) can be used in (12) to obtain an implicit relationship between the pump rate, R and the total laser cavity photon number Φ:

$$\frac{2\sigma l_c^*}{n} \iiint_{\text{crystal}} \frac{f\tau_f R r_p(r,z) - N_1^0}{1 + \frac{fc\sigma\tau_f}{n}\Phi\phi_L(r,z)} \phi_L(r,z)\, dV = \delta.$$
(13)

This equation shows that the intrinsic net gain of the medium, which includes the pumped gain and the reabsorption loss, is equal to the total round trip loss in the cavity. For practical laser design purposes, it is often more useful to insert the equation for the population density at threshold (11) and the definition of pump rate (5) into (12) to obtain the expression for the pump rate at threshold:

$$P_{\text{th}} = \frac{h\nu_p(V_{eff}/l_c^*)}{2\eta_p\eta_a f\sigma\tau_f}(L + T + 2N_1^0\sigma l),$$
(14)

where

$$V_{\text{eff}} = 1/\iiint_{\text{crystal}} r_p(r,z)\,\phi_L(r,z)\, dV.$$
(15)

As mentioned above, the presence of the additional loss term $2N_1{}^0\sigma l$ is unique to quasi-three level systems and accounts for the reabsorption of the laser photons in the crystal. Note that (15) allows for arbitrary distributions functions of pump and laser spatial modes. However, it is often sufficient to assume circularly symmetric Gaussian beams for both modes given by

$$r_p(r,z) = \frac{2\alpha}{\eta_a\pi w_p^2}\exp\left(\frac{-2r^2}{w_p^2}\right)\exp(-\alpha z)$$
(16)

and

$$\phi_L(r,z) = \frac{2}{\pi w_L^2 l}\exp\left(\frac{-2r^2}{w_L^2}\right),$$
(17)

where w_p and w_L are the pump mode waist and laser mode waist respectively. Using these spatial modes, (14) becomes,

$$P_{\text{th}} = \frac{\pi h\nu_p\, w_L^2(1+a^2)}{4\eta_p\eta_a f\sigma\tau_f}(L + T + 2N_1^0\sigma l),$$
(18)

where $a = w_p/w_L$.

From the theoretical threshold power, we can estimate the output power of the oscillator using,

$$P_{\text{out}} = \eta(P_{\text{pump}} - P_{\text{th}}),$$
(19)

96

where η is the slope efficiency of the system. There are numerous methods to analytically estimate the slope efficiency of quasi-three level systems. For this work, the following expression is used [9]:

$$\eta = \frac{T}{L+T}\eta_s\,\eta_t\,\eta_p\,\eta_a\,\eta_m \tag{20}$$

where $\eta_s = \nu_L/\nu_p$ is the quantum defect efficiency (sometimes called the Stokes factor), η_t is the pump transfer efficiency and accounts for any losses due to reflection or spill over in the optics that couple the pump radiation into the crystal and η_m is the mode overlap efficiency and is a ratio of the overlapping cross sections of the laser and pump modes in the crystal.

With this basic theoretical treatment, we can analyze our oscillator performance and estimate the various loss mechanisms in effort to maximize output characteristics and efficiency.

Experimental Setup
The general design of our KGW subcavity is based on a laser developed by Sheetz et al. [11]. The layout of the oscillator is shown schematically in Figure 2. We refer to the oscillator as a subcavity because we intend to extend the cavity to reduce the repetition rate and create the physical space necessary to implement a cavity dumping scheme by incorporating a Pockels Cell into the cavity. This initiative to increase the energy per pulse will be discussed in the following section.
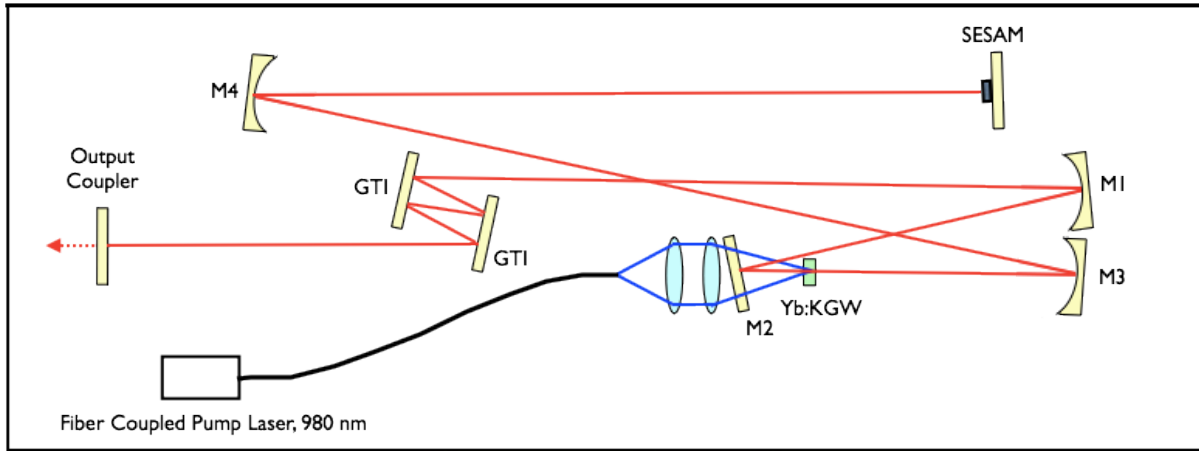
Figure 2. Schematic representation of KGW subcavity layout

The pump source is a 40 W fiber coupled diode module with a 200 μm core diameter emitting at 976-980 nm (nLight, Inc). The fiber output is imaged 1:1 into a 4-mm long, 5-mm wide and 2-mm high AR-coated 5% Yb:KGW crystal (Eksma). The pump light enters the cavity through a short wave pass flat mirror, M2 (Layertec, GmbH), coated for 98% transmission at the pump wavelength (980 nm) and 99.9% reflection at the laser wavelength (1040 nm). The crystal is cooled to 15° C from both sides by thermoelectric coolers (TE Technology, Inc) housed in a home-built water-cooled copper crystal mount. Mirrors M1 and M3 are highly reflective ($\geq$ 99.98%, Layertec,

GmbH) curved mirrors with radii of curvature r = 500 mm. A pair of Gires-Tournois interferometer (GTI) mirrors (Layertec, GmbH), each providing -1300 fs^2 per bounce (four bounces per round trip per mirror) are used for dispersion compensation. Although there have been numerous theoretical treatments addressing the amount of negative dispersion needed for a stably mode locked cavity [11,12], researchers building oscillators for specific practical application often take a trial-and-error approach, especially with discrete valued GTI mirrors, and simply increase the negative dispersion until the stable mode locked output is reached. In Figure 3, Cadet Justin Verde is shown making some modifications to the subcavity in efforts to optimize pump-mode overlap--a key consideration for lasing performance as discussed in the oscillator modeling theory discussed above.

Figure 3. Cadet Justin Verde aligning the pump laser to the cavity mode.
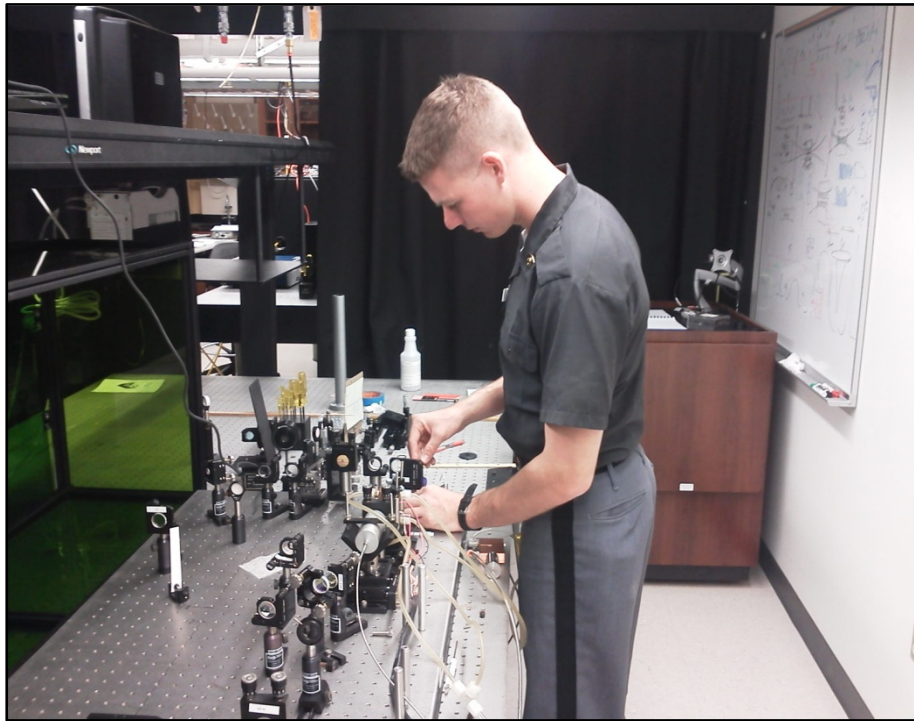
Results and Discussion

As part of the design optimization process, the average output power of the subcavity shown in Figure 2 was measured as a function of pump laser diode temperature. The computer controlled pump laser (nLignt, Inc) enables the user to adjust the diode temperature between 25°-35°C. The pump wavelength varies as a function of temperature so the pump laser can be tuned to get as close to the absorption peak of KGW (981nm) as possible. Figure 4 shows the laser output power as a function of pump power for various diode temperatures. Further measurements are required to determine the cause of the "roll off" at high diode temperature. We are continuing the process of optimizing the cavity for output power and, subsequently, pulse characteristics and mode lock stability.
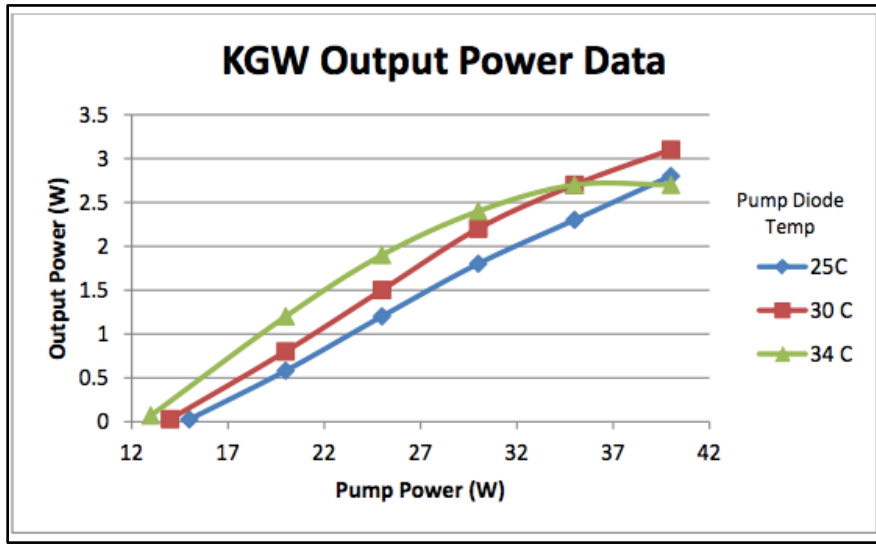
Figure 4. Laser output power as a function of pump diode temperature.

Future Direction

For nearly all of the applications discussed in the Background section above, the objective is to enhance the non-linear advantages provided by ultrashort pulses by maximizing the energy per pulse. This can be done external to the oscillator using, for example, a regenerative amplifier. Such techniques leverage chirped pulse amplification techniques and are extremely effective but require the cost and pulse management challenges of building a completely separate oscillator for external amplification. Another technique that can be used is called "cavity dumping" and uses polarization switching (via a Pockels cell) to keep the a given pulse inside the cavity for numerous round trips through the gain medium and then rotating the polarization with the Pockels cell and extracting from the cavity with a thin film polarizer. This effective reduction in the oscillator repetition rate will drastically increase the energy per pulse.

For example, the subcavity above can generate 300 fs pulses at an average power of 3 W. Given its repetition rate of 65 MHz, the resulting energy per pulse is ~50 nJ. Focusing this 300 fs pulse to a 1-μm spot would give an intensity of 5 GW/cm^2. Intensities on this scale are sufficient for shallow

penetration microscopy but insufficient for imaging deeply into turbid media or micro-machining. However, extending the cavity to 20 MHz and then picking out the pulse every 200 round trips (100 KHz effective) yields 30μJ which when focused to 1-μm would give an intensity of 2 TW/cm^2. Though still not sufficient for ultrahigh intensity applications like filamentation, such intensities can enable significant advances in nonlinear microscopy and micro-machining.

The subcavity shown in Figure 2 will have a serve as the base oscillator to build an extended cavity which will serve two purposes:

1. Create the space to insert a Pockels cell and requisite thin film polarizer and waveplate.
2. Extend the cavity to a low enough repetition rate (<20MHz) so that the Pockels cell can be switched on/off within an inter-pulse spacing period.

Figure 5 shows the extended cavity design as developed in our cavity modeling software (LaserCanvas5, developed by Philip Schlup at Colorado State University). We intend to fully design and characterize the cavity dumped KGW oscillator and then begin work on developing microscopy platform that will enable basic research into imaging and micro-machining/micro-manipulation with high energy pulses directly from the oscillator. To our knowledge, this type of work--absent external amplification--has not been done with KGW.
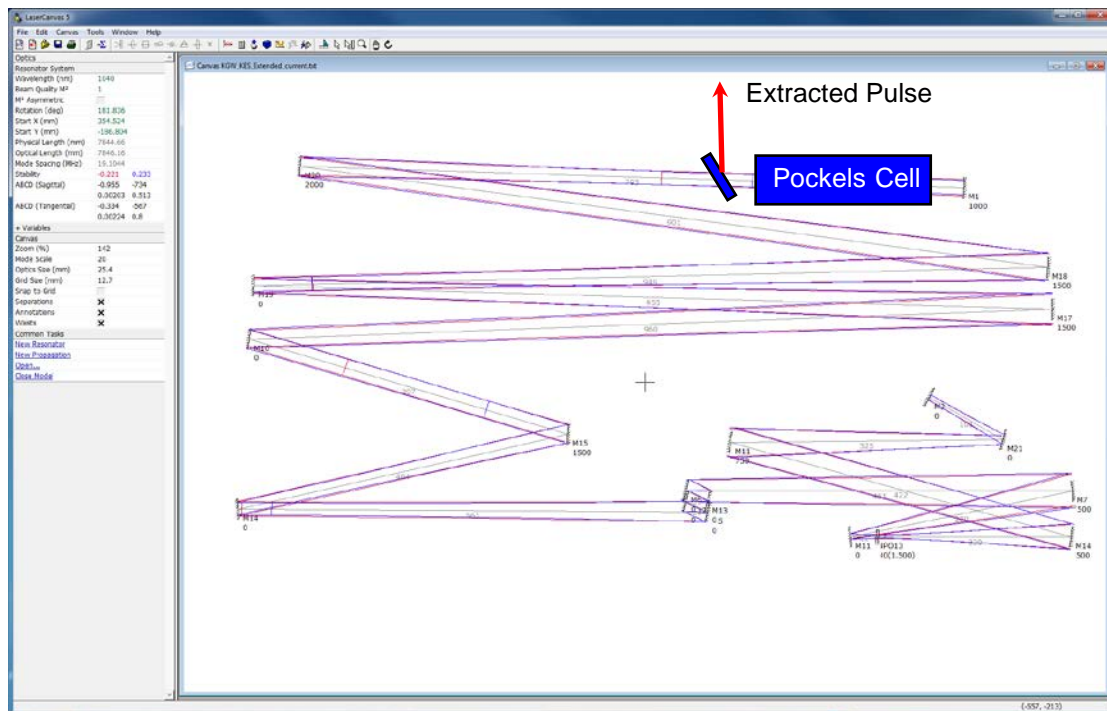

Figure 5. Extended cavity KGW design. Location of Pockels cell shown superimposed on cavity modeling screenshot.

Cadet/Faculty Involvement

LTC Kraig Sheetz, PhD	August 2009 to present
LTC Lou Florence, PhD	August 2012 to present
MAJ Robert Grimming	August 2010 to August 2009
Cadet Justin Verde	August 2012 to present
Cadet Virginia Albany	January 2011 to May 2011
Cadet Michael Eckland	January 2010 to January 2011
Cadet Thomas Wager	January 2011 to May 2011
Cadet Chris Ruis	January 2011 to May 2011

Publications/Presentations

Erich E. Hoover, Michael D. Young, Eric V. Chandler, Dawn N., Vitek, Anding Luo, Jeffrey J. Field, Kraig E. Sheetz, Anne W. Sylvester, and Jeff A. Squier, "Remote focusing for programmable multi-layer differential multiphoton microscopy", *Biomedical Optics Express, 2*, (2011)

Albany, V., Grimming, R. and Sheetz, K. "Improved Design for a Multi-beam Femtosecond Yb:KGW Oscillator," *Rochester Symposium for Physics Students, SPS Zone 2 Regional Meeting*, University of Rochester, NY, April (2011)

Jeffrey J. Field, Ramon Carriles, Kraig E. Sheetz, Eric V. Chandler, Erich E. Hoover, Shane E. Tillo, Thom E. hughes, Anne W. Sylvester, David Kleinfeld and Jeff Squier, *"Optimizing the fluorescent yield in two-photon laser scanning microscopy with dispersion compensation"*, Optics Express, 18 (2010)

Field, J. J., Sheetz, K. E., Chandler, E. V., Hoover, E. E.; Young, M. D., Ding, S.-y., Sylvester, A. W., Kleinfeld, D.; Squier, J. A., "Differential Multiphoton Laser Scanning Microscopy," (Invited) *IEEE Journal of Selected Topics in Quantum Electronics, 99*, (2010)

Carrilles, Ramon, Schafer, Dawn N., Sheetz, Kraig E**.**, Field, Jeffrey J., Cisek, Richard, Barzda, Virginijus, Sylvester, Anne W., Squier, Jeffrey A. "Imaging techniques for harmonic and multiphoton absorption fluorescence microscopy" (Invited) *Review Article: Review of Scientific Instruments*, 80 (2009)

Chandler, E., Hoover, E., Field, J. Sheetz, K., Amir, W., Carriles, R. Ding, S., and Squier, J., "High resolution mosaic imaging with multifocal, multiphoton-counting microscopy," *Applied Optics*, 48 (2009)

Sheetz, K., and Squier, J. "Ultrafast optics: Imaging and manipulating biological systems," (Invited) *Focused Review*, *Journal of Applied Physics*, 105 (2009)

References

[1] Maria, A. J. D., Stetser, D. A. & Heynau, H. "Self mode-locking of lasers with saturable absorbers." *Appl. Phys. Lett*. 8, 174 (1966).

[2] Wang, C. W. & Groves, S. H. "New materials for diode laser pumping of solid- state lasers." *IEEE J. Quantum Electron*. 28, 942 (1992).

[3] Curley, P. F., Ferguson, A. I., White, J. G. & Amos, W. B. "Application of a femtosecond self-sustaining mode-locked ti: sapphire laser to the field of laser scanning confocal microscopy." *Opt. Quantum Electron.* 24, 851 (1992).

[4] Brunner, F. et al. "Diode-pumped femtosecond Yb:KGd(WO4)2 laser with 1.1-W average power." *Opt. Lett.* 25, 1119 (2000).

[5] Klopp, P. et al. "Continuous-wave lasing of a stoichiometric Yb laser material: KYb(WO4)(2)". *Opt. Lett.* 28, 322 (2003).

[6] Fan, T. & Byer, R. "Modeling and CW operation of a quasi-three-level 946 nm Nd:YAG laser." *IEEE J. Quantum Electron*. QE-23 (1987).

[7] Risk, W. "Modeling of longitudinally pumped solid-state lasers exhibiting reab- sorption losses." *J. Opt. Soc. Am. B* 5, 1412 (1988).

[8] Taira, T., Tulloch, W. & Byer, R. "Modeling of quasi-three-level lasers and operation of CW Yb:YAG lasers." *Appl. Opt.* 36, 1867 (1997).

[9] Koechner, W. "Solid-State Laser Engineering. Optical Sciences (Springer, 2006), sixth edn."

[10] Sheetz, K, Hoover, E., Field, J., Kleinfeld, D., and Squier, J., "Advancing multifocal nonlinear microscopy: development of a novel Yb:KGW oscillator", *Optics Express,* 16, (2008).

[11] Krausz, F. et al. "Femtosecond solid-state lasers." *IEEE J. Quantum Electron*. 28, 2097 (1992).

[12] Paschotta, R. & Keller, U. "Passive mode locking with slow saturable absorbers." *Appl. Phys. B* 73, 653 (2001)

PHOTONICS RESEARCH CENTER OF EXCELLENCE

WEST POINT, NEW YORK

HONOR
DUTY
COUNTRY
WEST POINT
MDCCCII
U.S.M.A.

PRC Principle Investigator Biographical Information

Nicholas F. Fell, Jr.

Military Rank: N/A   **Civilian Rank:** DB-IV   **Branch:** N/A

Academic Rank: Assistant Professor, Visiting Scientist

Office Address:
Photonics Research Center
Department of Chemistry and Life Science
Bartlett Hall, Bldg 753, Rm 402
United States Military Academy
West Point, New York 10996
(845) 938-8624
(845) 938-3062 (FAX)
(240)676-6392 (Cell)
Email: nick.fell@usma.edu , nicholas.f.fell.civ@mail.mil

EDUCATION:

Ph.D.	University of Illinois, Urbana-Champaign
	Major: Chemistry, Oct 1993
	Dissertation Advisor: Paul W. Bohn
	Dissertation Title: "Characterization of Diffusion Processes in
	Thin Polymer Films Via Optical Waveguide Techniques."
B.S.	Stevens Institute of Technology, Hoboken, NJ
	Major: Chemistry, 1985

RESEARCH INTERESTS:
Current research interests focus on Raman spectroscopy, energetic materials
characterization and detection, chemical and biological threat detection. In particular, my
current research investigates the use of UV Raman spectroscopy for explosives and
energetic material detection on surfaces. Dr. Fell is the author or co-author of 11 refereed
publications, 2 book chapters, 27 proceedings, and over 60 presentations.

Louis A. Florence

Military Rank: Lieutenant Colonel   **Branch:** Corps of Engineers

Academic Rank: Assistant Professor

Office Address:
Photonics Research Center
Department of Physics and Nuclear Engineering
Bartlett Hall, Bldg. 753, Rm. 404
United States Military Academy
West Point, New York 10996
(845) 938-5810
(845) 938-3062 (FAX)
Email: louis.florence@usma.edu

EDUCATION:

Ph.D.	University of Central Florida, Orlando, FL
	Major: Optics, August 2012
	Dissertation Advisor: Glenn D. Boreman
	Dissertation Title: "Infrared Tapered Slot Antennas Coupled to Tunnel Diodes"
M.S.	University of Rochester, Rochester, NY
	Major: Optical Engineering, June 2002
B.S.	United States Military Academy, West Point, NY
	Major: Engineering Physics, May 1993

RESEARCH INTERESTS:
Current research interests focus on the propagation of and target effects caused by continuous wave high energy laser systems operating at 1 micron.

John P. Hartke

Military Rank: Lieutenant Colonel   **Branch:** Engineer / Academy Professor

Academic Rank: Professor of Photonics

Office Address:
Department of Physics and Nuclear Engineering
Bartlett Hall, Bldg. 753, Rm. 200F
United States Military Academy
West Point, New York 10996-5000
(845) 938-5810
(845) 938-3062 (FAX)
Email: john.hartke@usma.edu

EDUCATION:

Ph.D.	University of Arizona, Tucson, Arizona
	Major: Optical Sciences, 2005
	Dissertation Advisor: Eustace Dereniak
	Dissertation Title: "Dual Band Hyperspectral Imaging Spectrometer"
M.S.	Naval Postgraduate School, Monterey, California
	Major: Physics, 1997
	Thesis Advisor: Richard Harkins
	Thesis Title: "Characterization of an Electromagnetic Railgun"
B.S.	United States Military Academy, West Point, NY
	Major: Engineering Management, 1988

RESEARCH INTERESTS:
Hyperspectral imaging, Infrared focal planes, high energy lasers, physics education

William F. Pearman

Military Rank: Lieutenant Colonel (Retired)   **Branch:** Air Defense Artillery /
                                                                    Academy Professor

Academic Rank: Assistant Professor

Office Address:
Photonics Research Center
Department of Chemistry and Life Science
Bartlett Hall, Bldg 753
United States Military Academy
West Point, New York 10996-5000
(845) 938-4013
(845) 938-3062 (FAX)
Email: William.pearman@usma.edu

EDUCATION:

Ph.D.	University of South Carolina, Columbia
	Major: Analytical Chemistry, December 2007
	Dissertation Advisor: S. Michael Angel
	Dissertation Title: "Enhanced Raman Spectroscopy: Gas Analysis Using a New Type of Multi-Pass Optical Waveguide and Surface-Enhanced Raman Spectroscopy of Biologically Relevant Molecules"
M.S.	University of South Carolina, Columbia
	Major: Analytical Chemistry, May 2003
	Thesis Advisor: S. Michael Angel
	Thesis Title: "Lasers in Analytical Spectroscopy: Dual-Pulse Laser-Induced Breakdown Spectroscopy and Raman Microscopy"
B.S.	Elon College, Elon College North Carolina
	Major: Chemistry, May 1992

RESEARCH INTERESTS:

Analytical Chemistry: Laser Induced Breakdown Spectroscopy, Raman Spectroscopy, Hyper-spectral Imaging, and Chemometrics. My primary interests involve the use of optical spectroscopy for qualitative and quantitative analysis, and to fully understand the theoretical foundations of spectroscopic technique that I employ. I am especially interested in the development, fabrication, and validation of laser based probes that can provide relevant spectrochemical information on site or in situ.

James J. Raftery, Jr.

Military Rank: Colonel   **Branch:** Signal Corps /Acquisition Corps
                                                            Academy Professor

Academic Rank: Associate Professor

Office Address:
Photonics Research Center
Department of Electrical Engineering and Computer Science
Bartlett Hall, Bldg. 753, Rm. 406
United States Military Academy
West Point, New York 10996-5000
(845) 938-5565
(845) 938-3062 (FAX)
Email: James. Raftery@usma.edu

EDUCATION:

Ph.D.	University of Illinois at Urbana-Champaign, Urbana, Illinois
	Major: Electrical Engineering, October 2005
	Dissertation Advisor: Kent D. Choquette
	Dissertation Title: "Vertical-Cavity Surface-Emitting Lasers
	Operating with Multiple Photonic Crystal Defect Cavities"
M.S.S.	U.S. Army War College, Carlisle, Pennsylvania
	Major: Strategic Studies, June 2011
M.S.	University of Missouri-Columbia, Columbia, Missouri
	Major: Electrical Engineering, August 1996
B.S.	Washington University in St. Louis, St. Louis, Missouri
	Major: Electrical Engineering, May 1988

RESEARCH INTERESTS:

Current research interests are in vertical-cavity surface-emitting lasers (VCSEL) and power and energy technologies. Investigating coherent coupling in arrays of photonic crystal (PhC) VCSELs could lead to dynamically steerable optical beams for sensing and free-space communications applications. Investigating basic material and structure methodologies for low energy optimization of VCSELs could lead to energy savings through reduced energy-per-bit optical interconnects for local area networks and large data centers.

Caitlin N. Rinke-Kneapler

Academic Rank: Assistant Professor

Office Address:
Photonics Research Center
United States Military Academy
Building 753N, Room 410
West Point, New York 10996-5000
(845) 938-0460
(845) 938-3062 (FAX)
Email: Caitlin.Rinke@usma.edu

EDUCATION:

Ph.D.	University of Central Florida, Orlando, FL
	Major: Chemistry, August 2012
	Dissertation Advisor: Michael Sigman
	Dissertation Title: " Selective Multivariate Applications in Forensic Science."
B.S.	University of Central Florida, Orlando, Fl
	Major: Forensic Science, August 2008

RESEARCH INTERESTS:
Analytical Chemistry: Laser Induced Breakdown Spectroscopy, Chemometrics, Raman Spectroscopy, and Hyper-spectral Imaging. My primary area of research is the application of chemometric techniques to optical spectroscopy data for identification and classification of complex samples and sample matrices.

Kraig E. Sheetz

Military Rank: Lieutenant Colonel   **Branch:** Military Intelligence / Academy Professor

Academic Rank: Assistant Professor

Office Address:
Department of Physics and Nuclear Engineering
Bartlett Hall, Bldg. 753, Rm. 200D
United States Military Academy
West Point, New York 10996-5000
(845) 938-8611
Email: kraig.sheetz@usma.edu

EDUCATION:

Ph.D.	Colorado School of Mines, Golden, Colorado
	Major: Applied Physics, 2009
	Dissertation Advisor: Jeff Squier
	Dissertation Title: "Advancing Multifocal Nonlinear Microscopy
	Toward Real-Time Three-Dimensional Imaging: Development
	of a Novel $Yb^{3+}KGD(WO_4)_2$ Oscillator"
M.S.	Naval Postgraduate School, Monterey, California
	Major: Applied Physics, 2000
	Thesis Advisor: Thomas Muir
	Thesis Title: Seismo-acoustic buried mine detection
M.S.	New Mexico Institute of Mining and Technology, Socorro, NM
	Major: Geophysics, 1992
	Thesis Advisor: John Schlue
	Thesis Title: Crust and Mantle Structure Inferred from
	Teleseismic Receiver Functions
B.S.	Millersville University, Millersville, PA
	Major: Geophysics, 1990

RESEARCH INTERESTS:
Ultrashort Pulse Lasers, Nonlinear Microscopy, high energy lasers, physics education

Barry L. Shoop

Military Rank: Colonel   **Branch:** Professor, USMA

Academic Rank: Professor of Electrical Engineering

Office Address:
Department of Electrical Engineering and Computer Science
United States Military Academy
West Point, New York 10996-5000
(845) 938-5567
(845) 938-3062 (FAX)
Email: Barry.Shoop@usma.edu

EDUCATION:

Ph.D.	Stanford University, Stanford, California
	Major: Electrical Engineering, June 1992
	Dissertation Advisor: Joseph W. Goodman
	Dissertation Title: "Optical Oversampled Analog-to-Digital Conversion."
M.A.	U.S. Naval War College, Newport, Rhode Island
	Major: National Security and Strategic Studies, June 2002
M.S.	Naval Postgraduate School, Monterey, California
	Major: Electrical Engineering, September 1986
B.S.	The Pennsylvania State University, State College, Pennsylvania
	Major: Electrical Engineering, June 1980

RESEARCH INTERESTS:

Current research interests focus on optical and optoelectronic information processing for analog-to-digital (A/D). Applications include high-speed, high-resolution A/D conversion, multidimensional artificial neural networks for image halftoning. Recent extensions include image processing algorithms for multispectral and hyperspectral processing applications. He is also actively engaged in understanding the role of disruptive innovations in both commercial and defense applications.

John D. Zehnpfennig II

Military Rank: Captain   **Branch:** Engineers / Telecoms Systems Engineer

Academic Rank: Instructor

Office Address:
Photonics Research Center
Department of Electrical Engineering and Computer Science
Bartlett Hall, Bldg. 753, Rm. 409
United States Military Academy
West Point, New York 10996-5000
(845) 938-5558
(845) 938-3062 (FAX)
Email: John.Zehnpfennig@usma.edu

EDUCATION:

M.S.E.	University of Michigan, Ann Arbor
	Major: Electrical Engineering, April 2011
	Thesis Advisor: Tal Carmon
	Thesis Title: " Surface Optomechanics: Forward and Backward Scattered Surface Acoustic Waves in Silica Microsphere."
B.S.	U.S. Military Academy, West Point, New York
	Major: Electrical Engineering, May 2004

RESEARCH INTERESTS:

Current research interests focus on optical and optomechanical interactions within optical whispering gallery resonators and include major research thrusts in the areas of chemical detection and all-optical communications. Applications include pan-species chemical agent weapon detection and ultra-high speed and bandwidth communications devices. A secondary research thrust is related to optimal passive solar collection methods.

Photonics Research Center
United States Military Academy
West Point, New York 10996
http://www.westpoint.edu/prc